

A two-phase model of galaxy formation: I. The growth of galaxies and supermassive black holes

Houjun Mo,^{1,2*} Yangyao Chen,^{3,4} and Huiyuan Wang^{3,4}

¹*Department of Astronomy, University of Massachusetts, Amherst MA01003, USA*

²*Tsung-Dao Lee Institute, Shanghai Jiao Tong University, Shanghai 200240, China*

³*School of Astronomy and Space Science, University of Science and Technology of China, Hefei, Anhui 230026, China*

⁴*Key Laboratory for Research in Galaxies and Cosmology, Department of Astronomy, University of Science and Technology of China, Hefei, Anhui 230026, China*

Accepted XXX. Received YYY; in original form ZZZ

ABSTRACT

We develop a model for galaxy formation and the growth of supermassive black holes (SMBHs), based on the fact that cold dark matter (CDM) halos form their gravitational potential wells through a fast phase with rapid change in the potential, and that the high universal baryon fraction makes cooled gas in halos self-gravitating and turbulent before it can form rotation-supported disks. Gas fragmentation produces sub-clouds so dense that cloud-cloud collision and drag on clouds are not significant, producing a dynamically hot system of sub-clouds that form stars and move ballistically to feed the central SMBH. Active galactic nucleus (AGN) and supernova (SN) feedback is effective only in the fast phase, and the cumulative effects are to regulate star formation and SMBH growth, as well as to reduce the amount of cold gas in halos to allow the formation of globally stable disks. Using a set of halo assembly histories, we demonstrate that the model can reproduce a number of observations, including correlations among SMBH mass, stellar mass of galaxies and halo mass, the number densities of galaxies and SMBH, as well as their evolution over the cosmic time.

Key words: galaxies: haloes – galaxies: formation – quasars: supermassive black holes

1 INTRODUCTION

In the current Λ CDM scenario of structure formation, galaxies and supermassive black holes (SMBHs) hosted by them form in the gravitational potential wells of dark matter halos in the cosmic density field (e.g. Mo et al. 2010). It is thus crucial to understand how the formation and evolution of galaxies and SMBHs are determined by the growth and structure of dark matter halos. Despite the progress made so far using methods ranging from full hydro simulations (e.g. Springel & Hernquist 2003; Springel 2010; Genel et al. 2014; Vogelsberger et al. 2014; Schaye et al. 2015; Pillepich et al. 2018b; Springel et al. 2018; Davé et al. 2019) to simple analytical modeling (e.g. Mo et al. 1998; Dekel et al. 2013), the details remain poorly understood. For example, we still do not understand fully what processes separate the two basic types of galaxies, elliptical and disk, and how SMBHs fit into and affect the formation processes.

The difficulty arises from the complexity of the problem. Numerical simulations show that the halo population is very diverse not only in their mass, but also in other important properties relevant to galaxy formation, such as the spin, shape, and formation history (e.g. Macciò et al. 2007; Li et al. 2008; Wong & Taylor 2012; Mao et al. 2018; Chen et al. 2020, 2023b; Wang et al. 2024). Even more complex is the formation and evolution of the baryonic components, such as gas, stars and SMBHs, as they are affected not only by gravity but also by many gas-dynamical and radiative processes. These pro-

cesses are far from linear; they are strongly coupled with each other, and could even be self-interacting through feedback loops (e.g. Crain et al. 2015; Weinberger et al. 2017; Pillepich et al. 2018a; Davé et al. 2019).

As in dealing with any complex system, the best approach is to move step by step, starting from the simplest model that involves the most important properties of the driver population of the evolution, in our case dark matter halos. One then moves forward by adding more complexities when needed. The addition of complexity must be done intelligently, so that our goal of understanding the underlying physical processes is not lost in our endeavor.

One of the key properties of the halo population is the regularity in their formation histories. As shown by numerical simulations (Wechsler et al. 2002; Zhao et al. 2003, 2009), the assembly of dark halos in a cold dark matter (CDM) cosmology typically consists of two distinct phases: a fast assembly phase in which the gravitational potential well of the halo is established, and a slow assembly phase during which mass is added into the halo gently without changing the potential well significantly. The early fast assembly phase is also found to be associated with violent changes in the gravitational potential, which can cause energy exchanges between mass particles and make the velocity dispersion of these particles more isotropic (e.g. Zhao et al. 2003; Lu et al. 2006).

Another key condition for galaxy formation is set by current cosmology. Although the mass in the universe is dominated by cold dark matter (CDM), the mass fraction contained in baryons, $f_B \approx 0.15$, is significant gravitationally. Furthermore, the gas component is dissi-

* E-mail: hjmo@umass.edu

pative, so that it can cool and collapse further in a dark matter halo, making it gravitationally dominating on small scales where such dissipation is important. The typical specific angular momentum of dark matter halos, as described by the spin parameter λ , is in general too low to significantly impede the dissipation and collapse of the gas before it becomes self-gravitating. This, combined with the rapid change of the gravitational potential during the fast assembly phase, is expected to produce self-gravitating, dynamically hot (turbulent) clouds. These clouds can then fragment to form sub-clouds within which stars form and SMBHs grow. This early formation may also be accompanied by strong feedback that can reduce the cold gas fraction to a level $\sim \lambda$ so that globally stable disks with realistic rotation curves can form (e.g. [Mo et al. 1998](#)). In this scenario, the feedback is ‘ejective’ in the fast assembly phase, but becomes ‘preventive’ in the subsequent slow assembly phase. Such a two-phase scenario of galaxy formation has been put forward by [Mo & Mao \(2002\)](#) and [Mo & Mao \(2004\)](#), and worked out in some detail by [Cook et al. \(2009\)](#) and [Lu et al. \(2015\)](#) using an analytical approach, and by [Boco et al. \(2023\)](#) using an abundance-matching scheme. The turbulence and fragmentation of the gas associated with the fast assembly phase may also create conditions for seeding and growing SMBHs (e.g. [Hobbs et al. 2011](#); [Latif et al. 2022](#)), which allows us to treat the growth of the SMBHs and active galactic nuclei (AGN) feedback in the same framework as galaxy formation.

In this paper, we expand the two-phase formation scenario by developing a framework to model galaxy formation and the growth of SMBHs in dark matter halos predicted by current cosmology. The presentation of our framework will be based on a set of simple assumptions that make our model transparent to key processes driving the evolution. Our model is also quantitative so that it can be applied to make model predictions that can be tested with observations. The structure of the paper is as follows. In Section 2 we describe basic halo properties used in our model, including a scheme to separate the fast and slow assembly phases. In Section 3 we analyze the cooling and collapse of the gas component in dark matter halos, and present the case for the formation of self-gravitating, turbulent gas clouds (SGC) and their fragmentation to form gas sub-clouds. Section 4 describes how stars form and the SMBH grows in an SGC. The application of our model to simulated halos is given in Section 5, together with model predictions and comparisons with observational data. Finally, in Section 6, we summarize the main components and predictions of our model, and make further discussions. A code library that implements our model to populate halos with galaxies and SMBHs, along with the data used to make all the figures in the paper, is described in the Data Availability section.

2 DARK MATTER HALOS

We consider galaxy formation in cold dark matter (CDM) halos. We model the halo mass density distribution using the NFW profile

$$\rho(r) = \rho_{\text{crit}} \frac{\delta_{\text{v}}}{(r/r_{\text{s}})(1+r/r_{\text{s}})^2}, \quad (1)$$

where $\rho_{\text{crit}} \equiv 3H^2(z)/(8\pi G)$ is the critical density of the universe at the redshift z in question, r_{s} is a scale radius, and δ_{v} is a characteristic over-density (e.g. [Navarro et al. 1997](#)). Based on the spherical collapse model and virial theorem, we define δ_{v} so that the mean density within the halo radius, r_{v} , is $\bar{\rho}_{\text{v}} = 200\rho_{\text{crit}}$. In this case,

$$\delta_{\text{v}} = \frac{200}{3} \frac{c^3}{\mu(c)}, \quad (2)$$

where

$$c \equiv \frac{r_{\text{v}}}{r_{\text{s}}} \quad (3)$$

is the halo concentration, and

$$\mu(y) \equiv \ln(1+y) - y/(1+y). \quad (4)$$

The halo mass within a radius r is

$$M(< r) = 4\pi\rho_{\text{crit}}r_{\text{s}}^3\mu(cx), \quad (5)$$

where $x = r/r_{\text{v}}$. We also define a circular velocity at radius r ,

$$V_{\text{c}}(r) = \sqrt{\frac{GM(< r)}{r}}. \quad (6)$$

The halo (virial) mass, M_{v} , and circular velocity, V_{v} , are defined as $M(< r)$ and $V_{\text{c}}(r)$ evaluated at $r = r_{\text{v}}$, respectively:

$$M_{\text{v}} \equiv M(< r_{\text{v}}); \quad V_{\text{v}} \equiv \sqrt{\frac{GM_{\text{v}}}{r_{\text{v}}}}. \quad (7)$$

The formation history of a dark matter halo is represented by its merger tree. The mass growth of a halo is described by its mass assembly history, $M_{\text{v}}(z)$, which is the virial mass of the progenitor halo at redshift z along the main branch of the halo. The mass growth of the halo at z , over an interval Δz , can then be defined as

$$\Delta M_{\text{v}}(z) = \frac{dM_{\text{v}}(z)}{dz} \Delta z. \quad (8)$$

As shown in [Zhao et al. \(2003\)](#), the formation of CDM halos in general consists of a fast phase, where the mass increases with time rapidly, followed by a slow phase, where the mass assembly rate is slower. The distinction between these two phases is more clearly seen in the redshift evolution of $V_{\text{v}}(z)$. In the fast assembly regime, $V_{\text{v}}(z)$ increases rapidly with time (i.e. with decreasing z), while $V_{\text{v}}(z)$ remains almost constant or even declines with time in the slow phase. These behaviors can be seen in the examples shown in the top panels of Fig. 1 (see §5.1 and Appendix A for halo samples used in this paper).

For convenience, we denote the transition redshift of the two phases as z_{f} (‘f’ means fast). To obtain z_{f} of a halo, we trace its main branch assembly history and use

$$\frac{\dot{V}_{\text{v}}(z)}{V_{\text{v}}(z)} = \gamma(z)H(z) \quad (9)$$

to obtain $\gamma(z)$, the specific growth rate of the virial velocity. Following the arguments given in §4 of [Zhao et al. \(2003\)](#), we use the redshift when $\gamma(z)$ first reaches the threshold $\gamma_{\text{f}} = 3/8$ to define z_{f} :

$$\gamma(z_{\text{f}}) = \gamma_{\text{f}} = 3/8 \quad (\text{High-}z_{\text{f}}). \quad (10)$$

Models using this definition of z_{f} will be referred to as the High- z_{f} variant, since z_{f} so obtained is in general higher than those obtained by other definitions (see below). [More et al. \(2015\)](#) and [Boco et al. \(2023\)](#) both adopted $\Gamma_{\text{f}} \equiv \Gamma(z_{\text{f}}) = 3/2$ in their modeling based on the mass history, $\dot{M}_{\text{v}}(z)/M_{\text{v}}(z) = \Gamma(z)H(z)$. This corresponds to $\gamma_{\text{f}} = 0$ at high z . We thus also consider another case,

$$\gamma(z_{\text{f}}) = \gamma_{\text{f}} = 0 \quad (\text{Low-}z_{\text{f}}), \quad (11)$$

where Low- z_{f} indicates that the value of z_{f} defined with $\gamma_{\text{f}} = 0$ is in general lower than that defined with $\gamma_{\text{f}} = 3/8$ (see Appendix B for a comparison of different definitions).

Halo assembly histories in simulations are in general quite noisy, as can be seen from the simulated V_{v} and V_{max} curves shown in the top panels of Fig. 1. The time differentiation, $\gamma(z)$, is even noisier,

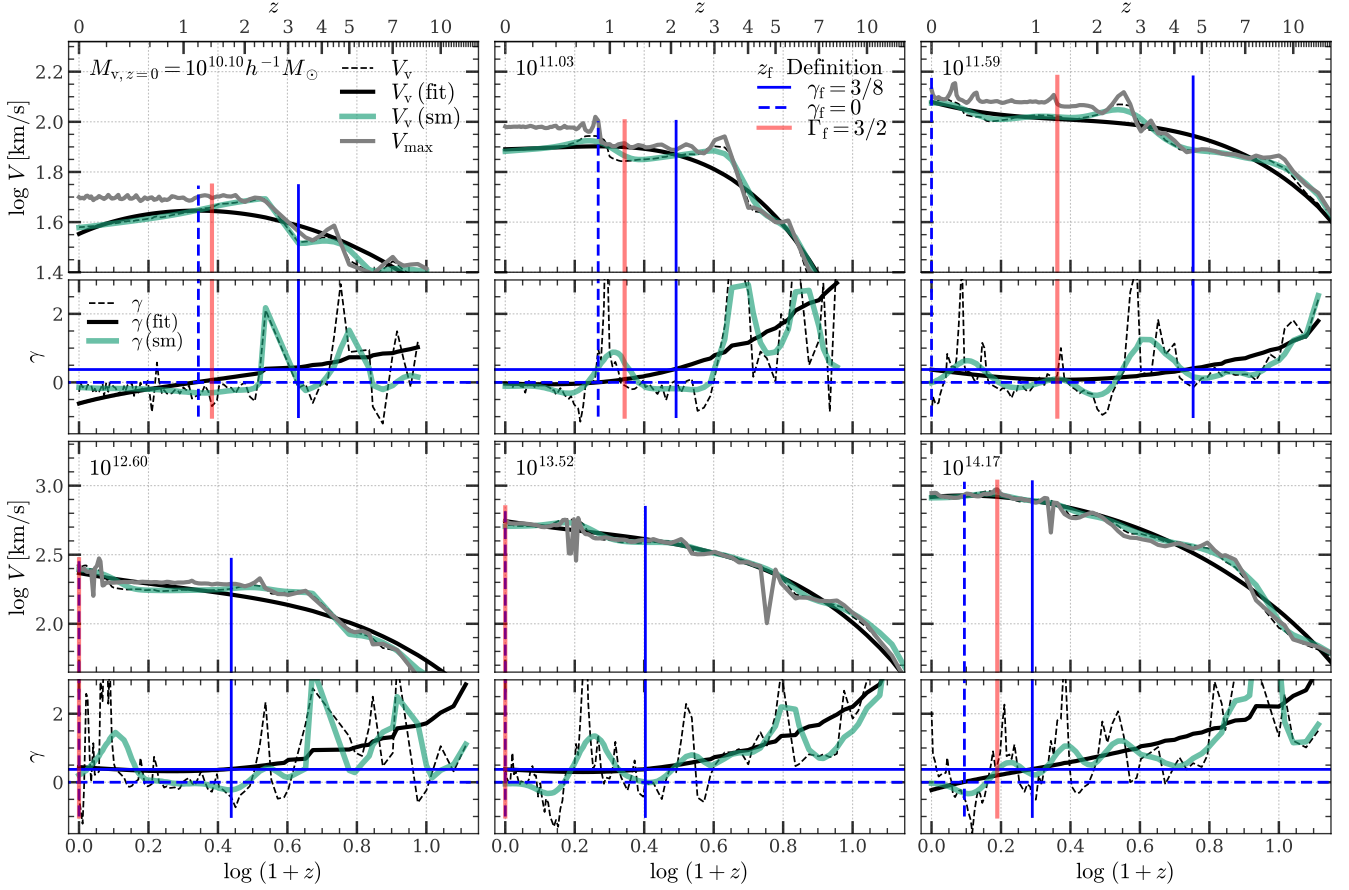


Figure 1. Assembly histories of individual halos (each pair of panels) described by circular velocity as a function of redshift. For each halo, the virial velocity, $V_v(z)$, is shown by the **black dashed curve**, obtained directly from the simulation. The **black solid curve** shows the virial velocity obtained from a parametric fitting of halo mass assembly history (Eq. 12), while the **green curve** shows that obtained from a smoothing of halo mass assembly history by a Gaussian kernel with $\sigma = \tau_{\text{dyn}}(z)$, the dynamical time scale of the halo. The **gray curve** shows the maximal circular velocity, $V_{\text{max}}(z)$, obtained from the simulation. The virial mass, $M_v \equiv M_{200c}$, at $z = 0$ is indicated in the top-left corner of each top panel. The velocity is shown in each **top panel**, while the corresponding **bottom panel** displays $\gamma(z)$, which represents the specific growth rate of $V_v(z)$. Transition redshifts, z_f , obtained using three definitions, as indicated in the legend of the top-center panel, are shown by three **colored vertical lines**. In each bottom panel, the **blue solid and dashed horizontal lines** denote the threshold $\gamma_f = 3/8$ and $\gamma_f = 0$ used to define z_f in the High- z_f and Low- z_f variants of our model, respectively. All the halos presented here are selected from the small sample, $S_{h,\text{small}}$ (see §5.1). For detailed information about halo assembly history and transition redshift, see §2. This figure clearly demonstrates the two-phase nature of CDM halo assembly, which forms the foundation for our two-phase model of the growth of galaxies and SMBHs.

as seen from the bottom panels of the same figure. To identify the transition redshift reliably, we fit each halo assembly history, $M_v(z)$, by a smooth function¹,

$$\ln M_v(z) = c_0 + c_1 \frac{z}{1+z} + c_2 \ln(1+z) + c_3 z, \quad (12)$$

where (c_0, c_1, c_2, c_3) are four free parameters. This functional form is similar to that used by Behroozi et al. (2019), and it can be viewed as an extension of the fitting methods used by, e.g. Wechsler et al. (2002), van den Bosch (2002), McBride et al. (2009) and Correa et al. (2015). Our tests show that the four-parameter fitting gives more stable and accurate results for the problem interested here. The evolution of $V_v(z)$ is then obtained by

$$V_v(z) = \left[\frac{\Delta_v(z)}{2} \right]^{1/6} [GM_v(z)H(z)]^{1/3}, \quad (13)$$

¹ To avoid confusion, we use ‘log’ to denote 10-based logarithm, and ‘ln’ to denote e -based logarithm.

where $\Delta_v(z) \equiv 200$. The dependence of γ and Γ on z can be obtained from the fittings to $V_v(z)$ and M_v , respectively. The fitting results of $V_v(z)$ and $\gamma(z)$ are shown by the black solid curves in Fig. 1. Finally, to reduce the ambiguity due to multiple solutions, we search for z_f by maximizing a ‘loss’ function defined as

$$l_\gamma(z|\gamma_f) = \ln \frac{V_v(z)}{V_v(z_f)} + \gamma_f \ln(1+z). \quad (14)$$

It is easy to show that the extreme location, $\text{argmax}_z [l_\gamma(z|\gamma_f)]$, is equivalent to the solution of $\gamma(z) = \gamma_f$.

The vertical lines in Fig. 1 mark the values of z_f obtained using different definitions. For most halos, the value represented by the blue dashed line ($\gamma_f = 0$) is significantly larger than that by the blue solid line ($\gamma_f = 3/8$), and the red line ($\Gamma_f = 3/2$) lies in between. In Appendix B, we show that the transition redshift obtained by all these definitions is a monotonically decreasing function of the halo mass. We also compare the transition redshift with the commonly used half-mass formation redshift to obtain some idea about the different definitions of the transition redshift.

For halos that are still in the fast assembly regime, [Zhao et al. \(2003\)](#) found that the halo concentration is about $c = c_f \approx 4$, with the exact value of c_f depending on the definition of the halo radius r_v . [Zhao et al. \(2003\)](#) also found that particles accreted at $z < z_f$ are distributed in the outer part of the halo, at $r > c_f r_s$, while those accreted in the fast assembly regime stay in the inner part, at $r \leq c_f r_s$. Note that $r = c_f r_s$ is close to the radius where the halo circular velocity reaches its peak and the density profile is roughly the isothermal profile, $1/r^2$. Thus, for a given halo, we may define a radius

$$r_f \approx c_f r_s = (c_f/c)r_v, \quad (15)$$

which separates an inner part, where mass is assembled into the halo by fast accretion and an outer part, where the mass is assembled mainly through slow accretion. So defined, $r_f = r_v$ for halos that are still in their fast assembly regime. The mass within r_f is

$$M_f = M(< r_f) = M_v \frac{\mu(c_f)}{\mu(c)}. \quad (16)$$

Since M_f is the halo mass assembled in the fast regime, the mass assembled in the slow accretion regime is, by definition, $M_v - M_f$.

The average density within r_f is

$$\bar{\rho}_f = \frac{3M_f}{4\pi r_f^3} = \frac{\mu(c_f)}{\mu(c)} \left(\frac{c}{c_f}\right)^3 \times \bar{\rho}_v. \quad (17)$$

Given that the mean density is proportional to the critical density of the universe, the time, t_f , when the mean density of a halo reaches $\bar{\rho}_f$ is related to the current time, t , by

$$H^2(t_f) = \frac{\mu(c_f)}{\mu(c)} \left(\frac{c}{c_f}\right)^3 \times H^2(t). \quad (18)$$

For an Einstein-de Sitter universe, or for $z \gg 1$, $H^2(t_f)/H^2(t) = (1+z_f)^3/(1+z)^3$, and so $(1+z_f) \sim (c/c_f)(1+z)$.

The dynamical time scale of the gravitational collapse of a halo is about $\tau_{\text{dyn}} \equiv R_v/V_v$. Thus the typical time for the halo structure to adjust to a new state corresponding to the change in the mass accretion is τ_{dyn} . For reference, we smooth $M_v(z)$ using a Gaussian kernel with standard deviation $\sigma(z) = \tau_{\text{dyn}}(z) = R_v(z)/V_v(z)$, where z is the redshift of the snapshot in question, and we obtain other virial quantities, such as $V_v(z)$ and $\gamma(z)$, from the smoothed $M_v(z)$. The results are shown by the green curves in Fig. 1. The smoothed $\gamma(z)$ follows the general trend of that obtained by the parametric fitting, but contains significant fluctuations even within a given phase of mass assembly. This suggests that a halo in the fast assembly phase can sometimes make an excursion to the slow phase and vice versa. We will discuss in §3.3 the implications of such excursions for the formation of galaxies in halos.

In the following, we will use the features of dark matter halos described above to develop a model for the formation and evolution of galaxies and SMBHs. Our modeling adopts a ‘step-wise’ strategy (e.g. [Lu et al. 2014](#)), deliberately designed to avoid over-fitting. Briefly, for each relevant process, we start with a physically motivated, heuristic functional form with all parameters held constant. We then introduce secondary dependencies, such as redshift, only when they are implied by observational evidence. An assumption made in this paper is the instantaneous recycling of baryons, where gas components are quantified by their ‘effective’ amounts at a given time that describe the net results of multiple cycles of inflow and outflow. Thus, the modeled quantities should be interpreted as averages over a period defined by the recycling timescale, which is typically the dynamical time or the cooling time, depending on the specific properties and scales in question. The details of baryon cycles remain poorly

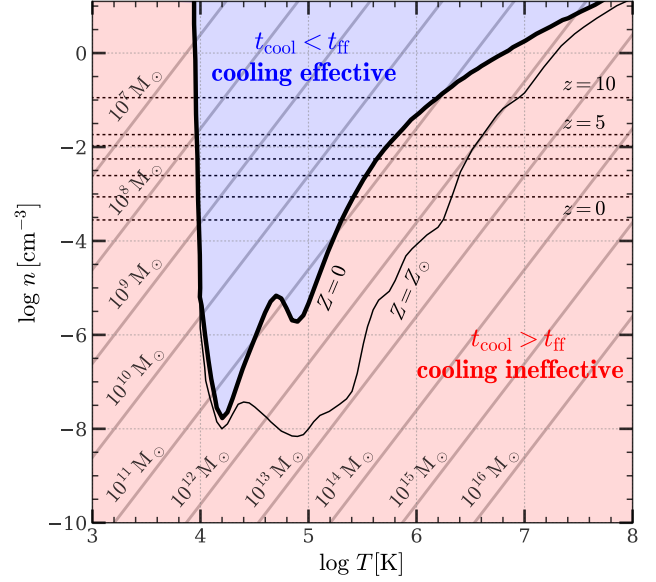


Figure 2. The cooling diagram. The **thick and thin black curves** show the locus of $t_{\text{cool}} = t_{\text{ff}}$ in the plane of gas particle number density (n) and gas temperature (T) for halo gas with zero and solar metallicity, respectively. The **gray tilted solid lines** are lines of constant halo mass ($M_v \equiv M_{200c}$). **Horizontal dashed lines**, from lower to upper, indicate the density of virialized halos at redshifts $z = 0, 1, 2, 3, 4, 5$, and 10 . The blue and red shaded regions indicate the regimes of effective and ineffective cooling, respectively. These calculations are based on a Λ CDM cosmology with $f_{\text{gas}} = 0.15$, $h = 0.7$, and $\Omega_{M,0} = 0.3$. For a more detailed description, see §3.1.

constrained by observations, particularly at high z (see, e.g. [Zhang et al. 2023b](#); [Lin et al. 2023](#)), and are not included in our model. To account for potential short-term fluctuations that are omitted in our model, we incorporate some random noise based on our best understanding of the uncertainties when conducting comparisons between model predictions and observational data.

3 THE COLLAPSE OF THE GAS COMPONENT

3.1 The role of radiative cooling

Cosmic gas is originally mixed uniformly with dark matter and collapses together with the dark matter as a halo forms. If the gas is initially heated by accretion shocks associated with the collapse, radiative processes can cool it down. The effectiveness of radiative cooling is represented by a cooling time scale, t_{cool} , under the assumption that the gas is at the virial temperature, $T = T_v$:

$$t_{\text{cool}} \approx 3.3 \times 10^9 \frac{T_6}{n_{-3} \Lambda_{-23}(T)} \text{ yrs}, \quad (19)$$

where n_{-3} is the gas number density in units of 10^{-3}cm^{-3} , $T_6 \equiv T_v/(10^6 \text{K})$, and Λ_{-23} is the cooling function in units of $10^{-23} \text{erg s}^{-1} \text{cm}^3$. This time scale is compared with the free-fall time scale of the gas,

$$t_{\text{ff}} = \sqrt{\frac{3\pi}{32G\bar{\rho}}} \approx 2.1 \times 10^9 f_{\text{gas}}^{1/2} n_{-3}^{-1/2} \text{ yrs}, \quad (20)$$

where $\bar{\rho}$ is the typical total mass density of the halo, and f_{gas} is the gas mass fraction. If we approximate the cooling function by a power

law, $\Lambda(T) \propto T^{-\mu}$, then

$$\frac{t_{\text{cool}}}{t_{\text{ff}}} \propto \frac{1}{f_{\text{gas}}} M_{\text{v}}^{2(1+\mu)/3} \rho^{-(2\mu-1)/6}, \quad (21)$$

where μ is the mean molecular mass of the gas particle in units of the proton mass. For an enriched gas at temperature $T \sim 10^6$ K, $\mu \sim 0.5$, the following interesting relation holds roughly:

$$\frac{t_{\text{cool}}}{t_{\text{ff}}} \sim \left(\frac{f_{\text{gas}}}{0.15}\right)^{-1} \left(\frac{M_{\text{v}}}{10^{12} M_{\odot}}\right). \quad (22)$$

Thus, radiative cooling is expected to be effective, i.e. $t_{\text{cool}} < t_{\text{ff}}$, for all halos with masses below $M_{\text{cool}} \sim 10^{12} M_{\odot}$, quite independent of redshift, as shown in Fig. 2. This suggests that the gas that can cool is a fraction of the total, and this fraction can be modeled as

$$F_{\text{cool}}(M_{\text{v}} | M_{\text{cool}}, \beta_{\text{cool}}) = \frac{1}{1 + (M_{\text{v}}/M_{\text{cool}})^{\beta_{\text{cool}}}}, \quad (23)$$

where $\beta_{\text{cool}} \sim 1$ and $M_{\text{cool}} \sim 10^{12} M_{\odot}$ are two model parameters. So modeled, $F_{\text{cool}} \rightarrow 1$ for $M_{\text{v}} \ll M_{\text{cool}}$ and $\rightarrow 0$ for $M_{\text{v}} \gg M_{\text{cool}}$. Note that the cooled amount of gas described by F_{cool} is an upper limit, assuming that the gas inflow is not coupled with, for example, hot outflows resulting from feedback processes. The actual amount of gas entering the galaxy and forming stars is modified by additional operators to be described later.

Note that $t_{\text{cool}}/t_{\text{ff}}$ scales inversely with f_{gas} , and that t_{ff} defined above is about 1/10 times the Hubble time: $t_{\text{ff}} \sim t_{\text{H}}/10$. Thus, for example, the locus of $M_{\text{v}} = 10^{11} M_{\odot}$ will be shifted to that labeled by $M_{\text{v}} = 10^{12} M_{\odot}$ in the figure, either if the Hubble time is used instead of the free-fall time, or if f_{gas} is ten times smaller than the cosmic baryon fraction. Similarly, such changes will cause a shift of the locus of $M_{\text{v}} = 10^{12} M_{\odot}$ to that labeled by $M_{\text{v}} = 10^{13} M_{\odot}$ in the figure.

Fig. 2 also shows that radiative cooling is very effective in the temperature range $10^4 \text{ K} < T < 10^5 \text{ K}$. This range roughly corresponds to $10^{10} M_{\odot} < M_{\text{v}} < 10^{11} M_{\odot}$ at $z \approx 0$, and $10^9 M_{\odot} < M_{\text{v}} < 10^{10} M_{\odot}$ at $z \approx 5$.

3.2 The role of angular momentum

In the presence of angular momentum, gas can be supported by its angular momentum in the host halo to form a rotation-supported disk. According to the model described in Mo et al. (1998), halo gas typically needs to collapse by a factor of λ (the effective spin parameter of the gas) to become supported by rotation. Thus, as long as the cooled gas fraction, f_{gas} , is larger than λ , the collapsing gas will become self-gravitating before it can settle into a rotation-supported disk. In contrast, if the gas fraction is comparable to or smaller than the spin parameter, the collapse of the cooled gas will settle down to a rotation-supported disk before the gas can fragment and form stars. Previous modeling of the observed size distribution of disk galaxies in the Universe indicates that the required λ -distribution is roughly log-normal, with a median ~ 0.04 and a dispersion $\sigma_{\ln \lambda} \sim 0.5$ (e.g. Shen et al. 2003; Somerville et al. 2008; Desmond & Wechsler 2015; Burkert et al. 2016; Somerville et al. 2018). This distribution is similar to that of dark matter halos (e.g. Bullock et al. 2001b; Bett et al. 2007; Macciò et al. 2007), but it does not necessarily mean that individual galaxies have similar spins to their host halos (see, e.g. Danovich et al. 2015; Jiang et al. 2019). Regardless of the origin of spins of galaxies, the typical value obtained from observations, $\lambda \sim 0.04$, is much smaller than the cosmic baryon fraction, $f_{\text{B}} = 0.15$. Thus, as long as radiative cooling is effective and f_{gas} is not much smaller than the cosmic baryon fraction, the collapse of the halo

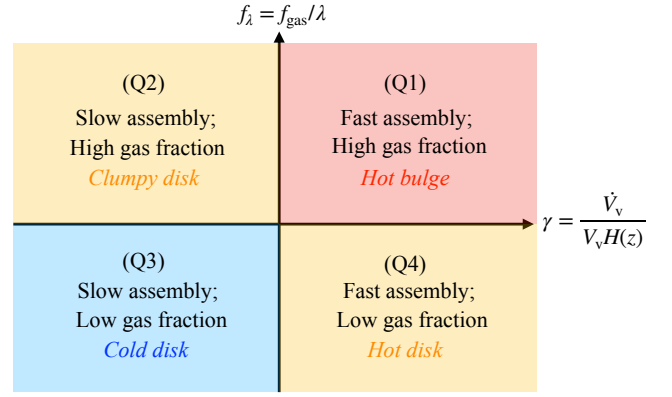


Figure 3. The quadrant diagram showing four combinations of $\gamma \equiv \dot{V}_{\text{v}}/[V_{\text{v}}H(z)]$, which describes the rate of assembly, and $f_{\lambda} \equiv f_{\text{gas}}/\lambda$, which describes the importance of angular momentum in supporting gas. The formation of a galaxy in a halo can be represented by a trajectory in the $f_{\lambda}(t)-\gamma(t)$ space, and the formation of different structural components depends on the location in the diagram. See §3.3 for a detailed discussion for the quadrants. This figure motivates the use of γ as a key parameter to separate the two phases of halo assembly and build the model for galaxy formation and SMBH growth based on the separation.

gas will not be affected much by the angular momentum before it becomes self-gravitating. However, if f_{gas} is reduced to a value comparable or smaller than λ due to, e.g. ineffective cooling and other (e.g. feedback) processes associated with galaxy formation, then the gas will be able to form a rotation-supported disk before it collapses further to form stars in the gravitational potential of the dark matter halo.

3.3 The four quadrants of gaseous structure formation

The discussion above suggests that the collapse of cooled gas in dark matter halos may be characterized by the value of γ that describes the change of the gravitational potential and

$$f_{\lambda} \equiv \frac{f_{\text{gas}}}{\lambda}, \quad (24)$$

which describes the importance of the angular momentum. If we divide each of the two parameters into two portions, high and low, according to their critical values at $(\gamma, f_{\lambda}) = (3/8, 1)$ based on the discussion above, we have four different combinations corresponding to the four quadrants in the $\gamma-f_{\lambda}$ plane shown in Fig. 3. In what follows, we discuss the structure of the gas expected in each of the quadrants. The formation of a galaxy can then be considered as a trajectory in this plane. The quadrant diagram may, therefore, be used to understand the evolution and structure of individual galaxies.

Q1: Self-gravitating and turbulent gaseous spheroids

Let us first look at the first quadrant where $f_{\lambda} > 1$ and the collapse is in the fast regime, with $\gamma > \gamma_{\text{f}}$. We note that the gravitational potential is dominated by dark matter as long as the gas and dark matter are well mixed. As the gas cools and collapses in its halo, the gravity of the gas component will become more important. The gas is expected to become self-gravitating when the circular velocity it generates is larger than that of the dark matter. Using the definition of the circular velocity, we can write

$$V_{\text{c}}^2(r) = \frac{GM(<r)}{r} = \frac{GM_{\text{g}}(<r)}{f_{\text{gas}} r}. \quad (25)$$

Thus, for a roughly flat rotation curve, as is the case of CDM halos, the above relation suggests that the gas has to collapse by a factor of about $1/f_{\text{gas}}$ relative to the dark matter to become self-gravitating. Since $f_\lambda > 1$, rotation support is not important with such a collapse factor and the structure of the gas is roughly spheroidal. For convenience, we will refer to such a self-gravitating gas cloud as the SGC. The gas mass density will then be comparable to that of dark matter. For the gas assembled in the fast accretion phase, the radius at self-gravitating is thus

$$r_{f,\text{SGC}} = f_{\text{gas}} r_f, \quad (26)$$

and the gas mass is

$$M_{f,\text{SGC}} = f_{\text{gas}} M_f. \quad (27)$$

The mean gas density at this point is then

$$\bar{\rho}_{f,\text{SGC}} = \frac{3M_{f,\text{SGC}}}{4\pi r_{f,\text{SGC}}^3} = \frac{\bar{\rho}_f}{f_{\text{gas}}^2}. \quad (28)$$

The free-fall time scale of the gas, which is determined by the gas density, is now about f_{gas} times that given by $\bar{\rho}_f$.

We can also obtain the relation between the size and mass for the SGC. At a given redshift, the halo radius scales with the halo mass as $r_v \propto M_v^{1/3}$. Thus

$$r_f \propto \left(\frac{M_v}{M_f}\right)^{1/3} \frac{r_f}{r_v} M_f^{1/3} \propto \left(\frac{\bar{\rho}_v}{\bar{\rho}_f}\right)^{1/3} M_f^{1/3} \propto \frac{c_f}{c_v} M_f^{1/3}. \quad (29)$$

We may write

$$c_f/c \propto M_v^{\beta_c} \quad (\beta_c > 0), \quad (30)$$

so that

$$r_f \propto \left(\frac{M_v}{M_f}\right)^{\beta_c} M_f^{\beta_c+1/3}. \quad (31)$$

Since M_f/M_v depends on M_v only logarithmically, we have

$$r_f \propto M_f^{\beta_c+1/3}. \quad (32)$$

This will lead to a relation with a logarithmic slope steeper than $1/3$. [Shen et al. \(2003\)](#) found that the size of an early-type galaxy scales with its stellar mass roughly as $R \propto M_*^{0.55}$. If these galaxies are formed from the SGC with a constant star formation efficiency, we need $\beta_c = 0.25$, which is consistent with the decrease of c with the halo mass. In reality, the star formation efficiency is expected to depend on both redshift and halo mass, and thus different values of β_c may be possible to reproduce the observed size-mass relation. We will come back to this topic in the second paper of this series ([Chen et al. 2023a](#)).

The Jeans mass of a gas at temperature T can be written as

$$M_J = 5 \times 10^7 \left(\frac{c_s}{10 \text{ km s}^{-1}}\right)^3 \left(\frac{n_{\text{gas}}}{1 \text{ cm}^{-3}}\right)^{-1/2} M_\odot, \quad (33)$$

where $c_s(T)$ and n_{gas} are the gas sound speed and density, respectively. As discussed above, effective atomic cooling can cool proto-galaxy gas to a temperature of about 10^4 K. For gas assembled in the fast accretion region, the density is initially a factor of $(c/c_f)^3$ as large as the virial density. The gas density is further increased by a factor of $1/f_{\text{gas}}^3$ as it becomes self-gravitation. Thus,

$$n_{\text{gas}} = \frac{200 n_{\text{B},0} c^3}{\Omega_{m,0} c_f^3 f_{\text{gas}}^3}, \quad (34)$$

where $n_{\text{B},0} \approx 2.5 \times 10^{-7} \text{ cm}^{-3}$ is the mean cosmic baryon number

density of the present-day universe. Assuming $c/c_f = 4$ and $f_{\text{gas}} = 0.15$, we get $n_{\text{gas}} \sim 1.0 \text{ cm}^{-3}$. The corresponding Jeans mass is

$$M_J \sim 5 \times 10^7 M_\odot. \quad (35)$$

This suggests that the original gas in an SGC can fragment to form gas sub-clouds with masses similar to M_J . These clouds will collapse and cool further to form stars. Note that the mass is similar to that of a giant molecular cloud (GMC) complex observed in star-forming galaxies. In what follows, we refer to such clouds as sub-clouds, or ‘sc’ for short.

When gas cooling is effective, the density of a sub-cloud generated by shock compression is typically

$$\rho_{\text{sc}} \sim \mathcal{M}^2 \rho_{\text{SGC}} \sim \left(\frac{V_{\text{SGC}}}{c_s}\right)^2 \rho_{\text{SGC}}, \quad (36)$$

where \mathcal{M} is the Mach number of the shock, c_s is the sound speed of the gas, and V_{SGC} is the virial velocity of the SGC. The number of collisions experienced by a sub-cloud as it moves over the size of an SGC is expected to be

$$N_c \sim \frac{\rho_{\text{sc}} r_{\text{sc}}}{\rho_{\text{SGC}} r_{\text{SGC}}} \sim \left(\frac{r_{\text{sc}}}{r_{\text{SGC}}}\right) \left(\frac{V_{\text{SGC}}}{c_s}\right)^2 \sim 100 \left(\frac{r_{\text{sc}}}{r_{\text{SGC}}}\right). \quad (37)$$

To avoid frequent collisions, sub-clouds must have sizes

$$r_{\text{sc}} < r_{\text{SGC}}/100. \quad (38)$$

The typical mass of such a sub-cloud is

$$M_{\text{sc}} \sim \rho_{\text{sc}} r_{\text{sc}}^3 \quad (39)$$

$$\sim \left(\frac{V_{\text{SGC}}}{c_s}\right)^2 \left(\frac{r_{\text{sc}}}{r_{\text{SGC}}}\right)^3 M_{\text{SGC}} \quad (40)$$

$$\sim \left(\frac{V_{\text{SGC}}}{c_s}\right)^2 \left(\frac{r_{\text{sc}}}{r_{\text{SGC}}}\right) M_{\text{SGC}} \left(\frac{r_{\text{sc}}}{r_{\text{SGC}}}\right)^2 \quad (41)$$

$$\sim M_{\text{SGC}} \left(\frac{r_{\text{sc}}}{r_{\text{SGC}}}\right)^2 \sim 10^{-4} M_{\text{SGC}}. \quad (42)$$

This gives $M_{\text{sc}} \sim 10^7 M_\odot$ for $M_{\text{SGC}} \sim 10^{11} M_\odot$, which is similar to the Jeans mass, M_J , expected in an SGC. Thus, collisions of sub-clouds is expected to be infrequent. The same argument also suggests that the ram pressure on such sub-clouds is unimportant. These together indicate that the high-density sub-clouds, which inherit the large-scale turbulent motion generated by the gravitational collapse, can move roughly ballistically with velocities similar to that expected from the gravitational potential. In this case, the SGC as a whole is supported by random motion of sub-clouds, forming a dynamically hot system with a spheroidal morphology.

Q2: Self-gravitating unstable disks

In the second quadrant where the collapse is in the slow accretion phase, the gravitational potential is roughly static, and the collapse is similar to that of secondary infall onto an existing static potential. Since all halos must start from the fast assembly phase, we expect that a galaxy in this quadrant has evolved from the first quadrant. The value of f_λ remains high, indicating that f_{gas} has not been reduced significantly by feedback and ineffective cooling. The radiative cooling efficiency described in §3.1 indicates that only low-mass halos with $M_v < 10^{13} M_\odot$ can evolve to this quadrant.

As the mass assembly is dominated by radial infall in this case, gas clouds can reach the central halo region to dissipate and become supported by angular momentum to form a disk-like structure. However, since $f_\lambda > 1$, such a disk is dominated by self-gravity and is

thus unstable both locally and globally. This is expected to lead to the formation of clumpy disks due to local instabilities of the self-gravitating disk, and/or bar-like structures due to the global instability of the disk. Both of these can cause migrations of cold gas towards the central region of a galaxy, a process referred to as the compactification (e.g. Dekel et al. 2009; Dekel & Burkert 2014; Zolotov et al. 2015; Tacchella et al. 2016; Ji & Giavalisco 2023), leading to star formation and perhaps the growth of a bulge-like component near the center. The reduction of cold gas causes f_λ to decrease. Since γ changes only slowly in the slow assembly phase, a nearly vertical, downward evolution is expected in the quadrant diagram.

Q3: Rotation-supported cold disks

In the third quadrant, the gravitational potential is roughly static and f_λ is about one or below. These are the conditions for the formation of a stable cold disk. In order for the disk to fragment and form stars, it needs to be locally unstable, i.e. $f_\lambda \sim 1$. If λ is too large and/or f_{gas} too small so that $f_\lambda \ll 1$, the gaseous disk will become too stable to form stars. This can lead to the formation of a low surface brightness disk if most of the disk material is assembled in such a way.

A galaxy can evolve to this quadrant from Q2 as the amount of cold gas in the disk is reduced by the compactification. As to be described below, a galaxy may also evolve to this quadrant from Q4 when the amount of cold gas is reduced by processes associated with the fast assembly phase before the halo moves to the slow assembly phase. This evolutionary path is similar to the preventative scenario investigated in Mo & Mao (2004) and Lu et al. (2015), where starburst and AGN feedback associated with the fast assembly phase can reduce the amount of gas to be accreted by the halo in the slow assembly phase.

Q4: Disturbed and quenched galaxies

In the fourth quadrant, the halo assembly is still in the fast phase so the gravitational potential can change significantly. However, since $f_\lambda < 1$, the collapse of the gas for it to become dense enough to form stars will be halted by angular momentum. A disk can then be produced in the interval where major mergers are not involved, but the disk cannot remain cold because of the change of the gravitational potential. This may produce a thick disk with significant random motion. In the extreme case where a significant merger is involved in the assembly, which causes a spike in γ , the disk that has formed may be disrupted, producing a merger remnant. The above is expected to be true in halos where the amount of cold gas is still significant. If, on the other hand, radiative cooling is inefficient, such as in a massive halo, and/or feedback has eliminated the cold gas in the galaxy, the galaxy will be quenched. As mentioned above, if the halo makes a transition to the slow assembly regime, i.e. moves to Q3, a thin disk may grow around the structure that has formed in Q4.

As one can see from Fig. 1, although the overall assembly history can be separated into a fast phase followed by a slow phase, individual histories in general contain fluctuations on small time scales. Thus, a halo in the fast assembly phase can make excursions to the slow assembly regime and vice versa. Since the typical time for a perturbed self-gravitating system to settle to a new quasi-static structure is its dynamical time scale, a bulge-like galaxy in Q1 may thus make an excursion to a disk-like morphology in Q2 if the time interval of the excursion in Q2 is longer than the dynamical time, and vice versa. In Appendix C, we present various statistics for the fluctuations and

the excursions based on halo assembly histories and the change of binding energy of dark matter particles. Clearly, the binding energies of particles respond well to fluctuations in γ , even for particles in the inner part of the halo, indicating that the value of γ indeed characterizes the dynamic state of the halo. The number of excursions to the slow regime ($\gamma < \gamma_f$) during the fast phase ($z \geq z_f$) is ≤ 2 for about 80% halos, and ≤ 3 for all halos, regardless of the transition threshold γ_f adopted. The total time spent in the slow regime takes up to 30% of the fast phase for about 80% halos, and 40% for all halos. This indicates that most halos have a chance of excursion to a disk-like morphology, but then return back to a bulge-like morphology after a short period. In a forthcoming paper (Chen et al. in prep) we will examine in detail how galaxies evolve in the four-quadrant diagram using numerical simulations, and develop a detailed model for such evolution. In this paper, we only focus on some key points and demonstrate generic trends expected from the scenario.

3.4 Further justifications of model assumptions

One assumption in our modeling is that SGC is spherical. This is clearly a simplification given that the assembly of a dark matter halo is typically non-spherical and clumpy. However, in the fast assembly phase, the gravitational potential well deepens rapidly with time. Since feedback from star formation and SMBH growth (see below) is expected to be more effective in heating and dispersing gas in lower-mass halos with shallower gravitational potential wells, most of the gas associated with the progenitors of a halo cannot form stars before the assembly of the final halo in the end of the fast assembly phase, where the gravitational potential well is able to retain more gas. It is thus likely that most of the gas in a halo is not bound to dark matter substructures, such as subhalos, as it cools and collapses to form the SGC (see, e.g. figure 7 of Tillson et al. 2015). The situation is similar to what Latif et al. (2022) found in their simulations of the formation of gas collapse in galaxies, where ineffective cooling of metal-poor gas prevents star formation in substructures until the whole cloud becomes self-gravitating and collapses. Such a cloud is more or less spherical in the absence of angular momentum support. Consequently, the details of the halo assembly history may be irrelevant to the formation of the SGC.

A similar argument may also be made for the enrichment history of an SGC. If most stars formed in the SGC, instead of in substructures before the assembly of the SGC, then the metallicity of the gas is expected to increase quickly to a roughly constant value as stars form and evolve in the SGC. This is actually consistent with the observed uniformity in the stellar population of early-type galaxies. However, if one is interested in the formation of different stellar populations in galaxies, e.g. globular clusters, the details of the chemical enrichment need to be followed, as described in Chen et al. (2024).

Another simplification in §3.3 for the formation of SGC is the omission of the response of the dark matter to the collapse of gas. Following the model of Mo et al. (1998), we used adiabatic contraction to estimate this response, assuming spherical symmetry. We found that, for the typical concentration, $c_f \approx 4$, the change in the radius of an SGC by adiabatic contraction is within 20 percent as f_{gas} changes from 0.025 to 0.16. However, during the fast assembly phase, the rapid change of the gravitational potential and the fast growth of the SGC may make the adiabatic assumption invalid. Another complication, found in numerical simulations (e.g. Dutton et al. 2016; El-Badry et al. 2016) arises from feedback-driven outflow, which may ‘heat’ dark matter particles and reverse the contraction. Given the small effect of adiabatic contraction on the size of SGC and uncertainties in modeling it, we will ignore the effect in our model.

The detailed flow of the halo gas feeding the SGC is difficult to model analytically. However, high-resolution zoom-in simulations of individual galaxies published previously may provide some clues. [Ceverino et al. \(2010\)](#) performed simulations of three MW-size galaxies using a spatial resolution of 35–70 pc. They found that, at $z > 2$ these galaxies are fed by steady cold streams from locations well outside the virial radius of the host halo to the inner core. The streams appear to converge at about $0.3R_v$, resulting in violent interactions and producing strong turbulence (see their figure 3). In all cases, the gas medium generated is clumpy and turbulent, consisting of dense clumps with active star formation. For the three cases simulated, the structure of the stellar component appears flattened (resembling a thick disk) and contains strong turbulent motion, with a radius about $0.05\text{--}0.1R_v$. This is consistent with the expectation for a system in Q2 or Q4 described above. [Danovich et al. \(2015\)](#) expanded the investigation of [Ceverino et al. \(2010\)](#) by using 29 galaxies covering a wider range of masses and simulated with comparable spatial resolutions. They found that these galaxies are roughly fed by three cold streams. The major stream usually has an impact parameter of $0.3R_v$, while the other two streams have smaller impact parameters. All the streams penetrate the inner core of the halo and are stopped at about $0.3R_v$ where they collide. They also found that about 30% of the steam mass is counter-rotating to the net angular momentum of the gas so that gas can be strongly compressed. This provides the condition for the formation of dense sub-clouds envisaged in §3.3. The gaseous structures in their simulated galaxies are in general very clumpy and turbulent, particularly at high redshift (see their figure 17), which reflects the fact that halo accretion is faster at higher z , as described in §2.

As we assume in our model below, the star formation in the SGC is associated with dense sub-clouds. At high redshift, e.g. $z \sim 10$, the typical scale of an SGC is $\lesssim 1$ kpc (see also [Dekel et al. 2023](#)). Using Eq. (38) for r_{sc}/r_{SGC} , we expect that the size of a sub-cloud is typically $\lesssim 10$ pc, comparable to that of a young massive star cluster (YMSC) or a globular cluster (GC) observed in the local Universe (see e.g. [Krumholz et al. 2019](#), for a review). The detailed star formation processes at this scale involve complex physics, such as the cooling by dust, metals and molecules, and the feedback from stars. These are difficult to resolve computationally, even in zoom-in simulations of individual galaxies discussed above. [Mandelker et al. \(2018\)](#) used an analytical approach to model the stream accretion and star formation in SGCs. Assuming cylindrical contraction and angular-momentum conservation, they found that high-density sub-clouds can form in a metal-poor ($Z \approx 0.02Z_\odot$) SGC at $z \gtrsim 6$ in the core region ($R \lesssim 0.3R_v$) of a stream-fed halo, prior to the onset of gravitational instability. The criteria can be further relaxed in the presence of gravitational instability in sub-clouds, or if cold streams collide with each other to produce supersonic shocks that compress the gas. [Ma et al. \(2018\)](#) used GIZMO to perform a set of zoom-in simulations in volumes around 15 halos at $z \gtrsim 5$ selected from the FIRE-2 project, achieving a sub-pc (in physical units) spatial resolution. All the central galaxies in their sample appear clumpy and irregular in the redshift range covered by their simulations (see the mock images in their figures 2 and 3 for examples at $z = 5$ and 10, respectively), and none of them resembles a disk or elliptical galaxy in the local Universe. The star formation histories of these galaxies all contain frequent bursts that typically last a period of 50–100 Myr. These results are consistent with the formation of dynamically hot systems in the Q1 phase described in §3.3. [Ma et al. \(2020\)](#) re-ran simulations for a number of the 15 halos using a mass resolution eight times better than that in the original simulations, focusing on narrow time windows of 100 Myr containing starbursts. They

found that the gas-rich, turbulent environment originated from fast halo accretion and/or feedback-driven winds naturally give birth to high-density sub-clouds from which bound star clusters form. This supports the scenario of the formation of dense sub-clouds described in §3.3. They also confirmed that bound cluster formation ceases at lower redshift, due to the less dense and less turbulent galactic environment (see their figure 17, at $z = 1$). However, the sizes of their simulated bound star clusters (see their figure 13) are much larger than the observed size of YMSCs and GCs, and the number of bound clusters does not appear to reach convergence even at the highest resolution they used (see their figure 16), indicating that the conditions for the formation of sub-clouds and star clusters are not reproduced in the simulation. Instead of simulating the entire galaxies, [Grudić et al. \(2021\)](#) focused on individual GMCs with turbulence field injected artificially. The sizes of simulated bound clusters now appear to converge to the observed range (see their figure 7). A related investigation was carried out by [Latif et al. \(2022\)](#), who focused on extremely metal-poor gas (with pristine composition) at $z \gtrsim 20$ using the Enzo code with a spatial resolution that reaches ~ 20 AU. They found that turbulence compression due to global collapse and cloud mergers, and the delayed star formation due to inefficient cooling, give birth to massive and dense gas clumps that can host massive stars of $\gtrsim 10^4 M_\odot$ and probably provide a channel to seed SMBHs.

The above presentation shows that the scenario of SGC formation and fragmentation to produce sub-clouds envisaged in our model has support from high-resolution hydro simulations. It is also clear that there are still substantial amounts of uncertainties in current simulations, related particularly to resolving sub-clouds and sub-grid physics in modeling star formation. These not only affect the predicted properties of sub-clouds and star clusters, but also have impacts on the structure and dynamics of galaxies on large scales. For instance, if the fragmentation of an SGC to form dense sub-clouds is not properly resolved, the dissipation of turbulent motion by cloud-cloud collision may be overestimated. This, in turn, may lead to an overestimate of dynamically colder galaxies. Similarly, uncertainties in modeling the feedback from star formation in a sub-cloud can lead to incorrect predictions for the dissipation of the orbital energy of sub-clouds, again affecting the hotness of the predicted galaxies.

Some justifications may also be obtained from observations. The newly-launched JWST has already been able to resolve, albeit only for a few cases in strongly lensed fields, the formation of dense star clusters at high redshift. Together with multi-wavelength observations from, e.g., HST, ALMA and VLT, the JWST data can be used to measure a rich set of properties of high- z galaxies. Current samples are still small. The limited analyses indicate that high- z galaxies are in general very clumpy, containing clumps with sizes similar to those of YMSCs and GCs observed in the local universe (e.g. [Vanzella et al. 2022](#); [Lin et al. 2023](#); [Vanzella et al. 2023](#); [Fujimoto et al. 2024](#); [Mowla et al. 2024](#); [Adamo et al. 2024](#)). The global morphology of these galaxies appears to be diverse. In particular, a significant fraction of them show flattened shapes and nearly exponential light profiles (e.g. [Ferreira et al. 2023](#); [Lee et al. 2023](#); [Kuhn et al. 2023](#); [Kartaltepe et al. 2023](#); [Ormerod et al. 2024](#); [Sun et al. 2024](#); [Tohill et al. 2024](#)). However, it is unclear if these galaxies are rotation-supported, dynamically cold disks. Indeed, some recent analyses demonstrated that many of these flattened galaxies are consistent with being dynamically hot systems flattened by velocity anisotropy velocity (e.g. [Pandya et al. 2024](#); [Vega-Ferrero et al. 2024](#)). This issue is expected to be resolved in the near future as samples and analyses of observational data accumulate.

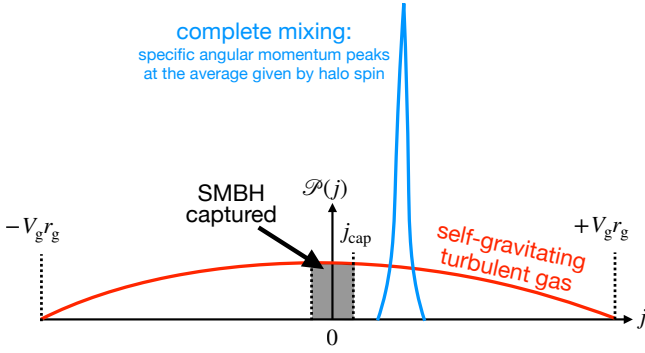


Figure 4. A schematic diagram showing the distribution of specific angular momentum (j) for gas clouds within a halo. The turbulent motion of gas clouds, driven by fast accretion, yields a broad and uniform distribution (red curve) of j . The fraction of gas accreted by the SMBH (gray shaded area) is determined by the maximum capturing angular momentum, j_{cap} . Subsequently, as the driving force of turbulent motion diminishes, gas mixing becomes significant, leading to the emergence of an angular momentum barrier and preventing gas accretion (blue curve). See §4.1 for a detailed discussion on SMBH accretion. This diagram shows the mechanism underlying the formation of dynamically hot systems, the accretion scenario of SMBH within turbulent gas clouds, and the transition to dynamically cold systems.

4 STAR FORMATION AND THE GROWTH OF SUPERMASSIVE BLACK HOLES

4.1 Accretion of gas onto a supermassive black hole

When the turbulent medium is fully developed, high-density clouds can move almost ballistically, as discussed above. We can then use the loss-cone argument (Shapiro & Teukolsky 1986) to estimate the mass that can be captured by a supermassive black hole (SMBH) (e.g. Hobbs et al. 2011). The fraction of the gas mass in a shell of mass ΔM_g and radius r_g that can reach the central SMBH of mass M_{bh} at an impact parameter smaller than r_{acc} is

$$\frac{\Delta M_{\text{acc}}}{\Delta M_g} \approx \frac{j_{\text{cap}}}{V_g r_g} \quad (43)$$

where V_{tb} is the typical large-scale turbulent velocity, and

$$j_{\text{cap}} = \sqrt{2GM_{\text{bh}}r_{\text{acc}}}. \quad (44)$$

For turbulence driven by gravitational collapse, we expect that $V_{\text{tb}} \sim V_g$, where V_g is the typical velocity in the gravitational potential of the proto-galaxy in question. The above relation can be understood as follows. Setting $V_{\text{tb}} = V_g$ in the above relation, we have

$$\frac{\Delta M_{\text{acc}}}{\Delta M_{\text{tb}}} = \frac{j_{\text{cap}}}{V_g r_g}. \quad (45)$$

This implies that the distribution of the specific angular momentum is uniform in mass between $j \sim 0$ to $j = j_{\text{max}} \sim V_g r_g$. A turbulent medium can produce such a distribution by randomizing the velocity. Consider a gas cloud of a given speed V in a spherical shell of a given radius r . The specific angular momentum of the cloud is $j = Vr \sin \theta$, where θ is the angle between the velocity vector and the radial vector at the location of the cloud. If the velocity has a random distribution in direction, then the solid angle element $2\pi \sin \theta d\theta$ has a uniform distribution.

We can estimate r_{acc} by requiring that the gravitational potential of the SMBH must be able to capture clouds moving at a speed

$\sim V_{\text{tb}} \sim V_g$. This gives

$$r_{\text{acc}} \sim \frac{GM_{\text{bh}}}{V_g^2} \sim \frac{M_{\text{bh}}}{M_g} r_g. \quad (46)$$

We thus have

$$\frac{\Delta M_{\text{acc}}}{\Delta M_g} = \frac{j_{\text{cap}}}{V_g r_g} = \alpha_{\text{cap}} \frac{M_{\text{bh}}}{M_g}, \quad (47)$$

where α_{cap} is a constant of order unity. Thus, if $\Delta M_{\text{acc}} = \Delta M_{\text{bh}}$, then we would have $M_{\text{bh}} \propto M_g$. As we will see later, star formation feedback may change this relationship, increasing the value of α_{cap} .

Since we are concerned with the feeding of SMBH, it is interesting to cast the above relation into a rate relation and write it in terms of the Eddington rate of M_{bh} ,

$$\dot{M}_{\text{Edd}} = \frac{M_{\text{bh}}}{\tau_{\text{Edd}}}, \quad \tau_{\text{Edd}} \approx 4.4 \times 10^8 \epsilon_r \text{ yrs}, \quad (48)$$

where $\epsilon_r \sim 0.1$ is the radiation efficiency of a black hole. Equation (47) can then be written in the following form

$$\dot{M}_{\text{acc}} = \alpha_{\text{cap}} \frac{\tau_{\text{Edd}}}{\tau_g} \dot{M}_{\text{Edd}}, \quad (49)$$

where $\tau_g \sim t_{\text{ff}}$ is the typical time scale for a gas sub-cloud to move across the galaxy once. For an SGC, we can use equations (17) and (28) to obtain

$$t_{\text{ff,SGC}} \approx \left[\frac{f_{\text{gas}}^2}{200} \left(\frac{c_f}{c} \right)^3 \right]^{1/2} t_{\text{H}}, \quad (50)$$

where t_{H} is the Hubble time. Assuming $f_{\text{gas}} = 0.15$ and $c/c_f = 2$, we get $t_{\text{ff,SGC}} \sim t_{\text{H}}/300 \sim 5 \times 10^7 \text{ yrs}$. This is comparable to τ_{Edd} for $\alpha_{\text{cap}} \sim 1$, suggesting that the accretion rate in an SGC can reach the Eddington limit. As we will describe below, the value of α_{cap} may be increased if supernova feedback can replenish the SGC with SMBH-feeding gas, making super-Eddington accretion possible.

Note that the above results are only valid for a fully turbulent gas. As the driving force decreases and the mixing of gas becomes important, the angular momentum barrier will develop and prevent gas accretion. This may occur when feedback can heat most of the gas, as well as in late times when the accretion is slow. For convenience, Fig. 4 gives a schematic illustration of the angular momentum distribution and the SMBH accretion scenario described here.

4.2 Star formation in self-gravitating clouds (SGC)

The star formation efficiency in individual gas sub-clouds can be defined as

$$\epsilon_{\text{sc}} = \frac{\dot{M}_{*,\text{sc}} t_{\text{ff,sc}}}{M_{\text{sc}}}, \quad (51)$$

where $\dot{M}_{*,\text{sc}}$ is the star formation rate, and $t_{\text{ff,sc}}$ the free-fall time of the sc. Based on observations of star formation in giant molecular clouds (GMC), the star formation efficiency in general is very low, typically 0.01 (e.g. Krumholz & Tan 2007; Feldmann & Gnedin 2011; Chevance et al. 2020). Suppose that the time scale for the formation of a sc is τ_{sc} . The efficiency at which gas is converted into stars in an SGC is then

$$\epsilon_{\text{SGC}} = \epsilon_{\text{sc}} \frac{t_{\text{ff,SGC}}}{\tau_{\text{sc}}}. \quad (52)$$

In a self-gravitating medium, the formation time of a sub-cloud is typically its free-fall time, so that $\tau_{\text{sc}} \sim t_{\text{ff,sc}}$. In a turbulent SGC, $t_{\text{ff,SGC}}/t_{\text{ff,sc}} \sim V_{\text{SGC}}/c_s \sim 10$. So the typical value of ϵ_{SGC} is about

0.1, comparable to the star formation efficiency required by the stellar mass-halo mass relation. This suggests that star-forming sub-clouds have to be dispersed and recreated about 10 times or more in an SGC.

A constraint on the star formation scale can also be obtained by using the fact that stars in elliptical galaxies are in general enhanced in α elements produced mainly by SNa II. The progenitors of these supernovae have masses $> 8M_{\odot}$, which have main-sequence lifetime about 10^7 yrs. Type Ia supernovae, which are the main sources of Fe, have progenitor masses about $3M_{\odot}$, with lifetime $> 10^8$ yrs. Thus the time scale of star formation must be about 10^8 yrs. This is comparable to the free-fall time scale of an SGC.

For the high-density tail of the gas distribution in an SGC, analytical models (e.g. [Dekel et al. 2023](#)) and numerical simulations (e.g. [Grudić et al. 2021](#)) suggest that the local free-fall time scale can be as short as 1 Myr and the local star formation efficiency can reach the order of unity. Such high-density sub-clouds naturally emerge in Q1 as a consequence of the high SGC density, strong compression associated with supersonic turbulence, and low gas metallicity expected at high z (see §3.3). This can lead to the formation of compact stellar systems such as young massive star clusters and globular clusters, and we will investigate them in the third paper of this series ([Chen et al. 2024](#)).

4.3 Feedback and quenching

Both supernovae and accreting SMBHs can deposit energy in the SGC. Using a rate of one supernova per $125M_{\odot}$ of stars, and a kinetic energy of 10^{51} ergs per explosion, we can write the cumulative feedback energy gain per gas mass as

$$E_{\text{sn}} \approx (630 \text{ km s}^{-1})^2 \epsilon_{\text{sn}} f_*, \quad (53)$$

where $f_* = M_*/M_g$ and ϵ_{sn} is the efficiency at which the supernova feedback energy can affect the gas component. For the feedback by an accreting SMBH, the corresponding expression can be written as

$$E_{\text{bh}} \approx (3 \times 10^3 \text{ km s}^{-1})^2 \epsilon_{\text{bh}} f_* \left(\frac{f_{\text{bh}}}{10^{-4}} \right), \quad (54)$$

where $f_{\text{bh}} = M_{\text{bh}}/M_*$, and ϵ_{bh} is the efficiency at which the feedback energy of the SMBH can affect the gas component. The main uncertainty is in the values of ϵ_{sn} and ϵ_{bh} , as the feedback energy can be lost through radiation and/or leaked without affecting the gas component. [Dekel & Silk \(1986\)](#) modeled the evolution of supernova remnants in a uniform medium taking into account radiative cooling, and found that ϵ_{sn} depends on the number density of supernova explosions. In a high-density, star-forming gas where supernova remnants can overlap before radiative cooling becomes important, $\epsilon_{\text{sn}} \sim 1$. Assuming $\epsilon_{\text{sn}} f_* \sim 0.1$, as may be appropriate in an SGC, supernova feedback is expected to be effective in halos with virial velocity $V_V < 200 \text{ km s}^{-1}$. For $\epsilon_{\text{bh}} \sim 0.1$ and $f_* \sim 0.2$, and for f_{bh} as low as 10^{-4} , the corresponding limit is $V_V \sim 400 \text{ km s}^{-1}$, indicating that SMBH might be able to drive outflows from relatively massive halos.

4.3.1 Feedback from accreting supermassive black holes

The total energy produced by an accreting SMBH (AGN) is:

$$E_{\text{bh}} = \epsilon_{\text{bh}} M_{\text{bh}} c^2, \quad (55)$$

where $\epsilon_{\text{bh}} \sim 0.1$ is an efficiency factor. We assume that a fraction of f_E of the feedback energy is coupled to the gas:

$$E_{\text{cp}} = f_E E_{\text{bh}}, \quad (56)$$

and that the gas coupled to (affected by) the feedback is M_{cp} . If the feedback energy of the AGN is stored in the gas as thermal energy, we can write

$$M_{\text{cp}} = \frac{f_E \epsilon_{\text{bh}} M_{\text{bh}} c^2}{w^2}, \quad (57)$$

where w is given by the gas temperature:

$$w^2 = \frac{kT}{\mu m_p}. \quad (58)$$

The fraction of gas that is affected by the feedback is then

$$f_{\text{cp}} = \frac{M_{\text{cp}}}{M_g} = \frac{f_E \epsilon_{\text{bh}} M_{\text{bh}} c^2}{M_g w^2}. \quad (59)$$

Assuming $w^2 \sim V_g^2$, with V_g being the velocity expected in the gravitational potential of the galaxy, the fraction that is not affected by the AGN feedback can be written as

$$F_{\text{agn}}(M_{\text{bh}}, M_g, V_g | \alpha_{\text{agn}}) = 1 - \frac{\alpha_{\text{agn}} M_{\text{bh}} c^2}{M_g V_g^2}, \quad (60)$$

where α_{agn} is a constant parameter. To see the consequence of the feedback, let us assume an isothermal gas and that all gas not locked in stars are affected by the feedback. In this case, we have

$$M_{\text{cp}} = M_g - M_*, \quad (61)$$

and

$$M_{\text{bh}} = \frac{w^2 (M_g - M_*)}{f_{\text{cp}} \epsilon_{\text{bh}} c^2} = \frac{w^2 M_g}{f_{\text{cp}} \epsilon_{\text{bh}} c^2} \left(1 - \frac{M_*}{M_g} \right), \quad (62)$$

where M_*/M_g is an overall star formation efficiency. If we assume that the AGN feedback quenches the SMBH accretion when the gas is heated up to a temperature to escape the gravitational potential of the galaxy, we can set w to be the velocity dispersion of the gravitational potential: $w^2 \sim \sigma_g^2$. For a self-gravitating gas formed in a dark matter halo, $M_g \sim \sigma_g^2 r_g \sim \sigma_g^3$. We then have

$$M_{\text{bh}} \propto \sigma_g^b, \quad (b \sim 5). \quad (63)$$

This is actually similar to the observed value, $b \approx 5.3$ (e.g. [Hu 2008](#); [McConnell & Ma 2013](#); [Woo et al. 2013](#); [Saglia et al. 2016](#); [Greene et al. 2020](#)). If the stellar mass scales with σ_g as

$$M_* \propto \sigma_g^s, \quad (64)$$

then

$$M_{\text{bh}} \propto M_*^{b/s}. \quad (65)$$

The observed value, $s \sim 3$, then implies that $b/s \sim 5/3$, which again is consistent with observational results (e.g. [Greene et al. 2020](#); [Graham & Sahu 2023](#); [Zhuang & Ho 2023](#)). More recently, [Hong et al. \(2023\)](#) adopted a similar approach and applied it to MaNGA galaxies. They successfully connected the observed Faber-Jackson relation (eq. 64) and black hole scaling relations (eqs. 63 and 65).

4.3.2 Ineffective cooling at the high-mass end

At the massive end, radiative cooling becomes inefficient. Feedback may then quench the star formation and SMBH growth in a galaxy, even if its halo is still in the fast-assembly phase. The cooling curve suggests that, for halos above $M_{\text{cool}} \sim 10^{12} M_{\odot}$ and for the density expected for halo gas at the virial temperature, the ratio between the cooling time and free-fall time is roughly proportional to halo mass, M_V , quite independent of redshift (see Fig. 2). Thus, we need to include an additional halo mass-dependent factor, F_{cool} , to describe the fraction of cooled gas, as is given by Eq. (23).

4.3.3 Modifications at the low-mass end, and the enhancement of supermassive black hole accretion

According to the supernova energy output and rate, the specific energy gained by a sub-cloud due to supernovae associated with star formation can be written as

$$\mathcal{E}_{\text{sc}} = (40 \text{ km s}^{-1})^2 \left(\frac{\epsilon_{\text{sc}}}{0.01} \right) \left(\frac{\epsilon_{\text{sn}}}{0.5} \right), \quad (66)$$

where $\epsilon_{\text{sc}} \sim 0.01$ is the star formation efficiency in a sub-cloud (sc) and the value is based on that in a GMC; ϵ_{sn} is the fraction of supernova kinetic energy that is injected into the gas. Thus, supernovae in a sub-cloud are expected to disperse the gas from a sub-cloud, rather than to directly drive gas out of the galaxy potential. However, such dispersed gas can make the feedback from the central starburst, where the effective ϵ_* is much higher than ϵ_{sc} , more effective in loading the feedback energy onto the gas. In low-mass halos where the gravitational potential wells are shallow, the feedback may drive gas out of the central galaxy, reducing the amount of gas. One possibility to model the combined effect of supernova and AGN feedback is to replace F_{agn} defined above by

$$F'_{\text{agn}} = F_{\text{agn}} F_{\text{sn}}, \quad (67)$$

where

$$F_{\text{sn}}(V_{\text{g}}|\alpha_{\text{sn}}, \beta_{\text{sn}}, V_{\text{w}}) = \frac{\alpha_{\text{sn}} + (V_{\text{g}}/V_{\text{w}})\beta_{\text{sn}}}{1 + (V_{\text{g}}/V_{\text{w}})\beta_{\text{sn}}}, \quad (68)$$

with $\alpha_{\text{sn}} \leq 1$, $\beta_{\text{sn}} > 0$, and V_{w} a characteristic velocity. The assumption made in Eq. 67 is that supernova feedback and AGN feedback operate conditionally, so that the former only operates on the remaining gas fraction allowed by the latter, and vice versa. This is similar to the preferred scheme proposed by Booth & Schaye (2013), in which the effect of the weaker feedback is conditioned on the result of the more dominating one. As one can see, the combined effect of supernova and AGN feedback is to eject part of the gas from (low-mass) halos, while heating part or all of the remaining gas to the virial temperature.

The feedback process can also generate turbulence in the gas. In central regions of low-mass halos where radiative cooling is very effective, some of the gas affected by the feedback may cool, reproducing clouds with low specific orbital angular momentum and enhancing the mass accretion rate of the central SMBH. Unfortunately, the details of this ‘positive’ feedback are yet to be understood. To model the effect, we include the following factor in the accretion rate of SMBH:

$$F_{\text{en}}(M_{\text{v}}|\alpha_{\text{en}}, \beta_{\text{en}}, M_{\text{en}}) = \frac{\alpha_{\text{en}} + (M_{\text{v}}/M_{\text{en}})\beta_{\text{en}}}{1 + (M_{\text{v}}/M_{\text{en}})\beta_{\text{en}}}, \quad (69)$$

where β_{en} describes the transition from α_{en} at the low-mass end to one at the high-mass end, with α_{en} , β_{en} and M_{en} being model parameters. We assume that this positive feedback is important only in the central dense part of an SGC, and will not affect much the total star formation rate in the entire SGC.

4.4 Co-evolution of different mass components during the fast assembly

In practical applications, the evolution of halos can be modeled reliably using merging trees obtained from numerical simulations. To model the evolution of baryonic components in a halo, we start by introducing a small baryonic seed in the earliest progenitor of the halo and follow the evolution step by step using a set of equations relating different mass components. Based on the discussion presented

in the preceding sections, we outline the evolutionary equations as follows. Note that the prescriptions are for halos in the fast assembly phase (i.e. $z \geq z_{\text{f}}$). The evolution in the slow assembly phase will be presented later.

- (i) **Initialization:** In the first snapshot of the main branch of a dark matter halo, we set the initial stellar mass $M_{*,\text{init}}$ and gas mass $M_{\text{g},\text{init}}$ in the halo as follows:

$$M_{*,\text{init}} = 0; \quad (70)$$

$$M_{\text{g},\text{init}}(M_{\text{v}}) = f_{\text{B}} M_{\text{v}}. \quad (71)$$

When the halo mass M_{v} exceeds a threshold, $M_{\text{v},\text{min}}$, we seed a black hole with a mass $M_{\text{bh},\text{init}}$ proportional to M_{v} :

$$M_{\text{bh},\text{init}}(M_{\text{v}}|M_{\text{bh},\text{min}}, m_{\text{bh},\text{scale}}) = \max(M_{\text{bh},\text{min}}, m_{\text{bh},\text{scale}} M_{\text{v}}), \quad (72)$$

where $m_{\text{bh},\text{scale}}$ determines the initial black hole mass, and $M_{\text{bh},\text{min}}$ is a small value used to prevent the black hole mass from being too small.

- (ii) **Total amount of available gas:** The total amount of gas available in a halo is determined by the newly-accreted halo mass, ΔM_{v} , in each snapshot, through

$$\Delta M_{\text{g},\text{avail}} = f_{\text{B}} \Delta M_{\text{v}}. \quad (73)$$

- (iii) **Cooling of halo gas:** A fraction of the available halo gas cools down and contributes to the SGC. We define the amount of ‘cooled gas’ as

$$\Delta M_{\text{g},\text{cool}} = F_{\text{cool}} \Delta M_{\text{g},\text{avail}}, \quad (74)$$

where $F_{\text{cool}}(M_{\text{v}}|M_{\text{cool}}, \beta_{\text{cool}})$ is defined by equation (23). The remaining gas is referred to as the ‘hot gas’:

$$\Delta M_{\text{g},\text{hot}} = (1 - F_{\text{cool}}) \Delta M_{\text{g},\text{avail}}. \quad (75)$$

It is important to note that once the cooled gas becomes fully turbulent, the global cooling function may no longer be valid. For instance, Ji et al. (2019) suggested that the cooling of turbulent gas is dominated by mixing layers with temperatures located at the peak of the cooling function.

- (iv) **Feedback mechanisms:** The combined effect of supernova and AGN feedback results in the ejection and/or heating of the cooled gas. As a result, only a fraction of the cooled gas is able to effectively form stars and feed the SMBH. Therefore, we define the ‘star-forming gas’ as

$$\Delta M_{\text{g},\text{sf}} = F_{\text{agn}} F_{\text{sn}} \Delta M_{\text{g},\text{cool}}, \quad (76)$$

where $F_{\text{agn}}(M_{\text{bh}}, M_{\text{g}}, V_{\text{g}}|\alpha_{\text{agn}})$ and $F_{\text{sn}}(V_{\text{g}}|\alpha_{\text{sn}}, \beta_{\text{sn}}, V_{\text{w}})$ are defined by Eqs. (60) and (68), respectively. In our implementation, we define V_{g} as the maximum circular velocity, V_{max} , of the host halo, as the turbulent motion of the gas is driven by the gravity of the galaxy.

- (v) **Star formation and SMBH accretion:** The star formation rate (SFR) is expected to be related to the amount of cold gas available for star formation. In general, we can express this as

$$\Delta M_{*}(\Delta M_{\text{g},\text{sf}}|\epsilon_{*,\text{f}}) = \epsilon_{*,\text{f}} \Delta M_{\text{g},\text{sf}}, \quad (77)$$

where $\epsilon_{*,\text{f}} < 1$ represents the overall star formation efficiency in the fast assembly phase. Note that $\epsilon_{*,\text{f}}$ is included to reflect the fact that a small part of the star-forming gas may be locked in stellar remnants and in a cold ISM. Stars formed during the fast phase are expected to reside in a hot bulge or a hot disk, as indicated by the Q1 and Q4

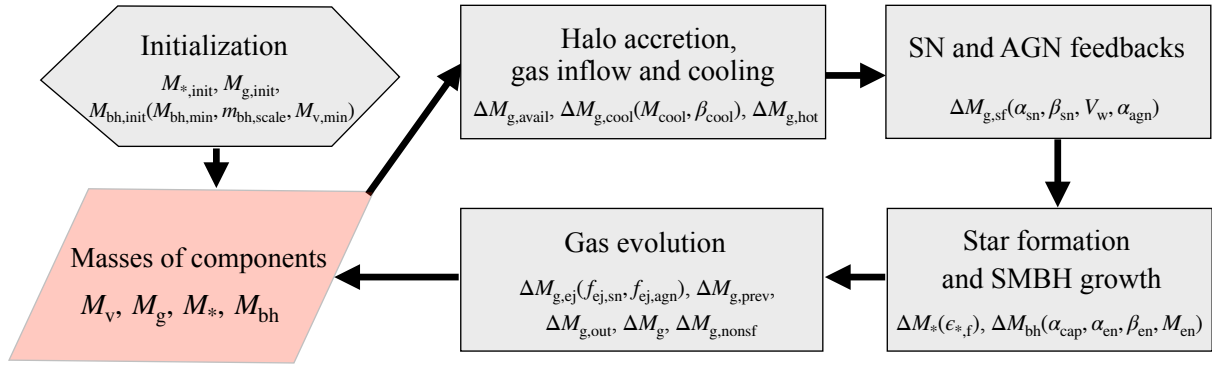


Figure 5. A flow diagram showing the model for the evolution of different mass components (shown in **red block**, including halo mass M_v , gas mass M_g remaining in SGC, stellar mass M_* and SMBH mass M_{bh}) during the fast assembly phase. The algorithm initializes the mass components at the initial snapshot and iteratively updates them until the ending point of the fast assembly. Each **gray block** shows a process, including the relevant physical quantities and model parameters. See §4.4 for a complete description of the evolutionary equations and Table 1 for a list of the model parameters adopted in this paper.

quadrants, respectively, in the quadrant diagram. In what follows, we refer to these two hot components collectively as the ‘bulge’. Since the SMBH growth occurs also during this turbulent phase, we can express it using equation (47) as

$$\Delta M_{bh} = \alpha_{cap} \frac{M_{bh}}{M_g} F_{en} F_{tb} \Delta M_{g,sf}, \quad (78)$$

where $F_{en}(M_v | \alpha_{en}, \beta_{en}, M_{en})$ represents the enhancement factor defined by equation (69), and $F_{tb} \equiv \Delta M_{tb} / \Delta M_g$ is the mass fraction of the turbulent gas, which is set to 1 due to its degeneracy with α_{cap} . If the combined effects of F_{cool} , F_{sn} and F_{agn} make $\Delta M_{g,sf}$ negligible, we have $\Delta M_{g,sf} \approx 0$. Consequently, both $\Delta M_* \approx 0$ and $\Delta M_{bh} \approx 0$, indicating the onset of a quenching regime. On the other hand, if certain processes lead to a very small value of F_{tb} , indicating that most of the gas moves in a non-turbulent (smooth) fashion, then we have $\Delta M_{bh} \approx 0$ while $\Delta M_* \neq 0$. This scenario corresponds to the smooth accretion in the slow phase, where the gas is likely to settle into a rotation-supported disk. In this case, a dynamically cold system is formed without affecting M_{bh} .

- (vi) **Evolution of the gas:** The cooled gas ($\Delta M_{g,cool}$) is affected by feedback processes, so that part of it is ejected from the turbulent region and mixed with the hot gas ($\Delta M_{g,hot}$). The part of the gas that has been affected by the feedback but remains in the SGC is also prevented from forming stars and feeding the SMBH. We refer to it as the ‘prevented gas’ and denote its mass by $\Delta M_{g,prev}$. Based on these considerations, we define the amount of ejected gas as

$$\Delta M_{g,ej} = \Delta M_{g,cool} [f_{ej,sn}(1 - F_{sn}) + F_{sn}(1 - F_{agn})f_{ej,agn}], \quad (79)$$

where $f_{ej,sn}$ represents the fraction of SN-affected gas that is ejected, while $f_{ej,agn}$ represents the fraction of AGN-affected gas that is ejected. Using mass conservation, we can write the amount of the prevented gas as

$$\Delta M_{g,prev} = \Delta M_{g,cool} - \Delta M_{g,ej} - \Delta M_{g,sf}. \quad (80)$$

The total amount of gas residing outside the turbulent region is given by

$$\Delta M_{g,out} = \Delta M_{g,hot} + \Delta M_{g,ej}. \quad (81)$$

The total amount of gas remaining in the turbulent region is given by

$$\Delta M_g = (\Delta M_{g,sf} - \Delta M_* - \Delta M_{bh}) + \Delta M_{g,prev}. \quad (82)$$

And the total amount of non-star-forming gas is given by

$$\begin{aligned} \Delta M_{g,nonsf} &= \Delta M_{g,avail} - \Delta M_{g,sf} \\ &= \Delta M_{g,hot} + \Delta M_{g,ej} + \Delta M_{g,prev}. \end{aligned} \quad (83)$$

We note that, due to the limitation of our model in tracking details of the feedback on the gas, it remains uncertain whether gas can indeed cool and flow into the galaxy before being affected by feedback, or it is continuously coupled with the hot outflow and thus prevented from entering the galaxy. Consequently, the quantity $\Delta M_{g,ej}$ has to be treated as the hot gas component that is affected by the feedback in some way and eventually resides outside the galaxy, rather than the gas that enters the galaxy and is subsequently ejected. The fate of this gas component is not specified: it may be incorporated into the hot halo gas outside the SGC, as may be the case for high-mass halos, or be ejected from the host halo, as is the case for low-mass halos, or may remain in the halo as a part of the circum-galactic medium (CGM). Note also that $\Delta M_{g,ej}$ and $\Delta M_{g,prev}$ are completely degenerate, and the separation of the two is determined completely by the choices of $f_{ej,sn}$ and $f_{ej,agn}$ in equation (79). Additional modeling and constraints from observations of the gas component are needed to separate these different possibilities.

Using the equations given above, we can numerically integrate the different components until the end of the fast assembly phase. After that, we switch the modeling to the slow assembly regime, where a clumpy or a cold disk grows, depending on whether the galaxy is located in Q2 or Q3 of the quadrant diagram. In this paper, we ignore the difference between Q2 and Q3 and generally refer to the stars formed in the slow assembly phase as disk stars. As the growth of the SMBH is expected to be slow in a less turbulent medium, we freeze the mass of the SMBH at the end of the fast assembly phase. In practice, we assume that the transition to a rotation-supported system occurs when $f_{ej,sn} \approx f_{ej,agn} \approx (f_B - \lambda) / f_B \approx 3/4$. This choice is made so that the gas remains in SGC and available for star formation in the slow phase is above $f_B/4 \sim 0.04$, so that $f_\lambda > 1$. Our model for the star formation in the slow assembly phase is presented below.

4.5 Star formation in the slow assembly phase

For halos in the slow assembly phase, we use the empirical model of Lu et al. (2014) to model the stellar component. The model relates the star formation rate as a function of halo mass and redshift, using functional forms characterized by model parameters. Specifically, we

adopt the functional form and parameters of their Model-II, which was calibrated using observed galaxy stellar mass functions at $z \lesssim 4$. Particularly relevant to the scenario proposed here, Lu et al. (2014) found that the star formation model constrained solely by stellar mass functions is not able to reproduce the faint-end upturn seen in the local composite conditional luminosity function of galaxies in clusters. They empirically proposed a transition from an early phase of efficient star formation to a later phase of slow star formation to mimic the preventative feedback proposed in the literature (e.g. Mo & Mao 2002, 2004; Lu et al. 2015), and designed their Model-III to replace the behavior of Model-II at high redshift. Our two-phase model provides the physical base for the transition. In our implementation, we incorporate a log-normal random component with a standard deviation of $\sigma_{*,s}$ in the SFR predicted by their Model-II, to account for nuanced factors that are not fully captured by the halo mass alone, as described in Chen et al. (2021) using hydrodynamic simulations.

The SFR is integrated over time in the slow phase to predict the disk mass at each snapshot. The final stellar mass, denoted as M_* , during the slow assembly phase is the sum of the bulge mass, $M_{*,\text{bulge}}$, obtained at the last snapshot of the fast assembly phase, and the disk mass, $M_{*,\text{disk}}$, obtained in the slow assembly phase. It should be noted that our modeling does not explicitly incorporate galaxy-galaxy mergers. This is because the effects of mergers are implicitly captured in the fast assembly phase, and the merger rate is assumed to be low in the slow assembly phase.

Fig. 5 is a flow chart that summarizes different parts of our model. Most of the free parameters in our model have physically motivated ranges. However, some parameters are still uncertain and need to be calibrated using observations. Quantities that are not used in the calibration process can be considered as model predictions. In this paper, we adopt parameters for the slow assembly phase from Lu et al. (2014). We manually adjust the remaining parameters to match the $M_* - M_V$ relation obtained by Yang et al. (2012) at $z \approx 0.1$, and to match the $M_{\text{bh}} - M_{*,\text{bulge}}$ relation for elliptical galaxies obtained by Graham & Sahu (2023) at $z \approx 0$. The resulting model is referred to as the default model, and the corresponding parameter values are given in Table 1. In Appendix D, we present the strategy to calibrate the parameters, as well as the predictions from non-default models for references. With all these, we can follow the baryonic components in individual dark matter halos along their assembly histories. In the next section, we will implement these prescriptions in a set of simulated dark matter halos to predict statistical properties of the galaxy and SMBH populations, and to contrast our model predictions with with observational data.

5 APPLICATIONS TO SIMULATED HALOS

5.1 Halo samples

The primary samples we use are taken from a dark-matter-only simulation conducted as part of the Illustris-TNG project (Pillepich et al. 2018b; Nelson et al. 2019). To achieve a balance between statistical robustness and resolution in halo assembly histories, we use the TNG100-1-Dark run (hereafter TNGDark). Specifics of the simulation can be found in Appendix A.

To optimize computational efficiency in adjusting our model, we work with sub-samples of halos from TNGDark. Details of the sampling technique and the weighting strategy for computing summary statistics, which include both halo sampling rates and contributions from satellite subhalos, are given in Appendix A. In summary, we

define two halo samples at $z = 0$ with host halo masses (M_V , defined as M_{200c}) ranging from $10^{10} h^{-1} M_\odot$ to $10^{14.5} h^{-1} M_\odot$. The first sample, denoted as $S_{h,\text{small}}$ and referred to as the small sample, consists of 45 halos and is used solely to illustrate the evolution of individual galaxies. The second sample, denoted as $S_{h,\text{large}}$ and referred to as the large sample, includes 720 halos and is used for deriving summary statistics. The main branch assembly histories of these halos are extracted from merger trees and serve as the input for our model. Some examples of the assembly histories drawn from $S_{h,\text{small}}$ have already been shown in Fig. 1.

In cases where summary statistics depend on extremely small or massive halos, the simulated sample is insufficient. In such instances, we use analytically fitted halo mass functions to sample halos at any desired redshift, and analytically fitted halo assembly histories to sample the main branch assembly histories of the halos in the sample. We adopt the HMF library (Murray 2014) and the DIFFMAH library (Hearin et al. 2021) to implement halo mass functions and halo assembly histories, respectively. Further details about these Monte Carlo samples are given in Appendix A.

Throughout the application, we adopt a flat Λ CDM cosmology with parameters obtained from the Planck2015 results (Planck Collaboration et al. 2016), which is also adopted by TNGDark: the density parameters $\Omega_{M,0} = 0.3089$, $\Omega_{B,0} = 0.0486$, and $\Omega_{\Lambda,0} = 0.6911$, the Hubble constant $H_0 = 100 h \text{ km s}^{-1} \text{ Mpc}^{-1}$, with $h = 0.6774$, the Gaussian initial density field with a power spectrum $P(k) \propto k^n$ with $n = 0.9667$ and amplitude specified by $\sigma_8 = 0.8159$.

5.2 The growth of different mass components

Fig. 6 shows the time evolution of different mass components in three dark matter halos with present halo mass equal to $10^{12.0}$ (left panels), $10^{12.8}$ (middle) and $10^{14.2} h^{-1} M_\odot$ (right), respectively. These halos are taken from $S_{h,\text{small}}$, and the predictions are made using the High- z_f variant. The transition redshift, z_f , from the fast to slow assembly is marked by the vertical gray solid line for each halo. To demonstrate the uncertainty in the determination of z_f , we use a vertical gray dashed line to mark z_f based on the Low- z_f variant.

In the low-mass halo considered here, the bulge was formed at $z \sim 4$ and has a mass of about $10^{9.6} h^{-1} M_\odot$. The associated SMBH has a mass of $\sim 10^{6.1} h^{-1} M_\odot$, while the disk mass is about 20 times as large as that of the bulge. These numbers are quite similar to that of the Milky Way galaxy. For the most massive case, the total stellar mass is about $10^{11.2} h^{-1} M_\odot$ and completely dominated by the bulge that formed at $z \sim 3$. The associated SMBH mass is $10^{8.9} h^{-1} M_\odot$. Both these masses are about five times smaller than those of M87. The case of the intermediate mass is quite special in that its transition from the fast to the slow assembly is not well defined, as shown by the broad vertical band. Using the High- z_f definition of z_f , the predicted bulge mass is about $10^{10} h^{-1} M_\odot$, and the SMBH mass about $10^7 h^{-1} M_\odot$. The predicted disk mass is quite massive, about $10^{11} h^{-1} M_\odot$. However, if we extend the fast assembly phase to lower redshift, both the bulge and SMBH masses will be larger, and the disk mass smaller, as is demonstrated by the thin black and thin blue curves in the middle panel in the top row predicted using the Low- z_f variant. This clearly indicates that using a single value of z_f to separate the fast and slow assembly is not sufficient for some halos. As pointed out earlier, we will use both the High- z_f and Low- z_f variants to bracket the uncertainty.

As one can see, the gas is dominated by the non-star-forming component ($M_{g,\text{nonstf}}$, the red solid curve), which closely follows the halo mass (the purple solid curve). Most of the non-star-forming gas is generated by the SN and AGN feedback and presented either as

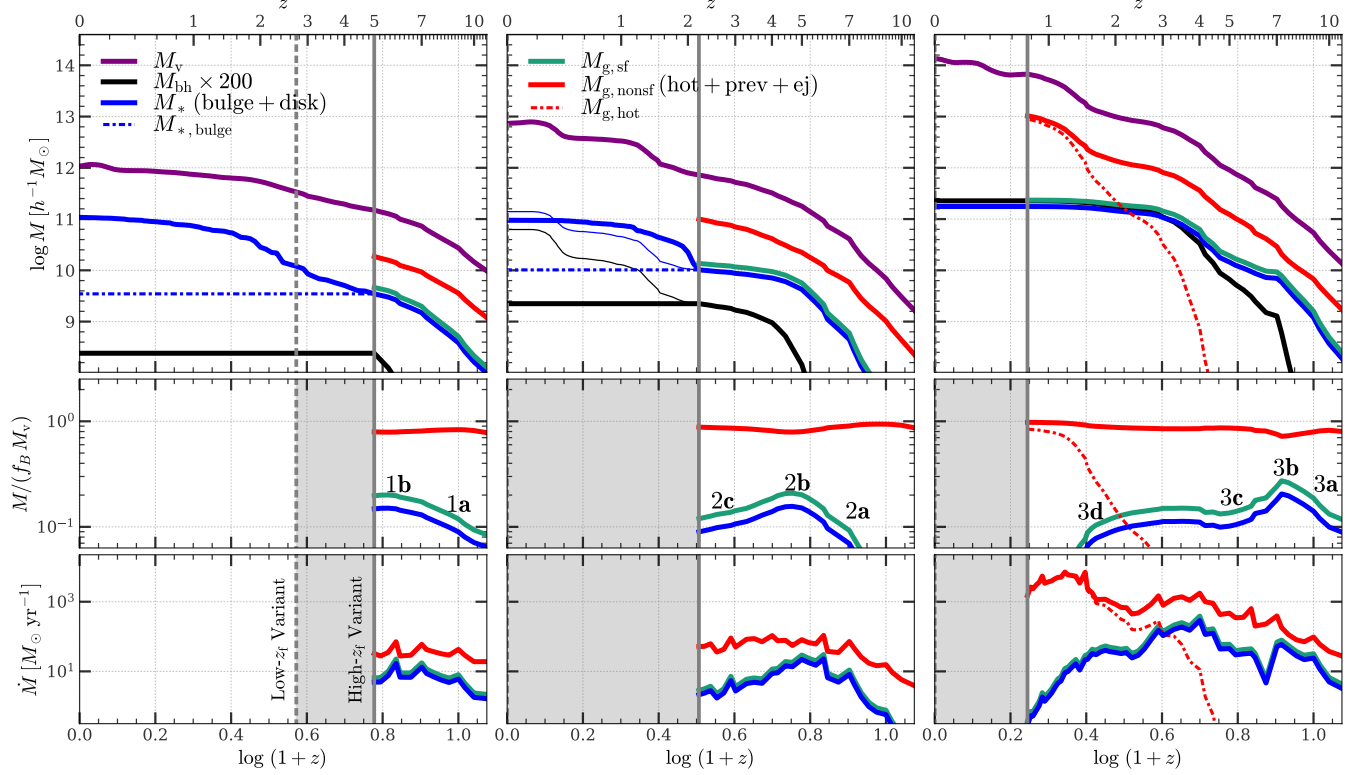


Figure 6. Assembly histories of different mass components for three individual halos and their central galaxies (**columns**) taken from the sample $S_{h,\text{small}}$ (see §5.1 for the definition of samples). **Top row** shows the masses of dark matter halo, central SMBH, stars and gas. **Middle row** shows the ratio of gas or stellar mass and $f_B M_V$ in the fast accretion regime. **Bottom row** shows the changing rate of gas or stellar mass. Masses of different components are shown by curves with different colors and line shapes, as indicated in the legends in the top row. Each dashed curve represents a sub-component of that shown by the solid curve with the same color. Specifically, **red solid curve** shows the mass of non-star-forming gas, which includes hot, prevented, and ejected gas, while **red dashed curve** shows the mass of hot gas, which is originated from inefficient radiative cooling. **Blue solid curve** shows the mass of all stars, while **blue dashed curve** shows the mass of bulge stars. **Vertical gray solid line** indicates the transition redshift, z_f , of the High- z_f variant, after which the halo enters the slow phase and disk stars begin to form. **Vertical gray dashed line** indicates z_f of the Low- z_f variant, and the **gray shaded area** marks the uncertainty in the determination of z_f bounding by the two variants. **Thick curves** are results obtained from the High- z_f variant, while the **black and blue thin curves** in the top-center panel are obtained from the Low- z_f variant. In the middle row, **annotations 1a, 2a and 3a** mark the SN-regulated regime, **1b, 2b and 3b** mark the switch point from SN-regulated to AGN-regulated regime, **2c and 3c** mark the AGN-regulated regime, and **3d** marks the regime where cooling is ineffective. Our model uses different prescriptions for each of these regimes. See §4.4 for the detailed evolutionary equations and Fig. 5 for a schematic summary. See §5.2 for a detailed discussion of this figure.

ejected gas ($M_{g,\text{ej}}$) or as prevented gas ($M_{g,\text{prev}}$). The exception is the high-mass halo (right column) near the end of the fast assembly, where the hot gas ($M_{g,\text{hot}}$, red dashed curve) contributes significantly to the non-star-forming gas. This is a direct consequence of the inefficient radiative cooling of the halo gas at $M_{\text{halo}} > 10^{13} h^{-1} M_\odot$.

By our model design, the stellar mass (blue curve) in the fast assembly phase follows that of star-forming gas, $M_{g,\text{sf}}$ (green curve). In the early growth of galaxies when $M_V \lesssim 10^{10} h^{-1} M_\odot$ (marked by 1a, 2a and 3a in the middle row for the three galaxies, respectively), the potential well of the halo is not deep enough to resist the SN feedback, thus the accumulation of star-forming gas is much slower than that of the non-star-forming gas, as seen from the middle and bottom rows. Consequently, the overall star formation efficiency during this period is suppressed at this stage (marked by 1a, 2a, 3a). When the halo mass continues to grow so that its potential is deepened, the SFR increases rapidly and reaches a peak value of ~ 10 – $100 M_\odot/\text{yr}$ at $M_V \sim 10^{11} h^{-1} M_\odot$ (marked by 1b, 2b and 3b). At this time, the stellar mass $M_* \sim 10^{9.5} h^{-1} M_\odot$, the specific star formation rate $\text{sSFR} \sim 10 h \text{Gyr}^{-1}$, and the star formation timescale is about

$1/\text{sSFR} \sim 0.1 h^{-1} \text{Gyr}$, comparable to the free-fall timescale of the halo, $t_{\text{ff}} \sim 0.1/H(z) \approx 0.1 h^{-1} \text{Gyr}$. This is a special ‘feedback-free’ regime where both SN feedback and AGN feedback are inefficient while radiative cooling is still effective. As seen from the middle row, the mass of the star-forming gas at this point reaches about 20%–30% of the cosmic baryon fraction in the halo, a value significantly higher than that in the low- z universe. The value could be even higher in halos where the on-set of SMBH growth was delayed by supernova (SN) feedback or some other factors operating near the center. It is thus possible that the high star formation efficiency required to explain recent JWST observations of massive galaxies at high- z (e.g. Naidu et al. 2022; Rodighiero et al. 2022; Donnan et al. 2022; Finkelstein et al. 2022; Bouwens et al. 2023; Finkelstein et al. 2023; Harikane et al. 2023; Labbé et al. 2023; Xiao et al. 2023; Lovell et al. 2022; Dekel et al. 2023; Mason et al. 2023; Yung et al. 2023; Boylan-Kolchin 2023; Chen et al. 2023b; Shen et al. 2023) is produced in this way. After the peak, the ratio $M_{g,\text{sf}}/(f_B M_V)$ declines rapidly, because of the onset of the SMBH growth (see the black lines in the top panels) and associated feedback. There is a delay in the onset of SMBH growth relative to that of the star formation, caused

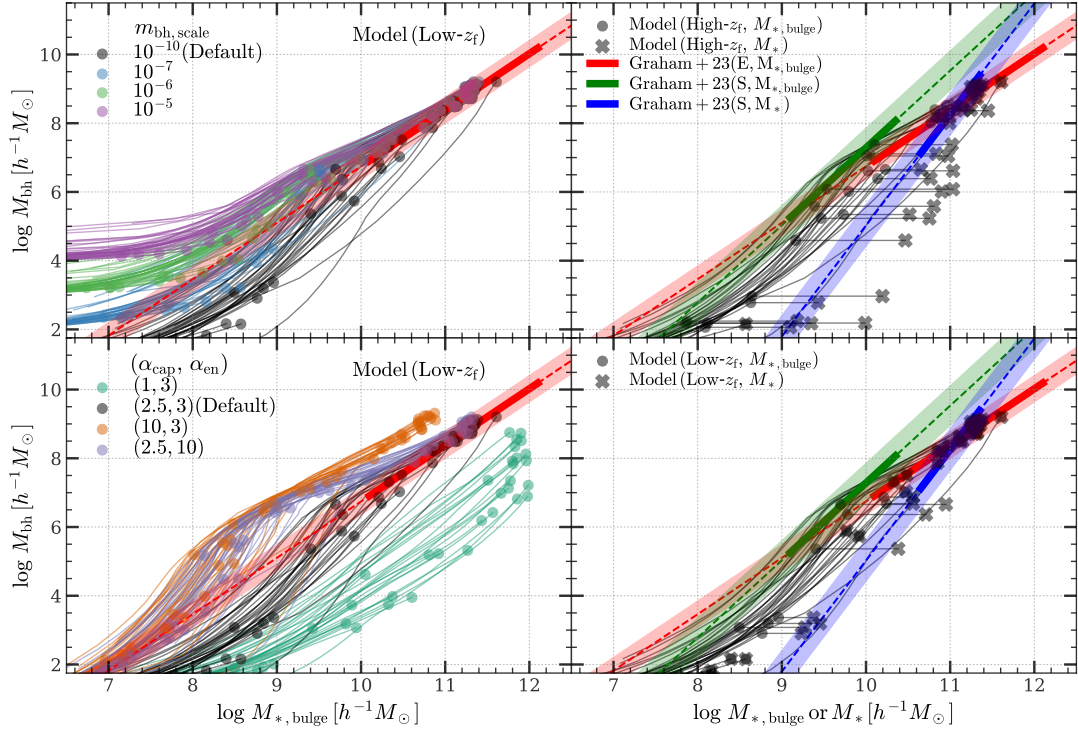


Figure 7. Evolutionary paths of individual galaxies in the black hole mass - stellar mass plane. **Upper-left panel:** Each bundle of curves with the same color show the $M_{\text{bh}} - M_{*,\text{bulge}}$ paths predicted by a specific model of given black hole seeding parameter $m_{\text{bh},\text{scale}}$, as indicated in the legend. Other parameters are set to their default values (see Table 1). Transition redshift (z_f) is defined by the Low- z_f variant. Only fast-phase evolution is shown here. The ending point of the fast phase is marked by a **circle** for each galaxy. **Lower-left panel:** Similar to the upper-left panel, but for the combination of black hole mass-capturing capability parameters α_{cap} , and α_{en} . **Upper-right panel** shows the evolution trajectories with additional disk growth in the slow phase, as indicated by a **horizontal line** with a **cross** marking the the ending point of the slow phase (i.e., $z = 0$) for each galaxy. Here z_f is defined by the High- z_f variant. **Lower-right panel** is similar to the upper-right panel, but z_f is defined by the Low- z_f variant. In all panels, **colored straight lines** are linear fits to observations obtained by [Graham & Sahu \(2023\)](#) at $z \approx 0$. Specifically, **red line** shows the $M_{\text{bh}} - M_{*,\text{bulge}}$ relation for elliptical (E) galaxies, while **green line** shows that for spiral (S) galaxies. **Blue line** shows the $M_{\text{bh}} - M_*$ (bulge + disk) relation for spiral galaxies. The solid piece of each line indicates the range reliably covered by observational data, the dashed line indicates the extrapolation, and shading area indicates the residuals of the linear fit. All halos in the sample $\mathcal{S}_{\text{h},\text{small}}$ are shown (see §5.1 for the details of samples). See §5.2 for a detailed discussion of our results. This figure illustrates how the SMBHs in our model converge to the observed scaling relations for different types of galaxies and different stellar mass components.

by the period required to grow a SMBH from a low seeding mass assumed in our model. The ratio $M_{\text{g},\text{sf}}/(f_{\text{B}}M_{\text{V}})$ then settles down to a roughly constant value at about 0.15 (marked by 2c and 3c; 1c does not exist). For the massive case, $M_{\text{g},\text{sf}}/(f_{\text{B}}M_{\text{V}})$ can decline further at some point (marked 3d) when the gas can no longer cool.

Let us examine the growth of SMBH in more detail. Fig. 7 shows the evolutionary paths of individual systems in the SMBH mass-stellar mass plane. The upper-left panel shows the impact of varying the seeding mass, as represented by the value of $m_{\text{bh},\text{scale}}$, while keeping all other model parameters at their default values (see Table 1) and using z_f given by High z_f . As one can see, all evolutionary trajectories converge to the same fiducial relation represented by the red lane obtained by [Graham & Sahu \(2023\)](#) from low- z data, independent of the seeding mass. However, depending on the initial seeding mass, it will take some time for a SMBH to reach the fiducial relation. Thus, at any given time, particularly at an early time, some SMBH can deviate significantly from the fiducial relation, especially in the low-mass end. The convergent behavior of the SMBH growth shown here is fully consistent with the indication obtained by [Zhuang & Ho \(2023\)](#), who used the stellar and SMBH masses and growth rates to infer the evolutionary trajectories of individual SMBHs and their host galaxies.

In the lower-left panel, we show the impact of changing the values

of α_{cap} , which specifies the ability of a SMBH to capture mass in the SGC, and α_{en} , which describes the enhancement of the capture ability produced by the SN feedback in low-mass halos. Our default model assumes $\alpha_{\text{cap}} = 2.5$ and $\alpha_{\text{en}} = 3.0$. In this model, the SMBH mass increases rapidly with time when the bulge mass reaches $\sim 10^9 h^{-1} M_{\odot}$, and merges from below to the red lane (the fiducial relation) at a bulge mass of $\approx 10^{10.5} h^{-1} M_{\odot}$. The green bundle (assuming $\alpha_{\text{cap}} = 1$) and orange bundle (assuming $\alpha_{\text{cap}} = 10$) of lines in the lower-left panel show the effects of changing α_{cap} . As can be seen, a higher value of α_{cap} leads to faster growth of SMBH at high- z (corresponding to the lower end of the bulge mass). However, due to regulations by the AGN feedback, the evolutionary trajectories join a lane that is parallel to the red lane but has a higher amplitude. In contrast, a value as low as $\alpha_{\text{cap}} = 1$ results in an inefficient growth at all redshifts, eventually giving a $M_{\text{bh}} - M_{*,\text{bulge}}$ relation that is about 1dex lower than the red lane. In this case, the evolutionary trajectories do not seem to merge, as they have not yet reached the point where regulations by the AGN feedback are important. Thus, while the logarithmic slope of the $M_{\text{bh}} - M_{*,\text{bulge}}$ relation is produced by the AGN feedback, the fiducial value of $\alpha_{\text{cap}} \approx 2.5$ is actually required by the observed amplitude of the relation. Increasing the value of α_{en} (purple bundle) makes black holes grow faster in their early stage, which is similar to the effect of increasing α_{cap} (orange

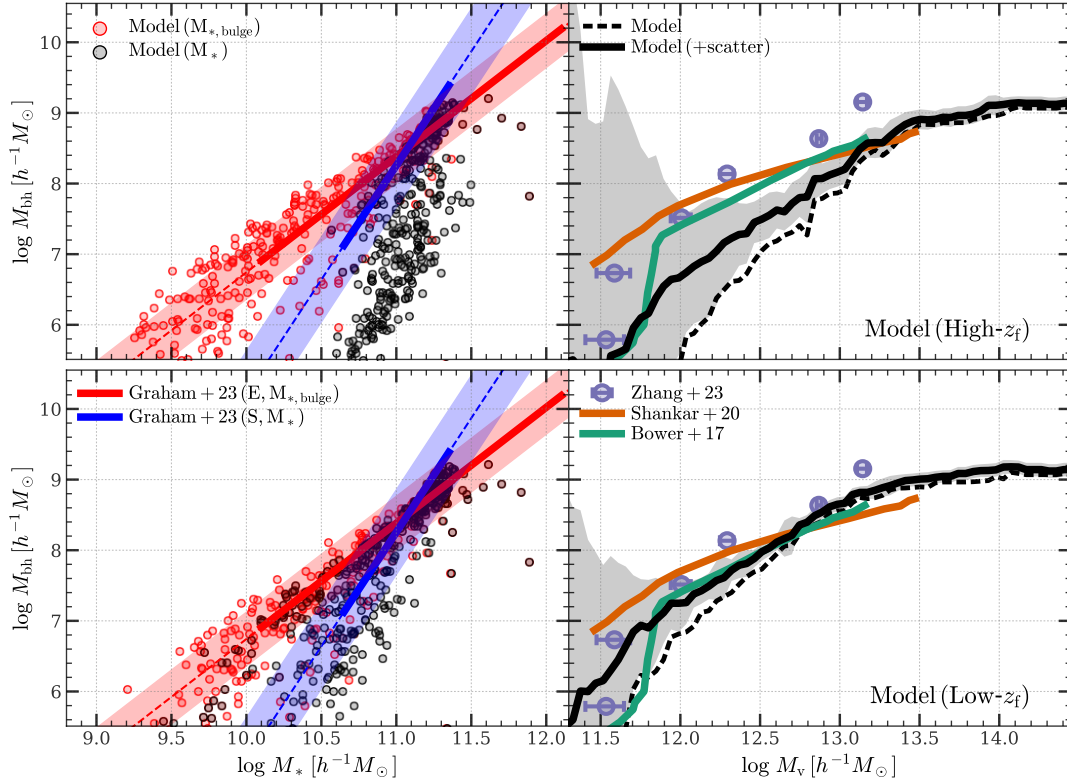


Figure 8. SMBH mass to stellar mass (**left column**) and halo virial mass (**right column**) relations at $z \approx 0$. The **upper row** shows the predictions of the High- z_f variant, while the **lower row** shows those of the Low- z_f variant. The default model parameters are adopted in all panels (see Table 1). In the left column, the **red circles** show the predicted M_{bh} with $M_{*,\text{bulge}}$ of individual galaxies, while the **black circles** show the predicted M_{bh} with M_* (bulge + disk). In the right column, the **dashed black line** represents the ‘true’ relation predicted by the model, while the **solid black line** incorporates the model prediction with an up-scatter of $\sigma = 3 \times 10^7 h^{-1} M_\odot$ in linear scale and an up-scatter of $\sigma = 0.5$ dex in logarithmic scale to mimic the observational systematics near the sharp transition at $M_v \approx 10^{11.5} h^{-1} M_\odot$. For comparison, we show the observational and empirical results from [Shankar et al. \(2020\)](#), [Zhang et al. \(2023a\)](#) and [Graham & Sahu \(2023\)](#), and the analytical modeling result from [Bower et al. \(2017\)](#). See §5.3 for a detailed discussion of our results. This figure demonstrates that our model is able to reproduce the local scaling relations of SMBHs, galaxies and halos.

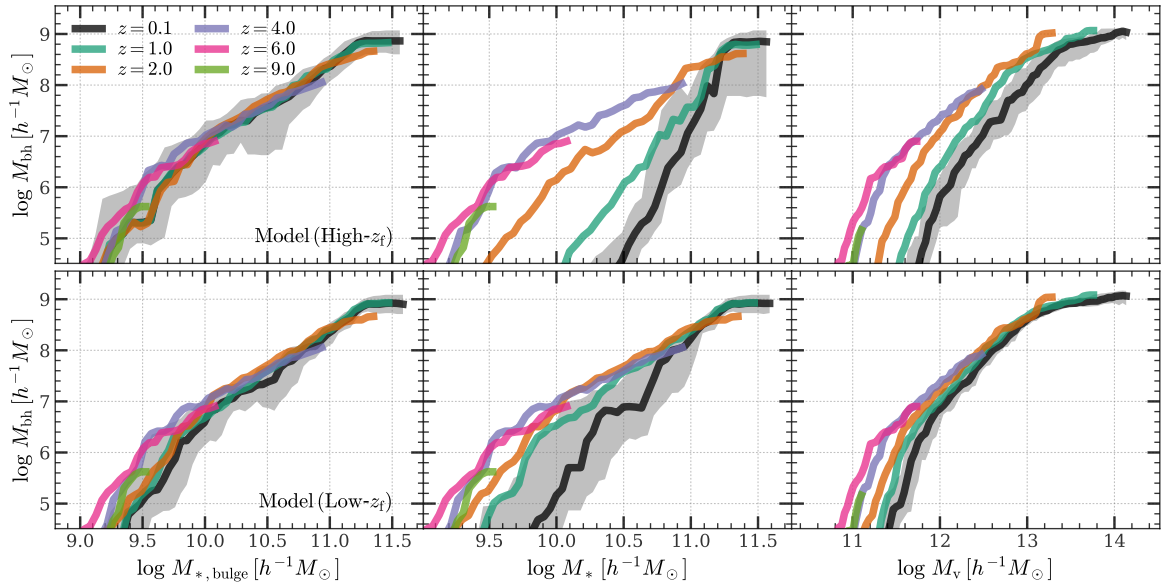


Figure 9. Model prediction for the median relations between SMBH mass and bulge mass ($M_{*,\text{bulge}}$, **left column**), total stellar mass (M_* , including bulge + disk, **middle column**), and halo virial mass ($M_v \equiv M_{200c}$, **right column**) at various redshifts ranging from $z = 0.1$ to $z = 9$, as indicated in the legend. **Two rows** show the predictions obtained from the High- z_f variant and Low- z_f variant, respectively, both with default model parameters (see Table 1). **Shaded areas** surrounding the black curves represent the $1-\sigma$ (16% - 84%) quantiles. See §5.3 for a detailed discussion of this figure.

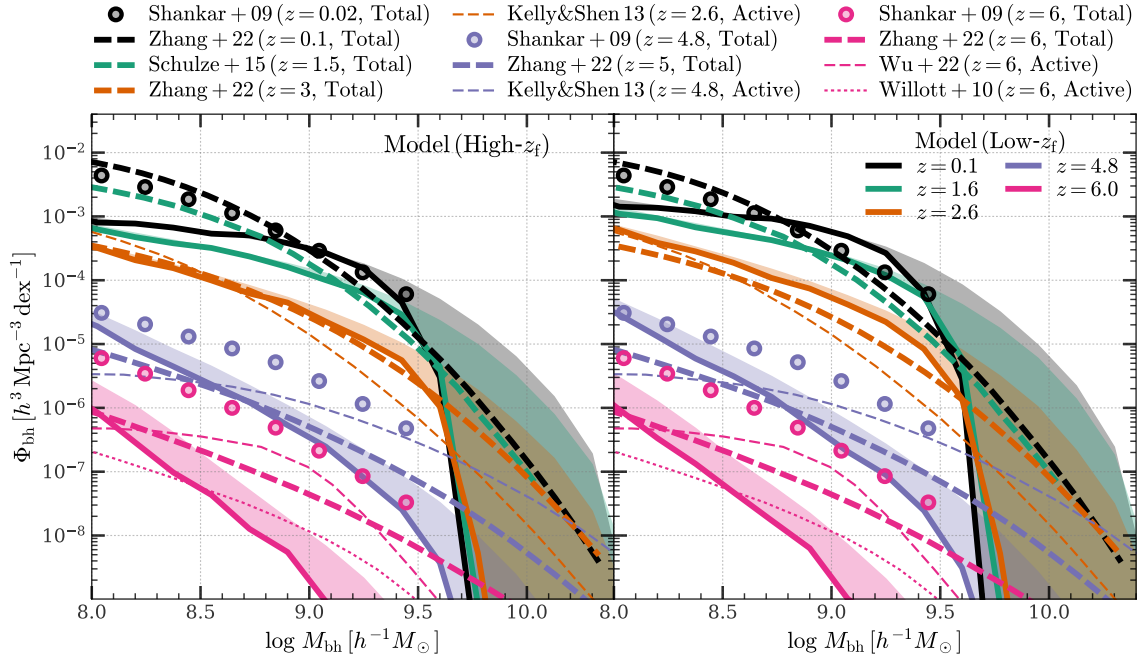


Figure 10. SMBH mass functions, $\Phi_{\text{bh}} \equiv d^2 N_{\text{bh}} / [d \log M_{\text{bh}} dV]$, at $z \approx 0 - 6$. The **thick solid curves** represent the prediction of our model with default parameters (see Table 1). The **left and right panels** show the results from the High- z_f and Low- z_f variants, respectively. The **shaded region** surrounding each curve indicates the variation of Φ_{bh} when a log-normal random scatter with $\sigma = 0.3$ dex is introduced into M_{bh} to account for the substantial Eddington bias at the high-mass end. Results obtained at comparable redshifts are shown by the same color. The total SMBH mass functions (corrections were made for the AGN duty cycle) are shown by **thicker symbols** (thick solid and dashed curves, as well as circle markers), while active SMBH mass functions (including only active AGN) are represented by **thinner symbols** (thin dashed and dotted curves). The presented observational results include those from Shankar et al. (2009), Willott et al. (2010), Kelly & Shen (2013), Schulze et al. (2015), Wu et al. (2022) and Zhang et al. (2022a). See §5.3 for a detailed discussion of our results. This figure indicates that our model reproduces the observational trend of SMBH mass function at a wide range of redshift.

bundle). However, at a later time when the enhancement becomes inefficient, the evolutionary trajectories join the red lane, but with a delay in comparison to the default model. The value of α_{en} may thus be constrained if the slope of the $M_{\text{bh}} - M_{*,\text{bulge}}$ relation becomes steeper when the bulge mass is lower than some characteristic value. For $\alpha_{\text{en}} = 3$, this characteristic mass is about $10^{10} h^{-1} M_{\odot}$, which seems to be needed by observational data, as we will see below.

In the upper-right panel, the green line shows the observational results for bulges of spiral (S) galaxies. This line has a logarithmic slope of ~ 2.25 , significantly steeper than that for early-type (E) galaxies. Our model provides an explanation of this steepening, by assuming that bulges in spiral galaxies had not reached the stage of AGN regulation before they entered the slow assembly phase.

The blue line in the upper-right panel shows the observed relation between the SMBH mass and the total stellar mass relation for spiral galaxies. This line has a slope of about 3.23, much steeper than the red line. This steepening is expected in our model, where M_{bh} remains constant in the slow assembly phase while the stellar mass increases due to star formation in the disk. This produces a horizontal shift, as indicated by the crosses connected to the bulge mass (filled circles) by horizontal lines. Since lower-mass halos on average move to the slow assembly phase earlier and their star formation efficiency in the slow phase is higher, they can grow larger disks (relative to the bulge component) than higher-mass halos. This leads to a larger horizontal shift for lower-mass systems and gives rise to the observed steepening of the relation. The High- z_f variant seems to over-predict the shift, resulting in a relation that is too steep, while the predictions of Low- z_f , shown in the lower-right panel, work much better.

5.3 The supermassive black hole population

We apply our model to the halo sample $S_{\text{h,large}}$ to generate galaxies and SMBHs to investigate their statistical properties. Fig. 8 shows the correlation of the SMBH mass with the stellar mass of galaxies (left column) and with the halo mass (right column). Results using default parameters (see Table 1) are shown for the High- z_f variant (upper row) and Low- z_f variant (lower row), respectively. The correlation with the stellar mass is shown separately for the bulge stellar mass $M_{*,\text{bulge}}$ (red circles) and the total stellar mass M_* (black circles). As one can see, our model predictions for the $M_{\text{bh}} - M_{*,\text{bulge}}$ relation match well the observational data, shown by the red line and band, in both slope and amplitude. The predicted scatter increases in the low-mass end, because many systems have not yet reached the stage of AGN regulation where $M_* > 10^{10.5}$. The two variants of z_f yield very different $M_{\text{bh}} - M_*$ relations, with High- z_f predicting a much larger disk mass for disk-dominated galaxies and thus a much steeper $M_{\text{bh}} - M_*$ relation than Low- z_f . As discussed before, the fast assembly phases of some halos end much earlier in High- z_f than in Low- z_f (see §5.2 and Fig. 6), giving much longer time for the disk to grow in these halos. The Low- z_f variant appears able to match the observational data nicely, indicating that the growth of the bulge and SMBH components can continue at $z < z_f$ defined by High- z_f . When a moderate random scatter is included in M_{bh} to mimic observational uncertainties, the $M_{\text{bh}} - M_V$ relation predicted by the Low- z_f variant also matches observational results well, while High- z_f seems to under-predict M_{bh} for given M_V in low-mass halos (see left panels of Fig. 8). The difference again has its origin in the fact

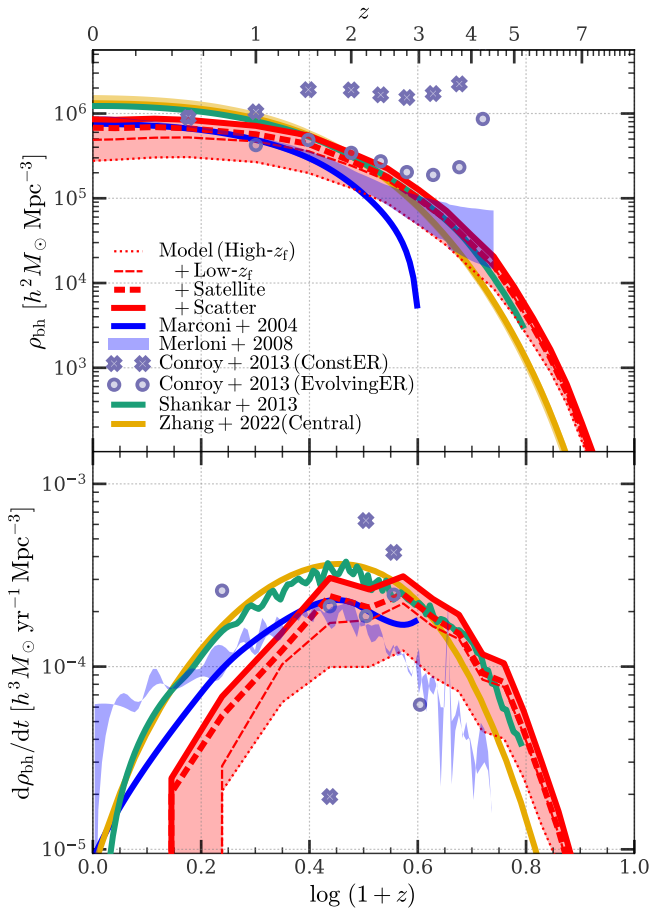


Figure 11. Evolution of the cosmic black hole mass density (ρ_{bh} , **top panel**) and the black hole mass growth rate density ($d\rho_{\text{bh}}/dt$, **bottom panel**). The predictions of the model with default parameters (see Table 1) are represented by the **red curves** bounding a **shaded area**. The **red dotted curve** shows the case where the transition redshift, z_f , is defined by the High- z_f variant, considering only central galaxies and without incorporating any observational uncertainty. The **red thin dashed curve** represents the result of the High- z_f variant, with a further inclusion of satellites resulting in the **red thick dashed curve**. The additional incorporation of a log-normal scatter to M_{bh} with $\sigma = 0.3$ dex is shown by the **red solid curve**. A number of empirical results calibrated by observations are included, such as those from [Marconi et al. \(2004\)](#), [Merloni & Heinz \(2008\)](#), [Conroy & White \(2013\)](#), [Shankar et al. \(2013\)](#) and [Zhang et al. \(2022a\)](#). For the study by [Conroy & White \(2013\)](#), the results obtained by a model with constant and redshift-dependent Eddington ratio distributions are indicated by **cross** and **circle markers**, respectively.

that the time for growing the bulge and SMBH components is shorter in High- z_f than in Low- z_f for some halos.

A recent spectroscopic study of [Maiolino et al. \(2023\)](#) based on JWST/JADES survey reported a number of over-massive black holes at $z > 4$. At $M_* \lesssim 10^9 M_\odot$, the estimated SMBH masses are orders of magnitude higher than the extrapolation of the local scaling relation shown in Fig. 8. This discrepancy could be caused by two main factors. Firstly, since the local scaling relation is not well constrained at $M_* \lesssim 10^9 M_\odot$, the extrapolation may not be reliable. As our fiducial model of SMBH seeding is based on the local scaling relation, it would under-predict SMBH masses at high z . Indeed, the change in SMBH seeds has significant impacts on the mass evolution of SMBHs in our model, as shown in Fig. 7. Secondly, observational estimates of the SMBH mass at high z are still quite uncertain. The

mass estimator used by [Maiolino et al. \(2023\)](#) relies on assumptions of virialization, a redshift-independent geometry of broad-line regions and the extrapolation of locally calibrated scaling relations. As shown by the case study of [Abuter et al. \(2024\)](#), a break of these assumptions can lead to large systematic changes in the estimated SMBH mass. Given the uncertainties both in current observations and in our model, we do not make a detailed comparison of our model with the observational data.

Fig. 9 shows the correlation of M_{bh} with bulge mass (left), total stellar mass (middle) and halo mass (right) at different redshift. The predicted $M_{\text{bh}}-M_{*,\text{bulge}}$ relations by both High- z_f and Low- z_f are quite independent of redshift, except at the low-mass end where the amplitude of the relation appears higher at higher z . This redshift-independence of the $M_{\text{bh}}-M_{*,\text{bulge}}$ relation is actually seen in observational data (e.g. [Schulze & Wisotzki 2014](#); [Zhuang & Ho 2023](#)). The middle-column panels show that the predicted $M_{\text{bh}}-M_*$ relation depends significantly on redshift, becoming progressively steeper at lower z , and the predicted evolution is stronger in the High- z_f variant than in Low- z_f . This steepening is completely produced by the growth of the disk mass with time after the formation of the bulge and SMBH in the fast assembly phase. Finally, the predicted $M_{\text{bh}}-M_V$ relation also steepens with redshift, but the change is much weaker for Low- z_f than for High- z_f . In a recent paper by [Shimasaku & Izumi \(2019\)](#), a weak redshift-dependence was found in the observed SMBH mass versus halo mass relation, again favoring a more extended growth of M_{BH} than that assumed in High- z_f .

In Fig. 10 we show our model predictions for the SMBH mass functions at different redshift, plotted as solid curves of different colors. Data for comparisons are also shown using symbols and broken lines with similar color coding. As one can see, model predictions of High- z_f and Low- z_f are similar, except at low z where the mass function at the low-mass end predicted by High- z_f is significantly lower. Our model predictions follow the general trend in the observational data, except at high- z where the predicted mass function appears significantly steeper than the observational results. Unfortunately, the data are still very uncertain; there are large discrepancies between different observational results. This is clearly seen from the change in the high-mass end of the predicted SMBH mass function caused by introducing a moderate amount of scatter, $\sigma = 0.3$ dex, in the predicted M_{bh} to mimic the Eddington bias. A horizontal shift of ≈ 1 dex is produced at $\Phi_{\text{bh}} = 10^{-8} h^3 \text{Mpc}^{-3} \text{dex}^{-1}$ in the low- z mass function, making it difficult to draw any strong conclusions (see [Conroy & White \(2013\)](#) for a similar result). A more robust quantity is the SMBH mass density, ρ_{bh} , which is obtained by integrating the mass-weighted mass function. This density as a function of redshift is shown in the upper panel of Fig. 11 for different cases, in comparison with various empirical results calibrated with observational data ([Marconi et al. 2004](#); [Merloni & Heinz 2008](#); [Conroy & White 2013](#); [Shankar et al. 2013](#); [Zhang et al. 2022a](#)). Note that these empirical results are obtained by different sets of assumptions that are not necessarily consistent with each other. For example, the starting redshift for black hole growth is assumed to be ≈ 3 by [Marconi et al. \(2004\), \$\approx 6\$ by \[Shankar et al. \\(2013\\)\]\(#\), and \$\gtrsim 15\$ by \[Zhang et al. \\(2022a\\)\]\(#\). As seen from the figure, these assumptions give different evolution trajectories at high redshift. Another source of systematic arises from the degeneracy of model parameters, e.g. between the mean relation and assumed variances, which can be seen from the two divergent curves obtained by \[Conroy & White \\(2013\\)\]\(#\) \(crosses and circles\). However, as shown in the lower panel of Fig. 11, our model appears to under-predict the growth rate of SMBH mass at \$z < 1\$. Although the fraction of the SMBH mass density generated at \$z < 1\$ may be small, the discrepancy indicates that our current model](#)

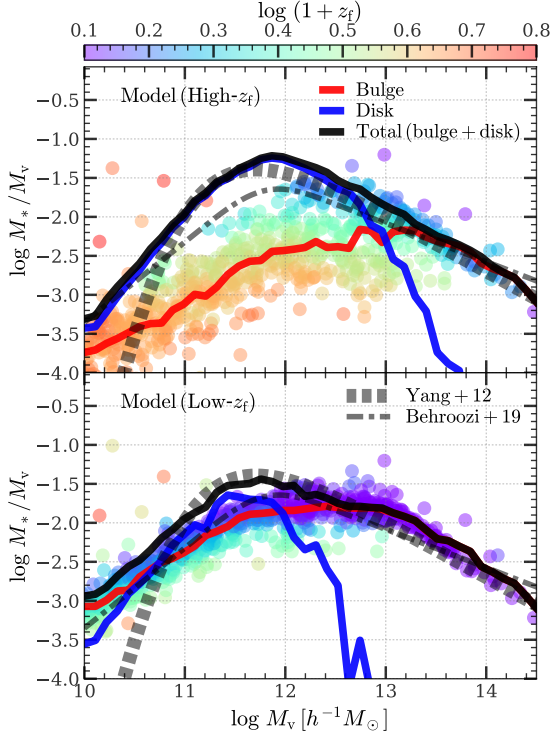


Figure 12. Stellar mass to halo mass ratio as a function of halo mass ($M_V \equiv M_{200c}$) at $z \approx 0.1$. The default model parameters (see Table 1) are adopted, and the halo sample $S_{h,\text{large}}$ (see §5.1) is used to derive the statistics. The **upper and lower panels** show the High- z_f variant and the Low- z_f variant, respectively. In each panel, model predictions for bulge, disk, and total (bulge + disk) stellar mass are shown by **red, blue, and black curves**, respectively. **Scatter points** represent the results for the bulge mass of individual galaxies, color-coded by their transition redshift, z_f , according to the color bar. The **gray thick dashed curve** represents the total stellar mass - halo mass relation obtained by [Yang et al. \(2012\)](#) with conditional stellar mass function modeling. The **gray thin dashed curve** represents the total stellar mass - peak halo mass relation obtained by [Behroozi et al. \(2019\)](#) with abundance-based empirical modeling. For further discussion, see §5.4. This figure highlights that older halos (with early transition) have centrals with lower bulge mass and larger disk mass, which is crucial for reproducing the observed bimodal distribution of galaxies shown in Fig. 13.

may miss some channels of SMBH mass growth at low z . Indeed, as discussed in §4, our model only includes SMBH growth in Q1 of the quadrant diagram. In reality, later mergers of cold gaseous disks, corresponding to low-mass halos making an excursion from Q3 to Q4, may feed SMBH with cold gas and increase their masses. In addition, gas-rich disks living near the border of Q2 and Q3, may become unstable due to non-axisymmetric perturbations from their halos and/or other objects, forming bar-like structures that can also feed the central SMBH. It seems clear that these channels need to be included in order to explain the SMBH mass growth at $z < 1$.

5.4 Stellar components

Fig. 12 shows the stellar mass versus halo mass relation at $z \sim 0$, predicted by both the High- z_f (upper panel) and Low- z_f (lower panels) variants. Here default model parameters are adopted (see Table 1) and sample $S_{h,\text{large}}$ (see §5.1) is used to derive the statistics. Results are shown for the total stellar mass (M_* , solid black curve), and separately for the bulge mass ($M_{*,\text{bulge}}$, red curve) and disk mass

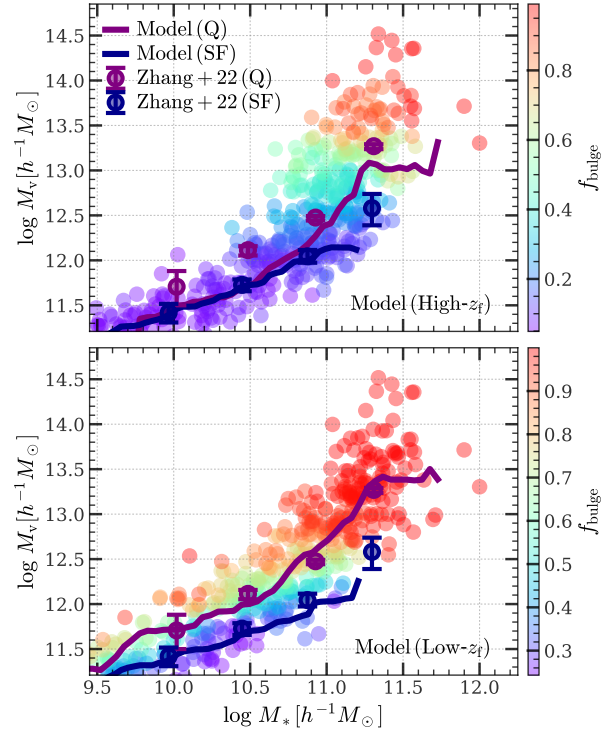


Figure 13. Similar to Fig. 12, but here we show the $M_V - M_*$ relation at $z \approx 0.1$ for direct comparison with observational data. Individual galaxies, represented by **scatter points**, are color-coded based on their bulge fraction, $f_{\text{bulge}} \equiv M_{*,\text{bulge}}/M_*$, as indicated by the color bar. Galaxy-galaxy lensing measurements of halo mass obtained by [Zhang et al. \(2022b\)](#) for quenched and star-forming galaxies are shown by **purple and blue markers**, respectively. Our predictions for these two types of galaxies are shown by **solid curves**. To mimic observational uncertainties, a log-normal random scatter with $\sigma = 0.15$ dex is added to both M_* and M_V . This figure suggests that our model can naturally reproduce the observed bimodal distribution of galaxies. For further discussion, see §5.4.

($M_{*,\text{disk}}$, blue curve). The data points are individual model galaxies, color-coded here according to z_f . For comparison, we include the observational results of [Yang et al. \(2012\)](#), obtained from fitting galaxy stellar mass functions and conditional stellar mass functions of group galaxies. As one can see, for $M_V > 10^{11} h^{-1} M_\odot$ both High- z_f and Low- z_f variants predict a similar $M_* - M_V$ relation that closely matches the observational relation. For lower M_V , the predicted M_* is higher than that of [Yang et al. \(2012\)](#). However, the relation for such low-mass halos is still poorly constrained observationally. For example, empirical results obtained from other combinations of observational data show that the stellar mass in low-mass halos could be much higher, as shown by the thin dashed curve obtained more recently by [Behroozi et al. \(2019\)](#).

In contrast, the $M_{*,\text{bulge}} - M_V$ relation at $M_V < 10^{13} h^{-1} M_\odot$ predicted by Low- z_f is about a factor of three as high as that predicted by High- z_f . This difference is produced by the longer time in Low- z_f for halos to stay in the fast assembly phase, where stars are assumed to reside in the bulge component. The fact that both Low- z_f and High- z_f predict very similar $M_* - M_V$ relations thus indicate that our star formation model matches the empirical model of [Lu et al. \(2014\)](#). In their Model-III, a significant fraction of stars in present-day low-mass halos are assumed to have formed at redshift above a critical value $z \sim 2$, and thus it requires a low star formation rate at lower z to make up the total stellar mass. Such a low rate, combined

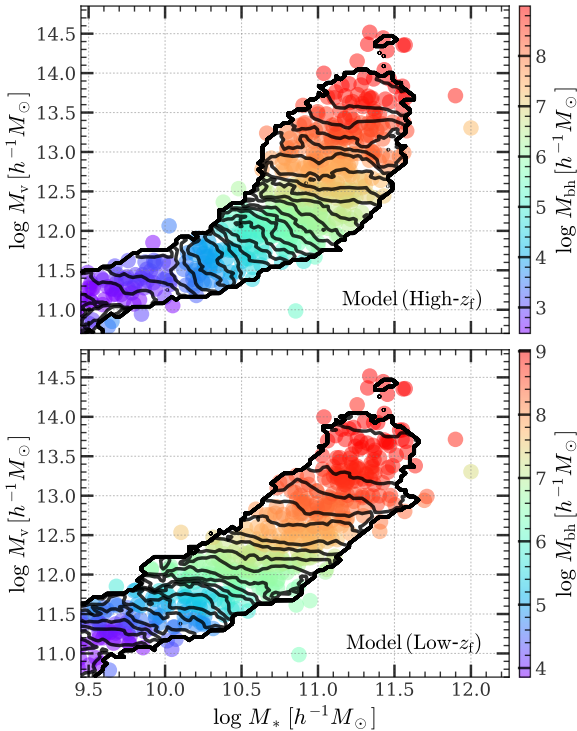


Figure 14. Similar to Fig. 13, but here scatter points are color-coded by SMBH mass M_{bh} . Contours with equal SMBH mass are overplotted. This figure indicates that the strong dependency of M_{bh} with M_V in high-mass halos is reproduced if the SMBH growth in high-mass halos is regulated by the AGN feedback controlled by gravitational potential. See §5.4 for a detailed discussion.

with the shorter time available for disk star formation in the case of Low- z_f , produces only small amounts of disk mass in low-mass halos. There is now evidence that present-day low-mass galaxies may contain large amounts of old stars (e.g. Zhou et al. 2020; Sacchi et al. 2021; Meng et al. 2023; Weisz et al. 2023). Whether these stars formed in dynamically hot ‘bulges’ or in dynamically cold ‘disks’ is still unclear. The answer to this question is observationally challenging because it is difficult to distinguish random motion from rotation in a low-mass halo where the circular velocity is low.

From the color coding of z_f for individual galaxies shown in Fig. 12, one can see that, for a given M_V , older halos (those with higher z_f) have centrals with lower bulge mass and larger disk mass. This is an interesting prediction of the model, and may shed some light on the connection between halos and galaxies beyond abundance matching based on masses alone. To demonstrate this, we show in Fig. 13 the relation of M_V with M_* , separately for star-forming and quenched galaxies. Observations suggest that quenching is tightly related to dynamical hotness (e.g. Bluck et al. 2020, 2022; Hong et al. 2023). Here we use the bulge fraction, $f_{\text{bulge}} \equiv M_{*,\text{bulge}}/M_*$, as a proxy of dynamical hotness, to separate quenched galaxies from star-forming ones by a stellar-mass-dependent boundary, $f_{\text{bulge}}(M_*)$, chosen to match the observed quenched fraction as a function of stellar mass obtained by Bauer et al. (2013). Fig. 13 shows a clear separation in the $M_V - M_*$ relation between the two types of galaxies, particularly in the Low- z_f variant. At a given M_* , the halo mass is on average larger for galaxies with higher f_{bulge} (thus more quenched). Equivalently, for a given M_V , the total stellar mass M_* is on average higher for galaxies of lower f_{bulge} (thus more star-forming). This

prediction can be tested by measuring the halo mass for galaxies of the same stellar mass but with different morphology and different star-formation status. Galaxy-galaxy lensing results of Mandelbaum et al. (2016) and Zhang et al. (2022b) show that star-forming galaxies (presumably dominated by the disk component) have lower halo mass for their stellar mass in comparison to quenched galaxies (dominated by bulges). These observational results are qualitatively reproduced by our model, particularly by the Low- z_f variant, as shown by the curves in the figure. We also note that the predicted $M_V - M_*$ relation has large scatter at the high-mass end, produced by the more diversity in their assembly histories. This may have important implications for models based on abundance matching.

The predicted anti-correlation between star formation rate and z_f is somewhat counter-intuitive, as one would assume that older halos should preferentially host older-type galaxies. This anti-correlation is produced naturally in our model by the longer time for disk formation in halos of higher z_f , provided the AGN feedback does not preferentially suppress star formation in old halos. Our model thus provides a boundary condition to model the observed anti-correlation, e.g. using cosmological hydrodynamic simulations. For example, the SIMBA simulation (Davé et al. 2019) reproduces the anti-correlation (Cui et al. 2021), as it satisfies the condition. In SIMBA, earlier-formed (older) halos host galaxies with later transitions to the slow growth of the SMBH. This has the effect of delaying the onset of the ‘jet’ mode feedback in older halos, thus giving longer time for star formation in dynamically cold disks. However, this anti-correlation is not seen in other cosmological simulations that implement different feedback models. For example, the trigger of the kinetic mode of AGN feedback in the TNG simulation (e.g. Weinberger et al. 2018) was tuned to depend on the mass of SMBH, so that the observed anti-correlation between halo formation time and star formation rate is suppressed. On the other hand, the EAGLE simulation has only one feedback channel throughout the entire halo assembly history Schaye et al. (2015), thus mixing the growth paths of galaxies in halos of different formation times. As cosmological simulations have not yet reached a consensus on how to model the AGN feedback, it is difficult to draw a firm conclusion as to exactly which mechanisms can produce the observed anti-correlation.

Fig. 14 shows the $M_V - M_*$ relation color-coded according to the value of M_{bh} . As expected, M_{bh} increases with both M_* and M_V . However, inspecting the figure in detail reveals that M_{bh} is more closely related to M_V than to M_* in the high-mass end, as shown by the nearly horizontal contours of constant M_{bh} at $M_V > 10^{12} h^{-1} M_\odot$. At lower mass, $M_* < 10^{10.5} h^{-1} M_\odot$, the contours are nearly vertical, indicating that M_{bh} is more closely related to stellar mass than to halo mass. These results are produced because the growth of the SMBH in high-mass halos is regulated by the AGN feedback efficiency controlled by M_V (or V_{max}). Our test shows that, if the AGN feedback is turned off, by setting $\alpha_{\text{agn}} = 0$, the dominating dependence on M_V at the high-mass end disappears. When the regulation by AGN feedback is insignificant, the growths of both M_{bh} and M_* are driven by the gas mass available for them, and the correlation of M_{bh} with M_* becomes more dominating. This is seen at the low-mass end in the prediction of the High- z_f variant but almost absent in that of Low- z_f . Using gravitational lensing measurements of halo mass, Zhang et al. (2023a) found that the SMBH mass depends strongly on M_V at $M_{\text{bh}} > 10^7 h^{-1} M_\odot$, while the dependence becomes much weaker at lower M_{bh} . This is qualitatively in agreement with the prediction of the High- z_f variant. The discrepancy of the data with the Low- z_f variant may indicate that the growth of M_{bh} predicted by Low- z_f , which is missing in High- z_f but seems to be needed to better match other observations, is not able to affect the gas effectively

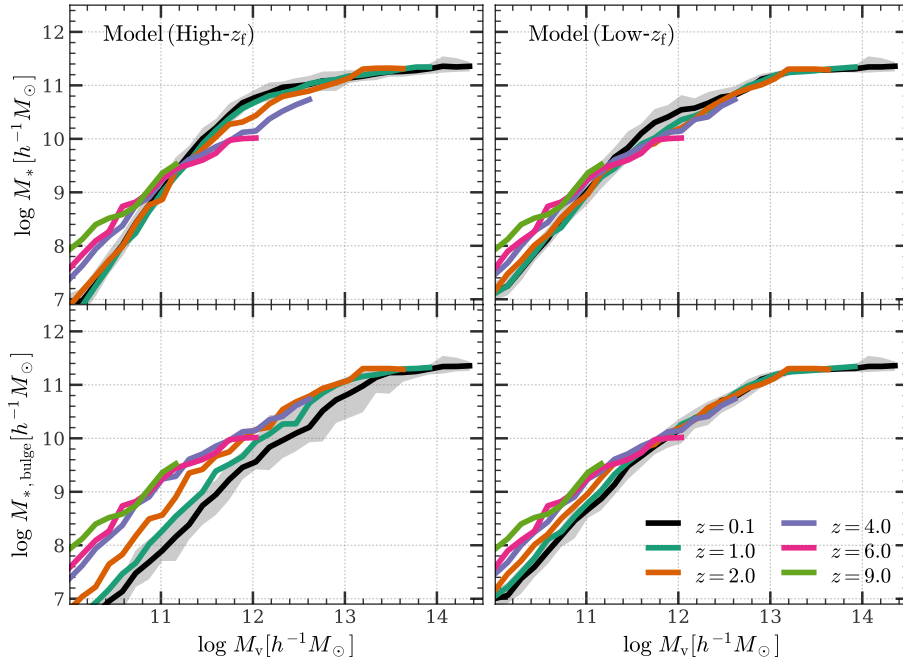


Figure 15. The stellar mass to halo mass relation predicted by our model at various redshifts (different colors) from $z = 0.1$ to $z = 9$, as indicated in the legend. The **upper row** shows the total stellar mass (M_*), while the **lower row** shows the bulge stellar mass ($M_{*,\text{bulge}}$). The **left column** shows the results derived from the High- z_f variant of our model, while the **right column** shows those obtained from the Low- z_f variant. The **solid lines** represent the median relations, and the **shaded area** surrounding the $z = 0.1$ curve shows the $1-\sigma$ (16%-84%) quantiles at this redshift. See §5.4 for a detailed discussion.

to achieve the regime of AGN regulation. The observed transition at $M_{\text{bh}} 10^7 h^{-1} M_\odot$ may thus indicate a transition from the regime dominated by regulations of AGN feedback to a regime in which AGN feedback is either no longer important in affecting the gas, or working in a way such that its effect is not limited by the potential of halo. Note that the extra growth of M_{bh} in Low- z_f relative to that in High- z_f occurred at relatively late time when the condition is already favorable for the formation of a disk-like structure and unfavorable for the AGN feedback to affect the gas in a self-regulated way.

In Fig. 15 we show the stellar mass - halo mass relation for galaxies at different redshift, predicted by our model assuming the High- z_f variant (left panels) and Low- z_f variant (right panels). Results are shown separately for the total stellar mass (M_* , upper panels) and the mass of the dynamically hot (bulge) component ($M_{*,\text{bulge}}$, lower panels). Galaxies in massive halos with $10^{13} h^{-1} M_\odot$ are dominated by the bulge component, regardless of the definition of z_f . The stellar mass - halo mass relation is flattened and quite independent of z . This is the regime of ineffective cooling, which prevents star formation and thus ‘freezes’ the stellar mass before these halos enter into the slow regime. At $M_v \lesssim 10^{12.5} h^{-1} M_\odot$, galaxies are dominated by the disk component, particularly in the High- z_f variant. The time evolution of the stellar mass - halo mass relation then begins to appear, driven by the halo-mass-dependent star formation rate of disk formation in the slow phase. At $M_v \lesssim 10^{11} h^{-1} M_\odot$, the predicted stellar mass at a given halo mass is higher at higher z , particularly in the bulge mass. This evolution is driven by the halo-mass dependence of the transition time, and consequently, is stronger in the High- z variant. These results about the evolution of the $M_* - M_v$ relation are in qualitative agreement with those obtained using methods of abundance matching (e.g. Behroozi et al. 2013, 2019).

Fig. 16 shows the cosmic star formation rate density, ρ_{SFR} , as a function of redshift, in comparison with data compiled by Hopkins & Beacom (2006) and Zhang et al. (2022a). The two upper panels show

the total ρ_{SFR} (black thin curve), as well as those separated into the bulge (red) and disk (blue) components. Results obtained by High- z_f and Low- z_f are shown in the left and right panels, respectively. To deal with the intrinsic inconsistency between the observed evolution of the stellar mass function and the cosmic star formation rate density, we follow §3.5 of Behroozi et al. (2019) and scale the predicted ‘true’ star formation rate, SFR_{true} , to obtain a scaled version, $\text{SFR}_{\text{scaled}}$, given by

$$\log \left(\frac{\text{SFR}_{\text{scaled}}}{\text{SFR}_{\text{true}}} \right) = \mu(z) + \kappa \exp \left[-\frac{(z-2)^2}{2} \right], \quad (84)$$

where $\mu(z) = 0.041 - 0.044z/(1+z)$ and $\kappa = 0.314$. The total scaled ρ_{SFR} is shown by the thick black curve in the upper panels of Fig. 16, and this curve should only be used when we compare our results with observational measurements on ρ_{SFR} . At $z \lesssim 1.5$, the two variants match the observed density equally well, with only slight difference that falls within the uncertainty of the observational data. The divergence emerges at $z \gtrsim 1.5$ and becomes the most significant at $z \approx 2$. At this epoch, the High- z_f variant predicts a much higher star formation activity in disks than that in bulges, while the Low- z_f variant has a small but non-negligible bulge contribution. The observational data seem to favor the Low- z_f variant, similar to what we have seen in other statistical measures. At $z \gtrsim 3$, the star formation of the bulge component dominates the total ρ_{SFR} in the Low- z_f variant. As observations in such early times suffer from systematic effects, for example, in dust correction and sample completeness, it is difficult to obtain quantitative constraints on the model.

The lower panels of Fig. 16 shows the contribution to ρ_{SFR} by halos of different mass (left) and by galaxies of different stellar mass (right), as function of redshift assuming the Low- z_f variant. At $z \lesssim 3$, most of the cosmic ρ_{SFR} comes from halos with M_v in the range of $[10^{11.5}, 10^{12.5}] h^{-1} M_\odot$, or galaxies with M_* in the range of $[10^{10.0}, 10^{11.0}] h^{-1} M_\odot$. This is exactly the population of halos

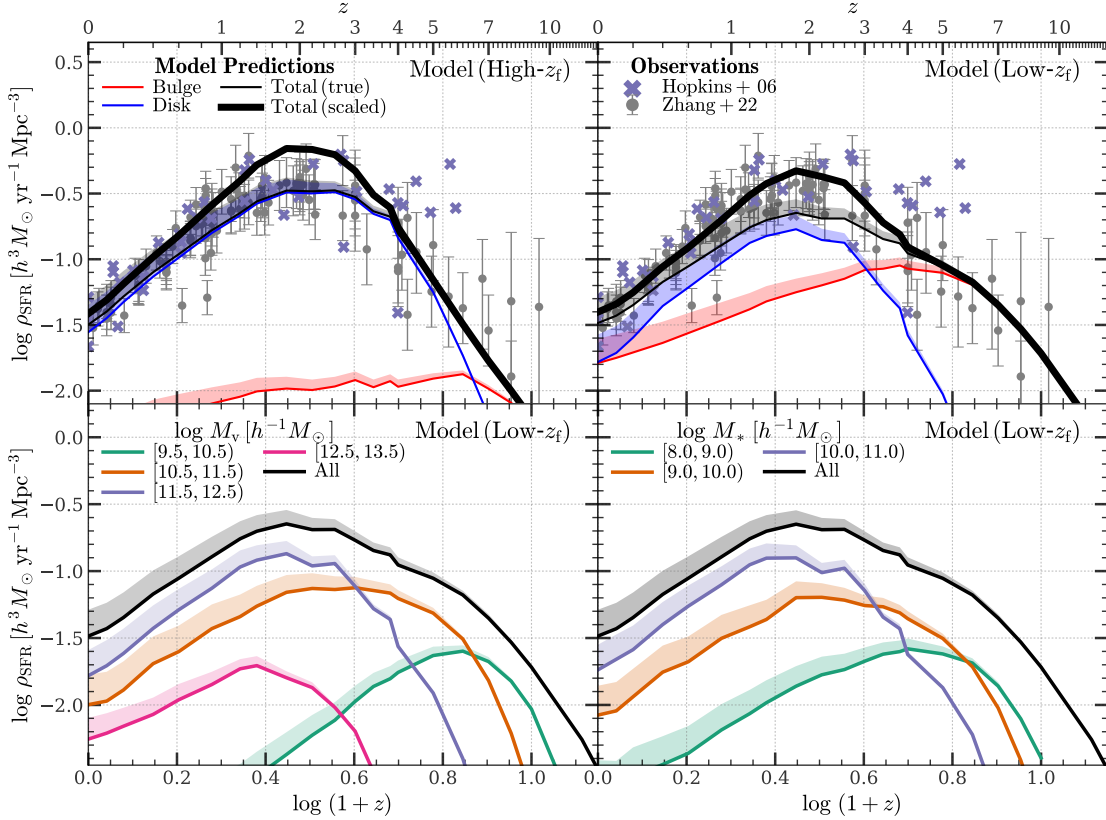


Figure 16. Cosmic star formation rate density ρ_{SFR} . The **upper-left panel** shows the total ρ_{SFR} , and those decomposed as bulge and disk components, all obtained by the High- z_f variant. **Thin curves** represent the true values predicted by our model, while the **thick black curve** shows the scaled values for comparison with observational data, corrected according to §3.5 of Behroozi et al. (2019) to account for the intrinsic inconsistency between the observed evolution of stellar mass functions and cosmic star formation rate density. Observational data points compiled by Hopkins & Beacom (2006, **cross markers**) and Zhang et al. (2022a, **dots with errorbars**) are shown. The **upper-right panel** is similar, but with the Low- z_f variant. The **lower panels**, obtained using the Low- z_f variant, show a decomposition by halo mass in the **left panel** and a decomposition by stellar mass in the **right panel**. In all panels, the shaded area around each curve indicates the uncertainties contributed by satellite galaxies. This figure shows that it is the same population of halos that drive the cosmic star formation throughout the entire history of the Universe, and that the star formation activity of the Universe is not concentrated around a well-defined period around $z \sim 2$ but rather has a more extended distribution in time. See §5.4 for a detailed discussion.

(galaxies) that have peak efficiency in star formation (represented by M_*/M_V) at $z = 0$ (Yang et al. 2012, see also Fig. 12). At $z \gtrsim 3$, the contribution to ρ_{SFR} comes mainly from halos with M_V in the range of $[10^{10.5}, 10^{11.5}] h^{-1} M_\odot$, or galaxies with M_* in the range of $[10^{9.0}, 10^{10.0}] h^{-1} M_\odot$. Using halo assembly histories shown in Fig. 6, one can infer that these halos are exactly the progenitors of the halos that contribute the most to the cosmic ρ_{SFR} at $z \lesssim 3$. Thus, it is the same population of halos that drives the cosmic star formation throughout the entire history of the Universe.

One interesting feature in the prediction of the Low- z_f variant, which is preferred by observational data, is the presence of a slowly evolving plateau of the total ρ_{SFR} at redshift $1 \lesssim z \lesssim 5$. This plateau is produced by the combined contribution of two components. The first is peaked at $z \approx 5$ with a $\rho_{\text{SFR}} \approx 10^{-1} h^3 M_\odot \text{yr}^{-1} \text{Mpc}^{-3}$ (red curve in the upper right panel), and produced when a significant fraction of the ρ_{SFR} contributors enter the ‘feedback-free’ regime for the bulge formation (see Fig. 6 and §4.4). The second one is peaked at $z \approx 2$ with a $\rho_{\text{SFR}} \approx 10^{-0.75} h^3 M_\odot \text{yr}^{-1} \text{Mpc}^{-3}$ (blue curve in the upper right panel), and produced when these contributors switch to the slow assembly phase and begin to form dynamically cold disks. The predicted peak at $z \approx 2$ has numerous observational supports (e.g. Le Borgne et al. 2009; Dunne et al. 2009; Kajisawa et al. 2010;

Karim et al. 2011; Cucciati et al. 2012; Sobral et al. 2014; Behroozi et al. 2019). The peak around $z \approx 5$ is a prediction of our model and can be tested by ongoing and future observations (e.g. DESI, JWST, PFS and Roman). If confirmed, the concept of the cosmic noon may need to be re-defined, as the star formation activity of the universe is not concentrated around a well-defined period around $z \sim 2$, but rather has a more extended distribution in time.

6 SUMMARY AND DISCUSSION

In this paper, we have developed a two-phase framework to understand galaxy formation and the growth of central supermassive black holes (SMBHs) in dark matter halos predicted by current cosmology. The main components of the framework and the predictions of the model are summarized below.

- (i) The framework uses the fact that the assembly of a cold dark matter (CDM) halo in general consists of two phases, a fast phase in which its gravitational potential well changes and deepens rapidly with time, and a slow phase in which the halo mass increases gently without changing much the gravitational potential. We used simulated halo

Table 1. List of model components, their functional forms and the default parameters adopted in this paper for the co-evolution of different mass components. See §4.4 for the detailed definitions, Fig. 5 for a schematic diagram and Appendix D for the strategy of adjusting model parameters.

Model Component	Functional	Default Parameter
Phase transition (eqs. 10, 11)	$\gamma(z_f) = \gamma_f$	$\gamma_f = 3/8$ (High- z_f variant); $\gamma_f = 0$ (Low- z_f variant)
Black hole seeding (eq. 72)	$M_{\text{bh,init}}(M_V M_{\text{bh,min}}, m_{\text{bh, scale}})$ at $M_{V,\text{min}}$	$M_{V,\text{min}} = 10^9 h^{-1} M_\odot$; $M_{\text{bh,min}} = 10 h^{-1} M_\odot$; $m_{\text{bh, scale}} = 10^{-10}$
Gas cooling (eq. 23)	$F_{\text{cool}}(M_V M_{\text{cool}}, \beta_{\text{cool}})$	$M_{\text{cool}} = 10^{13} h^{-1} M_\odot$; $\beta_{\text{cool}} = 4$
Feedbacks (eqs. 68, 60, 69)	$F_{\text{sn}}(V_g \alpha_{\text{sn}}, \beta_{\text{sn}}, V_w)$; $F_{\text{agn}}(M_{\text{bh}}, M_g, V_g \alpha_{\text{agn}})$	$\alpha_{\text{sn}} = 0$; $\beta_{\text{sn}} = 2.5$; $V_w = 250 \text{ km s}^{-1}$; $\alpha_{\text{agn}} = 10^{-3}$
Star formation and SMBH growth (eqs. 77, 78)	ΔM_* ($\Delta M_{g,\text{sf}} \epsilon_{*,f}$); ΔM_{bh} ($\Delta M_{g,\text{sf}} \alpha_{\text{cap}}, F_{\text{en}}$); $F_{\text{en}}(M_V \alpha_{\text{en}}, \beta_{\text{en}}, M_{\text{en}})$	$\epsilon_{*,f} = 0.75$; $\alpha_{\text{cap}} = 2.5$; $\alpha_{\text{en}} = 3$; $\beta_{\text{en}} = 2$; $M_{\text{en}} = 10^{11.5} h^{-1} M_\odot$
Gas evolution (eq. 79)	$\Delta M_{g,\text{ej}}(\Delta M_{g,\text{cool}} f_{\text{ej,sn}}, f_{\text{ej,agn}}, F_{\text{sn}}, F_{\text{agn}})$	$f_{\text{ej,sn}} = f_{\text{ej,agn}} = 0.75$

assembly histories to design a critical redshift that separates the two phases of a given history and to quantify uncertainties in the separation.

- (ii) Our modeling also uses the fact that the universal baryon fraction is high, so that cooled gas in a primordial, unprocessed halo becomes self-gravitating before it can form a rotation-supported disk. The gas associated with the fast assembly is thus expected to form a self-gravitating cloud (SGC) that is inherently turbulent because of the fast variation of the gravitational potential.
- (iii) The density and size of an SGC in a halo can be estimated from the assembly history of the halo and the cold gas fraction. Jeans instability causes the SGC to fragment and form sub-clouds with a typical mass of $\sim 10^7 M_\odot$.
- (iv) Sub-clouds in SGC are sufficiently compact so that cloud-cloud collision and drag force on clouds can be neglected. An SGC is thus a dynamically hot system of sub-clouds that form stars and move ballistically to feed the central SMBH.
- (v) Under the assumption of random ballistic motion of sub-clouds, we estimated the mass accretion rate of an existing SMBH. We found that such an accretion can achieve the Eddington limit, thus providing a viable channel for the growth of SMBH.
- (vi) We assumed that AGN and supernova feedbacks are effective only in the fast phase, where sub-clouds have a more isotropic distribution. The feedback efficiency is also enhanced because individual sub-clouds can be dispersed by supernova (SN) feedback associated with the star formation in them.
- (vii) The cumulative effects of AGN and SN feedback in an SGC are twofold: regulating star formation and SMBH growth, while simultaneously reducing the amount of cold gas within the halo to facilitate the formation of globally stable disks. Consequently, the feedback mechanism manifests itself as ‘ejective’ during the fast assembly phase and transitions to a ‘preventive’ mode when galactic disks begin to form during the slow assembly phase.
- (viii) Quenching of star formation through feedback is only effective in dynamically hot systems form during the fast assembly phase, but not effective in disk-dominated systems that form later in the slow assembly phase.
- (ix) We have applied our model to a set of realistic halo assembly histories to make predictions and make comparisons with observational data.
- (x) We found that an early phase of enhancement in SMBH accretion is needed to grow SMBH if the seeding mass is small. We suggested that the SN feedback in low-mass progenitor halos, where cooling is very effective, can quickly re-generate sub-clouds in the turbulent medium to enhance the accretion rate of early SMBH.
- (xi) The predicted correlations of SMBH mass (M_{bh}) with the stellar mass of central galaxies (M_*) and with the host halo mass (M_V) match well observational results. The predicted $M_{\text{bh}}-M_*$ relation for dynamically hot galaxies in the massive end follows roughly a power law, $M_{\text{bh}} \propto M_*^{5/3}$, expected from the regulation by AGN feedback. The predicted relation deviates from this relation for galaxies with $M_* < 10^{10} M_\odot$ because they have not reached the regime of the AGN regulation. For a similar reason, M_{bh} is predicted to correlate more tightly with M_V than with M_* in the massive end, $M_{\text{bh}} > 10^7 h^{-1} M_\odot$. At lower M_{bh} the stellar mass of galaxies becomes the more important factor in producing the correlation, as the regulation by the AGN feedback becomes ineffective in the more disk-like structure expected for these galaxies.
- (xii) The predicted $M_{\text{bh}}-M_*$ relation for dynamically hot galaxies is quite independent of redshift. The relation steepens significantly with decreasing redshift if M_* contains both dynamically hot (bulge) and cold (disk) masses. The predicted $M_{\text{bh}} - M_V$ relation also steepens with decreasing redshift, but only mildly.
- (xiii) The predicted cosmic SMBH mass density as a function of z matches observational results, but the predicted density of mass accretion rate by SMBH at $z < 1$ is lower than that observed. This suggests that other channels of SMBH growth, such as those associated with the formation of pseudo bulges, and recent mergers of disk galaxies, are needed at low z .
- (xiv) The stellar mass - halo mass relation predicted by our model is in good agreement with those obtained from observational data. Our model predicts that, at a given mass, older halos (those with higher formation redshift) tend to host galaxies that are more disk-dominated. Similarly, the model predicts that, at a given stellar mass, disk-dominated galaxies on average have lower halo mass than bulge-dominated ones. This prediction naturally emerges as a consequence of the earlier transition of more massive halos, and it appears in good agreement with results obtained from galaxy-galaxy gravitational lensing.
- (xv) Redshift evolution of the stellar mass - halo mass relation predicted by our model is in qualitative agreement with those obtained from abundance matching. The predicted cosmic star formation rate density as a function of z matches observational data at $z \leq 5$, and has a slowly evolving plateau between $1 \lesssim z \lesssim 5$ due to the superposition of a bulge-forming peak and a disk-forming peak.

The presentation of our framework given above is based on a set of simple assumptions. This makes our model transparent so that we can see clearly how different assumptions affect the model prediction. We purposely avoid fine-tuning model parameters, so that one can see the success and failure of the model faithfully. Clearly, many assumptions made in our model need to be checked by looking

into how the relevant processes operate in realistic settings. The best approach is perhaps through the use of zoom-in simulations of individual halos that can resolve star-forming clouds with masses below $10^7 M_{\odot}$. The critical things to check are: (i) the properties of the turbulent medium associated with the fast assembly phase to see to what extent the SGC envisaged in our model can be produced; (ii) the formation, disruption and motion of sub-clouds in the SGC to check to what extent the assumption of ballistic motion is valid, and whether or not sub-clouds can be produced at sufficient rates to sustain star formation and SMBH growth; (iii) the rate at which sub-clouds can reach the halo center to be accreted by an existing SMBH; (iv) the efficiency at which central AGN and SN feedback disperses, heats and ejects gas in a dynamically hot SGC of star-forming sub-clouds; (v) to what extent the feedback from the SGC can preheat and pre-process the halo gas so as to affect the subsequent assembly of gas to form galactic disks. Current state-of-the-art computational facilities and numerical methods are powerful enough to simulate these processes. The model and results presented in this paper can thus be used to motivate, and identify cases for, such simulations.

One direct consequence of our two-phase model is the inside-out quenching of galaxies, as central bulge stars in our model form earlier than the surrounding disk stars. Indeed, this inside-out trend has been found in observational data. For example, using MaNGA data [Lin et al. \(2019\)](#) found that the inside-out quenching is the dominant mode in all environments, and that the signal is stronger in more massive galaxies, regardless of environment. They invoked morphological quenching to explain their findings. Similar results have also been found by [Li et al. \(2015\)](#) using the P-MaNGA data, and by [Nelson et al. \(2021\)](#) using 3D-HST data. Such inside-out quenching is expected in our model by the fact that more massive systems have later transition times and hence longer time for the bulge component to grow.

Our model also suggests a scenario in which AGN feedback is not expected to be significant in affecting the gas (or the feedback is limited to a small fraction of the halo gas) in the slow assembly phase. This is consistent with the observational results for galaxies at $z \leq 0.35$ obtained by [Zhuang & Ho \(2023\)](#), who concluded that instantaneous feedback from accreting SMBH in quenching star formation may not be efficient. However, this scenario seems in contradiction with recent cosmological simulations ([Weinberger et al. 2018](#); [Davé et al. 2019](#)), and so the question remains open.

The plateau feature of the cosmic star formation history predicted by our model indicates strong star formation activity at $z \sim 5$ in the self-gravitating SGC. Recent JWST observations revealed a population of massive galaxies at $z \gtrsim 5$ with significant ongoing star formation activities ([Xiao et al. 2023](#)), which is in qualitative agreement with our model prediction. Further information from high-redshift observations will be needed to give quantitative constraints on the model.

ACKNOWLEDGEMENTS

YC is funded by the China Postdoctoral Science Foundation (grant No. 2022TQ0329). HJM thanks T.D. Lee Institute and Shanghai Jiaotong University for hosting his sabbatical during which the work was done. This work is also supported by the National Natural Science Foundation of China (NSFC, Nos. 12192224, 11733004 and 11890693) and CAS Project for Young Scientists in Basic Research (grant No. YSBR-062). YC thanks Kai Wang, Hui Hong, Hao Li, Yu Rong, Enci Wang, Wentao Luo and Fangzhou Jiang for their valuable insights and discussions. The authors would like to express their

gratitude to the Tsinghua Astrophysics High-Performance Computing platform at Tsinghua University and the Supercomputer Center of the University of Science and Technology of China for providing the necessary computational and data storage resources that have significantly contributed to the research results presented in this paper. The authors thank [Behroozi et al. \(2019\)](#), [Zhang et al. \(2022a\)](#) and [Wu et al. \(2022\)](#) for compiling observational data and making them publicly available. The computations and presentations in this paper are supported by various software tools, including the HPC toolkits HIPP ([Chen & Wang 2023](#))² and PyHIPP³, interactive computation environment IPYTHON ([Perez & Granger 2007](#)), numerical libraries NUMPY ([Harris et al. 2020](#)), ASTROPY ([Robitaille et al. 2013](#); [Astropy Collaboration et al. 2018, 2022](#)), SCIPY ([Virtanen et al. 2020](#)) and PYTREEGRAV⁴, as well as the graphical library MATPLOTLIB ([Hunter 2007](#)). This research has made extensive use of the arXiv and NASA's Astrophysics Data System. Data compilations used in this paper have been made much more accurate and efficient by the software WEBPLOTDIGITIZER.

DATA AVAILABILITY

We provide a code repository, `TwoPhaseGalaxyModel`⁵, that implements the model described in this paper. The library is written in Python and can be applied to halo assembly histories from different sources, such as N-body simulations or Monte Carlo methods. All data used in this paper, including halo assembly histories, modeled galaxies and SMBHs, data points displayed in figures, and observational results used for calibration and testing, will be distributed along with the repository.

REFERENCES

- Abuter R., et al., 2024, A Dynamical Measure of the Black Hole Mass in a Quasar 11 Billion Years Ago (arxiv:2401.14567), doi:10.1038/s41586-024-07053-4
- Adamo A., et al., 2024, The Discovery of Bound Star Clusters 460 Myr after the Big Bang, doi:10.48550/arXiv.2401.03224
- Astropy Collaboration et al., 2018, *The Astronomical Journal*, 156, 123
- Astropy Collaboration et al., 2022, *The Astrophysical Journal*, 935, 167
- Bauer A. E., et al., 2013, *Monthly Notices of the Royal Astronomical Society*, 434, 209
- Behroozi P. S., Wechsler R. H., Conroy C., 2013, *ApJ*, 770, 57
- Behroozi P., Wechsler R. H., Hearin A. P., Conroy C., 2019, *Monthly Notices of the Royal Astronomical Society*, 488, 3143
- Bett P., Eke V., Frenk C. S., Jenkins A., Helly J., Navarro J., 2007, *Monthly Notices of the Royal Astronomical Society*, 376, 215
- Bluck A. F. L., Maiolino R., Sánchez S. F., Ellison S. L., Thorp M. D., Piotrowska J. M., Teimoorinia H., Bundy K. A., 2020, *Monthly Notices of the Royal Astronomical Society*, 492, 96
- Bluck A. F. L., Maiolino R., Brownson S., Conselice C. J., Ellison S. L., Piotrowska J. M., Thorp M. D., 2022, *A&A*, 659, A160
- Boco L., Lapi A., Shankar F., Fu H., Gabrielli F., Sicilia A., 2023, TOPSEM, Two Parameters Semi Empirical Model: Galaxy Evolution and Bulge/Disk Dichotomy from Two-Stage Halo Accretion (arxiv:2307.13036), doi:10.48550/arXiv.2307.13036
- Booth C. M., Schaye J., 2013, *Scientific Reports*, p. 1738

² <https://github.com/ChenYangyao/hipp>

³ <https://github.com/ChenYangyao/pyhipp>

⁴ <https://github.com/mikegrudic/pytreegrav>

⁵ <https://github.com/ChenYangyao/two-phase-galaxy-model>

- Bouwens R. J., et al., 2023, *Monthly Notices of the Royal Astronomical Society*, 523, 1036
- Bower R. G., Schaye J., Frenk C. S., Theuns T., Schaller M., Crain R. A., McAlpine S., 2017, *Monthly Notices of the Royal Astronomical Society*, 465, 32
- Boylan-Kolchin M., 2023, *Nat Astron*
- Boylan-Kolchin M., Springel V., White S. D. M., Jenkins A., Lemson G., 2009, *Monthly Notices of the Royal Astronomical Society*, 398, 1150
- Bullock J. S., Kolatt T. S., Sigad Y., Somerville R. S., Kravtsov A. V., Klypin A. A., Primack J. R., Dekel A., 2001a, *Monthly Notices of the Royal Astronomical Society*, 321, 559
- Bullock J. S., Dekel A., Kolatt T. S., Kravtsov A. V., Klypin A. A., Porciani C., Primack J. R., 2001b, *ApJ*, 555, 240
- Burkert A., et al., 2016, *ApJ*, 826, 214
- Ceverino D., Dekel A., Bournaud F., 2010, *Monthly Notices of the Royal Astronomical Society*, 404, 2151
- Chen Y., Wang K., 2023, Astrophysics Source Code Library, p. ascl:2301.030
- Chen Y., Mo H. J., Li C., Wang H., Yang X., Zhang Y., Wang K., 2020, *ApJ*, 899, 81
- Chen Y., Mo H. J., Li C., Wang K., 2021, *Monthly Notices of the Royal Astronomical Society*, 504, 4865
- Chen Y., Mo H., Wang H., 2023a, A Two-Phase Model of Galaxy Formation: II. The Size-Mass Relation of Dynamically Hot Galaxies, doi:10.48550/arXiv.2311.11713
- Chen Y., Mo H. J., Wang K., 2023b, *Monthly Notices of the Royal Astronomical Society*, 526, 2542
- Chen Y., Mo H., Wang H., 2024, A Two-Phase Model of Galaxy Formation: III. The Formation of Globular Clusters (arxiv:2405.18735)
- Chevance M., et al., 2020, *Monthly Notices of the Royal Astronomical Society*, 493, 2872
- Conroy C., White M., 2013, *The Astrophysical Journal*, 762, 70
- Cook M., Lapi A., Granato G. L., 2009, *Monthly Notices of the Royal Astronomical Society*, 397, 534
- Correa C. A., Wyithe J. S. B., Schaye J., Duffy A. R., 2015, *Monthly Notices of the Royal Astronomical Society*, 450, 1514
- Crain R. A., et al., 2015, *Monthly Notices of the Royal Astronomical Society*, 450, 1937
- Cucciati O., et al., 2012, *A&A*, 539, A31
- Cui W., Davé R., Peacock J. A., Anglés-Alcázar D., Yang X., 2021, The Origin of Galaxy Colour Bimodality in the Scatter of the Stellar-to-Halo Mass Relation (arxiv:2105.12145), doi:10.48550/arXiv.2105.12145
- Danovich M., Dekel A., Hahn O., Ceverino D., Primack J., 2015, *Monthly Notices of the Royal Astronomical Society*, 449, 2087
- Davé R., Anglés-Alcázar D., Narayanan D., Li Q., Rafieferantsoa M. H., Appleby S., 2019, *Monthly Notices of the Royal Astronomical Society*, 486, 2827
- Davis M., Efstathiou G., Frenk C. S., White S. D. M., 1985, *The Astrophysical Journal*, 292, 371
- De Lucia G., Blaizot J., 2007, *Monthly Notices of the Royal Astronomical Society*, 375, 2
- Dekel A., Burkert A., 2014, *Monthly Notices of the Royal Astronomical Society*, 438, 1870
- Dekel A., Silk J., 1986, *The Astrophysical Journal*, 303, 39
- Dekel A., Sari R., Ceverino D., 2009, *The Astrophysical Journal*, 703, 785
- Dekel A., Zolotov A., Tweed D., Cacciato M., Ceverino D., Primack J. R., 2013, *Monthly Notices of the Royal Astronomical Society*, 435, 999
- Dekel A., Sarkar K. C., Birnboim Y., Mandelker N., Li Z., 2023, *Monthly Notices of the Royal Astronomical Society*, 523, 3201
- Desmond H., Wechsler R. H., 2015, *Monthly Notices of the Royal Astronomical Society*, 454, 322
- Dolag K., Borgani S., Murante G., Springel V., 2009, *Monthly Notices of the Royal Astronomical Society*, 399, 497
- Donnan C. T., et al., 2022, *Monthly Notices of the Royal Astronomical Society*, 518, 6011
- Dunne L., et al., 2009, *Monthly Notices of the Royal Astronomical Society*, 394, 3
- Dutton A. A., Macciò A. V., Frings J., Wang L., Stinson G. S., Penzo C., Kang X., 2016, *Monthly Notices of the Royal Astronomical Society*, 457, L74
- El-Badry K., Wetzel A., Geha M., Hopkins P. F., Kereš D., Chan T. K., Faucher-Giguère C.-A., 2016, *The Astrophysical Journal*, 820, 131
- Feldmann R., Gnedin N. Y., 2011, *The Astrophysical Journal*, 727, L12
- Ferreira L., et al., 2023, *The Astrophysical Journal*, 955, 94
- Finkelstein S. L., et al., 2022, *ApJL*, 940, L55
- Finkelstein S. L., et al., 2023, *ApJL*, 946, L13
- Fujimoto S., et al., 2024, Primordial Rotating Disk Composed of $\gtrsim 15$ Dense Star-Forming Clumps at Cosmic Dawn, doi:10.48550/arXiv.2402.18543
- Genel S., et al., 2014, *Monthly Notices of the Royal Astronomical Society*, 445, 175
- Graham A. W., Sahu N., 2023, *Monthly Notices of the Royal Astronomical Society*, 518, 2177
- Greene J. E., Strader J., Ho L. C., 2020, *Annual Review of Astronomy and Astrophysics*, 58, 257
- Grudić M. Y., Kruijssen J. M. D., Faucher-Giguère C.-A., Hopkins P. F., Ma X., Quataert E., Boylan-Kolchin M., 2021, *Monthly Notices of the Royal Astronomical Society*, 506, 3239
- Harikane Y., et al., 2023, *ApJS*, 265, 5
- Harris C. R., et al., 2020, *Nature*, 585, 357
- Hearin A. P., Chaves-Montero J., Becker M. R., Alarcon A., 2021, *The Open Journal of Astrophysics*, 4, 7
- Hobbs A., Nayakshin S., Power C., King A., 2011, *Monthly Notices of the Royal Astronomical Society*, 413, 2633
- Hong H., et al., 2023, *The Astrophysical Journal*, 954, 183
- Hopkins A. M., Beacom J. F., 2006, *The Astrophysical Journal*, 651, 142
- Hu J., 2008, *Monthly Notices of the Royal Astronomical Society*, 386, 2242
- Hunter J. D., 2007, *Computing in Science & Engineering*, 9, 90
- Ji Z., Gialavisco M., 2023, *ApJ*, 943, 54
- Ji S., Oh S. P., Masterson P., 2019, *Monthly Notices of the Royal Astronomical Society*, 487, 737
- Jiang F., et al., 2019, *Monthly Notices of the Royal Astronomical Society*, 488, 4801
- Kajisawa M., Ichikawa T., Yamada T., Uchimoto Y. K., Yoshikawa T., Akiyama M., Onodera M., 2010, *The Astrophysical Journal*, 723, 129
- Karim A., et al., 2011, *The Astrophysical Journal*, 730, 61
- Kartaltepe J. S., et al., 2023, *The Astrophysical Journal*, 946, L15
- Kelly B. C., Shen Y., 2013, *The Astrophysical Journal*, 764, 45
- Klypin A., Kravtsov A. V., Bullock J. S., Primack J. R., 2001, *The Astrophysical Journal*, 554, 903
- Krumholz M. R., Tan J. C., 2007, *The Astrophysical Journal*, 654, 304
- Krumholz M. R., McKee C. F., Bland-Hawthorn J., 2019, *Annual Review of Astronomy and Astrophysics*, 57, 227
- Kuhn V., Guo Y., Martin A., Bayless J., Gates E., Puleo A. J., 2023, JWST Reveals a Surprisingly High Fraction of Galaxies Being Spiral-like at $0.5 \leq z \leq 4$, doi:10.48550/arXiv.2312.12389
- Labbé I., et al., 2023, *Nature*, 616, 266
- Latif M. A., Whalen D. J., Khochfar S., Herrington N. P., Woods T. E., 2022, *Nature*, 607, 48
- Le Borgne D., Elbaz D., Ocvirk P., Pichon C., 2009, *Astronomy and Astrophysics*, 504, 727
- Lee J. H., Park C., Hwang H. S., Kwon M., 2023, Morphology of Galaxies in JWST Fields: Initial Distribution and Evolution of Galaxy Morphology, doi:10.48550/arXiv.2312.04899
- Li Y., Mo H. J., Gao L., 2008, *Monthly Notices of the Royal Astronomical Society*, 389, 1419
- Li C., et al., 2015, *The Astrophysical Journal*, 804, 125
- Lin L., et al., 2019, *The Astrophysical Journal*, 872, 50
- Lin X., et al., 2023, *The Astrophysical Journal*, 944, L59
- Lovell C. C., Harrison I., Harikane Y., Tacchella S., Wilkins S. M., 2022, *Monthly Notices of the Royal Astronomical Society*, 518, 2511
- Lu Y., Mo H. J., Katz N., Weinberg M. D., 2006, *Monthly Notices of the Royal Astronomical Society*, 368, 1931
- Lu Z., Mo H. J., Lu Y., Katz N., Weinberg M. D., van den Bosch F. C., Yang X., 2014, *Monthly Notices of the Royal Astronomical Society*, 439, 1294
- Lu Y., Mo H. J., Wechsler R. H., 2015, *Monthly Notices of the Royal Astronomical Society*, 446, 1907

- Ma X., et al., 2018, *Monthly Notices of the Royal Astronomical Society*, 478, 1694
- Ma X., et al., 2020, *Monthly Notices of the Royal Astronomical Society*, 493, 4315
- Macciò A. V., Dutton A. A., Van Den Bosch F. C., Moore B., Potter D., Stadel J., 2007, *Monthly Notices of the Royal Astronomical Society*, 378, 55
- Maiolino R., et al., 2023, JADES. The Diverse Population of Infant Black Holes at 4, doi:10.48550/arXiv.2308.01230
- Mandelbaum R., Wang W., Zu Y., White S., Henriques B., More S., 2016, *Mon. Not. R. Astron. Soc.*, 457, 3200
- Mandelker N., van Dokkum P. G., Brodie J. P., van den Bosch F. C., Ceverino D., 2018, *The Astrophysical Journal*, 861, 148
- Mao Y.-Y., Zentner A. R., Wechsler R. H., 2018, *Monthly Notices of the Royal Astronomical Society*, 474, 5143
- Marconi A., Risaliti G., Gilli R., Hunt L. K., Maiolino R., Salvati M., 2004, *Monthly Notices of the Royal Astronomical Society*, 351, 169
- Mason C. A., Trenti M., Treu T., 2023, *Monthly Notices of the Royal Astronomical Society*, 521, 497
- McBride J., Fakhouri O., Ma C.-P., 2009, *Monthly Notices of the Royal Astronomical Society*, 398, 1858
- McConnell N. J., Ma C.-P., 2013, *The Astrophysical Journal*, 764, 184
- Meng J., Li C., Mo H. J., Chen Y., Jiang Z., Xie L., 2023, *The Astrophysical Journal*, 944, 75
- Merloni A., Heinz S., 2008, *Monthly Notices of the Royal Astronomical Society*, 388, 1011
- Mo H. J., Mao S., 2002, *Monthly Notices of the Royal Astronomical Society*, 333, 768
- Mo H. J., Mao S., 2004, *Monthly Notices of the Royal Astronomical Society*, 353, 829
- Mo H. J., Mao S., White S. D. M., 1998, *Monthly Notices of the Royal Astronomical Society*, 295, 319
- Mo H., van den Bosch F., White S., 2010, *Galaxy Formation and Evolution*. Cambridge University Press
- More S., Diemer B., Kravtsov A. V., 2015, *The Astrophysical Journal*, 810, 36
- Mowla L., et al., 2024, The Firefly Sparkle: The Earliest Stages of the Assembly of A Milky Way-type Galaxy in a 600 Myr Old Universe, doi:10.48550/arXiv.2402.08696
- Murray S., 2014, *Astrophysics Source Code Library*, p. ascl:1412.006
- Naidu R. P., et al., 2022, *ApJL*, 940, L14
- Navarro J. F., Frenk C. S., White S. D. M., 1997, *ApJ*, 490, 493
- Nelson D., et al., 2019, *Computational Astrophysics and Cosmology*, 6, 2
- Nelson E. J., et al., 2021, *Monthly Notices of the Royal Astronomical Society*, 508, 219
- Ormerod K., et al., 2024, *Monthly Notices of the Royal Astronomical Society*, 527, 6110
- Pandya V., et al., 2024, *The Astrophysical Journal*, 963, 54
- Perez F., Granger B. E., 2007, *Computing in Science and Engineering*, 9, 21
- Pillepich A., et al., 2018a, *Monthly Notices of the Royal Astronomical Society*, 473, 4077
- Pillepich A., et al., 2018b, *Monthly Notices of the Royal Astronomical Society*, 475, 648
- Planck Collaboration et al., 2016, *Astronomy and Astrophysics*, 594, A13
- Robitaille T. P., et al., 2013, *A&A*, 558, A33
- Rodighiero G., Bisigello L., Iani E., Marasco A., Grazian A., Sinigaglia F., Cassata P., Gruppioni C., 2022, JWST Unveils Heavily Obscured (Active and Passive) Sources up to $z \sim 13$, https://arxiv.org/abs/2208.02825v2, doi:10.1093/mnras/slac115
- Rodríguez-Gomez V., et al., 2015, *Monthly Notices of the Royal Astronomical Society*, 449, 49
- Sacchi E., et al., 2021, *The Astrophysical Journal*, 920, L19
- Saglia R. P., et al., 2016, *The Astrophysical Journal*, 818, 47
- Schaye J., et al., 2015, *Monthly Notices of the Royal Astronomical Society*, 446, 521
- Schulze A., Wisotzki L., 2014, *Monthly Notices of the Royal Astronomical Society*, 438, 3422
- Schulze A., et al., 2015, *Monthly Notices of the Royal Astronomical Society*, 447, 2085
- Shankar F., Weinberg D. H., Miralda-Escudé J., 2009, *The Astrophysical Journal*, 690, 20
- Shankar F., Weinberg D. H., Miralda-Escudé J., 2013, *Monthly Notices of the Royal Astronomical Society*, 428, 421
- Shankar F., et al., 2020, *Nature Astronomy*, 4, 282
- Shapiro S. L., Teukolsky S. A., 1986, *Black Holes, White Dwarfs and Neutron Stars: The Physics of Compact Objects*
- Shen S., Mo H. J., White S. D. M., Blanton M. R., Kauffmann G., Voges W., Brinkmann J., Csabai I., 2003, *Monthly Notices of the Royal Astronomical Society*, 343, 978
- Shen X., Vogelsberger M., Boylan-Kolchin M., Tacchella S., Kannan R., 2023, *Monthly Notices of the Royal Astronomical Society*, 525, 3254
- Shimasaku K., Izumi T., 2019, *The Astrophysical Journal*, 872, L29
- Sobral D., Best P. N., Smail I., Mobasher B., Stott J., Nisbet D., 2014, *Monthly Notices of the Royal Astronomical Society*, 437, 3516
- Somerville R. S., et al., 2008, *The Astrophysical Journal*, 672, 776
- Somerville R. S., et al., 2018, *Monthly Notices of the Royal Astronomical Society*, 473, 2714
- Springel V., 2005, *Monthly Notices of the Royal Astronomical Society*, 364, 1105
- Springel V., 2010, *Monthly Notices of the Royal Astronomical Society*, 401, 791
- Springel V., Hernquist L., 2003, *Monthly Notices of the Royal Astronomical Society*, 339, 289
- Springel V., White S. D. M., Tormen G., Kauffmann G., 2001, *Monthly Notices of the Royal Astronomical Society*, 328, 726
- Springel V., et al., 2018, *Monthly Notices of the Royal Astronomical Society*, 475, 676
- Sun W., Ho L. C., Zhuang M.-Y., Ma C., Chen C., Li R., 2024, *The Astrophysical Journal*, 960, 104
- Tacchella S., Dekel A., Carollo C. M., Ceverino D., DeGraf C., Lapiner S., Mandelker N., Primack Joel R., 2016, *Monthly Notices of the Royal Astronomical Society*, 457, 2790
- Tillson H., Devriendt J., Slyz A., Miller L., Pichon C., 2015, *Monthly Notices of the Royal Astronomical Society*, 449, 4363
- Tohill C., Bamford S. P., Conselice C. J., Ferreira L., Harvey T., Adams N., Austin D., 2024, *The Astrophysical Journal*, 962, 164
- Vanzella E., et al., 2022, *The Astrophysical Journal*, 940, L53
- Vanzella E., et al., 2023, *The Astrophysical Journal*, 945, 53
- Vega-Ferrero J., et al., 2024, *The Astrophysical Journal*, 961, 51
- Virtanen P., et al., 2020, *Nat Methods*, 17, 261
- Vogelsberger M., et al., 2014, *Nature*, 509, 177
- Wang K., Mo H. J., Chen Y., Wang H., Yang X., Wang J., Peng Y., Cai Z., 2024, *Monthly Notices of the Royal Astronomical Society*, 528, 2046
- Wechsler R. H., Bullock J. S., Primack J. R., Kravtsov A. V., Dekel A., 2002, *ApJ*, 568, 52
- Weinberger R., et al., 2017, *Monthly Notices of the Royal Astronomical Society*, 465, 3291
- Weinberger R., et al., 2018, *Monthly Notices of the Royal Astronomical Society*, 479, 4056
- Weisz D. R., Savino A., Dolphin A. E., 2023, *The Astrophysical Journal*, 948, 50
- Willott C. J., et al., 2010, *The Astronomical Journal*, 140, 546
- Wong A. W. C., Taylor J. E., 2012, *ApJ*, 757, 102
- Woo J.-H., Schulze A., Park D., Kang W.-R., Kim S. C., Riechers D. A., 2013, *The Astrophysical Journal*, 772, 49
- Wu J., et al., 2022, *Monthly Notices of the Royal Astronomical Society*, 517, 2659
- Xiao M., et al., 2023, Massive Optically Dark Galaxies Unveiled by JWST Challenge Galaxy Formation Models (arxiv:2309.02492), doi:10.48550/arXiv.2309.02492
- Yang X., Mo H. J., van den Bosch F. C., Zhang Y., Han J., 2012, *ApJ*, 752, 41
- Yung L. Y. A., Somerville R. S., Finkelstein S. L., Wilkins S. M., Gardner J. P., 2023, Are the Ultra-High-Redshift Galaxies at $z > 10$ Surprising in the Context of Standard Galaxy Formation Models?, doi:10.48550/arXiv.2304.04348
- Zhang H., Behroozi P., Volonteri M., Silk J., Fan X., Hopkins P. F., Yang J.,

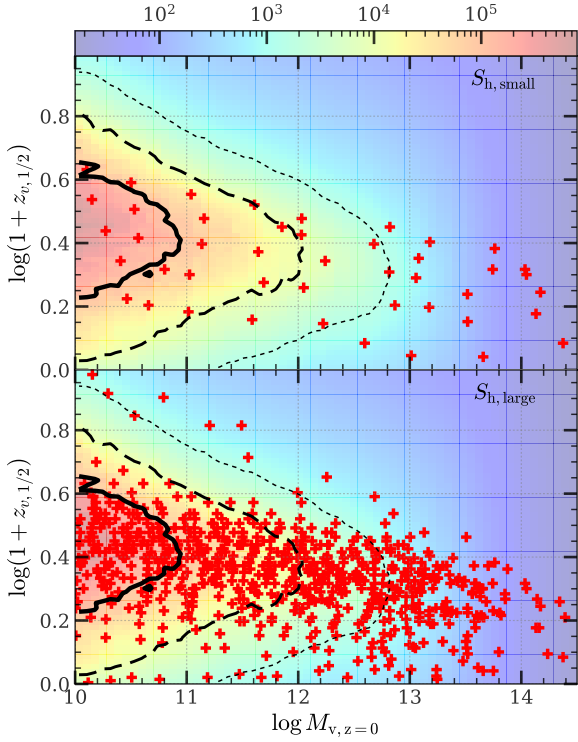


Figure A1. Halo samples extracted from N-body simulation. Each **plus marker** indicates an individual halo at $z = 0$. **Top:** the small sample, $S_{h,\text{small}}$, which consists of 45 halos with halo mass in the range of $[10^{10.0}, 10^{14.5}] h^{-1} M_{\odot}$. **Bottom:** the large sample $S_{h,\text{large}}$, which consists of 720 halos in the same mass range. Background colors, encoded according to the color bar, indicate the $M_{v,z=0} - z_{v,1/2}$ distribution of all halos at $z = 0$ in the simulation.

Aird J., 2022a, *Monthly Notices of the Royal Astronomical Society*, 518, 2123

Zhang Z., Wang H., Luo W., Zhang J., Mo H. J., Jing Y., Yang X., Li H., 2022b, *A&A*, 663, A85

Zhang Z., Wang H., Luo W., Mo H., Zhang J., Yang X., Li H., Li Q., 2023a, Halo Mass-Observable Proxy Scaling Relations and Their Dependencies on Galaxy and Group Properties, doi:10.48550/arXiv.2305.06803

Zhang S., et al., 2023b, *Science*, 380, 494

Zhao D. H., Mo H. J., Jing Y. P., Börner G., 2003, *Monthly Notices of the Royal Astronomical Society*, 339, 12

Zhao D. H., Jing Y. P., Mo H. J., Boerner G., 2009, *ApJ*, 707, 354

Zhou S., Li C., Hao C.-N., Guo R., Mo H., Xia X., 2020, arXiv:2011.13749 [astro-ph]

Zhuang M.-Y., Ho L. C., 2023, *Nat Astron*, pp 1–14

Zolotov A., et al., 2015, *Monthly Notices of the Royal Astronomical Society*, 450, 2327

van den Bosch F. C., 2002, *Monthly Notices of the Royal Astronomical Society*, 331, 98

APPENDIX A: THE METHODS OF SAMPLING HALOS AND THEIR ASSEMBLY HISTORIES

In §5.1, we briefly introduced the halo samples used in this paper. In this Appendix, we detail the techniques used to extract halos and their assembly histories from either N-body simulations of analytical fittings.

The main samples used in this paper are obtained from the IllustrisTNG100-1-Dark simulation. The simulation has a simulation

box with a side length $75 h^{-1} \text{Mpc}$, 1820^3 dark matter particles, each with a mass $6.0 \times 10^6 h^{-1} M_{\odot}$, a Plummer equivalent gravitational softening length varying from $1 h^{-1} \text{kpc}$ at high z to $0.5 h^{-1} \text{kpc}$ at low z . A total of 100 snapshots spanning from redshift $z = 20.0$ to 0 have been saved. Halos are identified using the friends-of-friends (FoF) algorithm with a scaled linking length of 0.2 (Davis et al. 1985). Subhalos are identified using the SUBFIND algorithm (Springel et al. 2001; Dolag et al. 2009), and subhalo merger trees are constructed using the SUBLINK algorithm (Springel 2005; Boylan-Kolchin et al. 2009; Rodriguez-Gomez et al. 2015). The lower limit for FoF halo mass is about $2 \times 10^8 h^{-1} M_{\odot}$. The main progenitor of a subhalo is defined as the one with the most massive history among all progenitors (De Lucia & Blaizot 2007; Rodriguez-Gomez et al. 2015). The central subhalo of a FoF halo is defined as the one with the most massive history among all subhalos within the halo. The main branch of an FoF halo corresponds to the main branch of its central subhalo. The main information of halo assembly history is contained within the main branch (e.g. Chen et al. 2020), which we use throughout this paper to model the properties of galaxies and their SMBHs.

To enhance the computational efficiency of our model adjustments, we use a subsampling technique on the TNGDark halos. This procedure tries to uniformly sample the distribution function $p[\mathcal{P}(z_{v,1/2})|M_v]$ by the following steps. First, we select all FoF halos at the desired redshift, denoted as z_d , with a halo mass satisfying $M_{v,\text{min}} \leq M_v < M_{v,\text{max}}$. We partition this range into n_{bin} logarithmically spaced bins of equal width. Next, for each halo residing in the i -th bin, we trace its main branch towards higher redshifts until the halo mass $M_v(z)$ drops below $M_v(z_d)/2$, thus determining its half-mass formation redshift, $z_{v,1/2}$. We then estimate the cumulative distribution function, denoted as $\mathcal{P}_i(z_{v,1/2})$, which characterizes the formation times of halos in this particular bin. By enforcing that the extracted halos in this bin have equidistant $\mathcal{P}_i(z_{v,1/2})$ values, we select a specific number, $\min(n_h, n_i)$, of halos, where n_i represents the total number of halos in this bin. Finally, we gather the extracted halos from all bins to give the subsample. This approach ensures that our sample accurately represents the overall population of halos at redshift z_d .

In this paper, we use two subsamples of halos from TNGDark at $z_d = 0$. These subsamples serve different purposes and are defined as follows:

- The ‘small sample’ $S_{h,\text{small}}$: This subsample consists of halos with a mass range of $(M_{v,\text{min}}, M_{v,\text{max}}) = (10^{10}, 10^{14.5}) h^{-1} M_{\odot}$. It is further divided into $(n_{\text{bin}}, n_h) = (9, 5)$ bins, resulting in a total of $n_{h,\text{total}} = 45$ halos. The primary goal of this small sample is to illustrate the assembly histories of individual halos.
- The ‘large sample’ $S_{h,\text{large}}$: This subsample consists of halos with a mass range of $(M_{v,\text{min}}, M_{v,\text{max}}) = (10^{10}, 10^{14.5}) h^{-1} M_{\odot}$. It is divided into $(n_{\text{bin}}, n_h) = (18, 50)$ bins, resulting in a total of $n_{h,\text{total}} = 720$ halos. The large sample is primarily used for statistical analysis. To account for the effect of subsampling in each bin, we assign a weight, $w_i = n_i / \min(n_h, n_i)$, to each halo in the i -th bin. This weight is used in computing summary statistics.

Figure A1 shows the distribution of halos in the two samples, in comparison with the overall population of halos in the simulation at $z = 0$. The small sample exhibits a sparse occupation of the halo mass - formation time space and misses halos in the extreme tail of the $\mathcal{P}_i(z_{v,1/2})$ distribution. In contrast, the large sample provides a finer and more complete coverage, following closely with the overall population. It is important to note that both samples are biased towards the higher end of the halo mass relative to the underlying distribution of all halos. This deliberate choice ensures the inclusion of

a sufficient number of massive halos, thereby covering their complex assembly histories.

Since observations at high redshift are limited to extremely bright and rare objects, it is difficult to obtain robust statistics from above samples when comparing with high- z observational results such as black hole mass functions (BHMFs). Meanwhile, to derive quantities that rely on small BHs, such as the cosmic BH mass densities (CBHMDs) at any given redshifts, the above sample is incomplete in the low-BH-mass end ($\lesssim 10^7 h^{-1} M_\odot$). To bypass these issues, we use analytical fittings to generate halo samples whose mass distribution and assembly histories are representative and complete of BH populations. Specifically, we use the HMF library (Murray 2014) to generate a halo mass function, $\Phi_c(M_v)$, for $M_{v,\min} \leq M_v < M_{v,\max}$ at the desired redshift z_d . We then sample a total of $n_{h,\text{total}}$ halos at z_d , with masses equally spaced between $M_{v,\min}$ and $M_{v,\max}$, and assign a weight w_c to each halo by

$$w_c \equiv \frac{\Phi_c(M_v)}{\Phi_{\text{samp}}(M_v)}, \quad (\text{A1})$$

where Φ_c is the halo mass function at z_d , and Φ_{samp} is the also mass function evaluated from our sample. We use the DIFFMAH library (Hearin et al. 2021) to randomly sample a mass assembly history at $z \geq z_d$ for each halo. Since our model in the fast phase requires halo V_{\max} as input, we assume an ideal NFW profile with a concentration parameter $c = c_f \approx 4$ for each halo throughout the fast phase history. We obtain the required halo properties, such as the maximal circular velocity, V_{\max} , the halo-centric distance, $r_{v\max}$, to achieve this velocity, and the total mass, $M_{v\max}$, enclosed in this radius, by (e.g. Bullock et al. 2001a; Klypin et al. 2001):

$$M_{v\max} = 0.468 \frac{M_v}{\mu(c)}; \quad (\text{A2})$$

$$r_{v\max} = \frac{2.163 r_v}{c}; \quad (\text{A3})$$

$$V_{\max} = V_v \sqrt{\frac{0.216c}{\mu(c)}}. \quad (\text{A4})$$

With the above semi-analytical procedure, we can define a sample at any desired redshift by specifying $(z_d, n_{h,\text{total}}, M_{v,\min}, M_{v,\max})$. This sample will be used to derive summary statistics beyond the scope of cosmological simulations, such as cosmic BH number density, mass density and growth rate density at z_d . Because BHs in satellite galaxies also contribute these quantities (see e.g. Zhang et al. 2022a), for each halo with mass M_v at z_d , we define another weight:

$$w_s \equiv 1 + \frac{\Phi_s(M_v)}{\Phi_c(M_v)}, \quad (\text{A5})$$

where Φ_s is the infall mass function of satellite subhalo, and Φ_c is the halo mass function, both evaluated at z_d from TNGDark and extrapolated to the mass below the resolution limit. The total weight, $w = w_c w_s$, is the final value used in computing summary statistics. Note that satellite galaxies do not follow exactly the same evolution as central galaxies, due to, for example, additional environment processes. Thus, our inclusion of satellites only provides a rough estimate of their contribution, which is small enough compared to large uncertainties in observations (see, e.g. Fig. 11).

APPENDIX B: RELATION OF TRANSITION REDSHIFT AND HALF-MASS FORMATION REDSHIFT

The transition redshift, z_f , is not commonly used in the existing literature for the construction of halo-based galaxy models. In order

to gain an overall feeling of the distribution of z_f , we present in Fig. B1 its correlation with the halo mass, M_v , at $z = 0$, as well as the half-mass formation redshift, $z_{v,1/2}$, which is more frequently used in halo-based models.

The three definitions of z_f yield qualitatively similar results: z_f consistently decreases with increasing M_v and rises monotonically with $z_{v,1/2}$. The definition of z_f based on $\Gamma = 3/2$ consistently falls between the other two definitions. Consequently, we use the two model variants, High- z_f and Low- z_f , to bracket the systematic uncertainty in the definition of z_f . The relationship between z_f and $z_{v,1/2}$ conditioned on $M_{v,z=0}$, and vice versa, is shown by the colors of the scattered points in the two panels of the figure for the High- z_f case. At a fixed conditioning variable, the conditional trend is weaker than the global trend, but remains statistically significant. This suggests that z_f provides supplementary information to halo assembly that is not entirely captured by $z_{v,1/2}$. Given that the ‘1/2’ in the definition of $z_{v,1/2}$ is arbitrary, we opt to use z_f in this paper to separate the different phases of halo assembly.

APPENDIX C: FLUCTUATIONS OF HALO ASSEMBLY HISTORY

To characterize the fluctuation in halo assembly history and the difference between the two phases, we compute the logarithmic residual of the simulated virial velocity V_v relative to $V_v^{(\text{fit})}$, obtained from a parametric fitting of the halo mass assembly history (see §2, Eqs. 12 and 13), as

$$\Delta \log V_v = \log V_v - \log V_v^{(\text{fit})}. \quad (\text{C1})$$

We then use the standard deviation of $\Delta \log V_v$ obtained from all halo assembly histories at a specific epoch relative to the transition time, $t - t(z_f)$, to quantify the fluctuation in halo assembly. The results are shown in Fig. C1 for the two variants, $\gamma_f = 3/8$ and 0, and for three bins of halo mass at $z = 0$. For given γ_f , halos of different masses have a similar pattern: significant fluctuation prior to the transition, a rapid decline during the transition, and subsequent stabilization. The fluctuation during the slow phase is about 1/4 to 1/3 of that in the fast phase, with the transition period lasting about $1 h^{-1} \text{Gyr}$. The similarity for halos with different masses suggests a unified path of deepening in the gravitational potential well in terms of a time variable that is measured relative to the transition time. This universality motivates us to use a single parametric form (Eq. 12) to model mass assembly histories of all halos, and to separate the two phases by a constant threshold of γ_f (Eqs. 10 and 11).

The rapid change in the gravitational potential well can also drive changes in the binding energy of dark matter particles within the halo (see e.g. figure 10 of Zhao et al. 2003). In Fig. C2, we present E_b , the specific (per unit mass) binding energy of particles, and γ , the specific growth rate of the halo, as functions of redshift for a Milky Way-mass halo ($M_{v,z=0} \approx 10^{12} h^{-1} M_\odot$). This particular halo does not experience a ‘back-splash’ event in its history, and thus environmental effects do not significantly contribute to the change in the particle binding energy. The binding energy is computed using all particles bound to the central subhalo. The thick curve in the top panel represents the average E_b traced by all particles bound to the central subhalo over the redshift range shown in the figure. The zero point of E_b is set such that the maximum value among all the tracers is zero. A distinct trend in E_b emerges: prior to the transition ($z \gtrsim 2$), the particles are nearly bound; within the transition period ($0.8 \lesssim z \lesssim 2$, defined by $0 < \gamma^{(\text{fit})} < 3/8$), the binding energy decreases rapidly and fluctuates significantly; well after the transition ($z \lesssim 0.8$), the

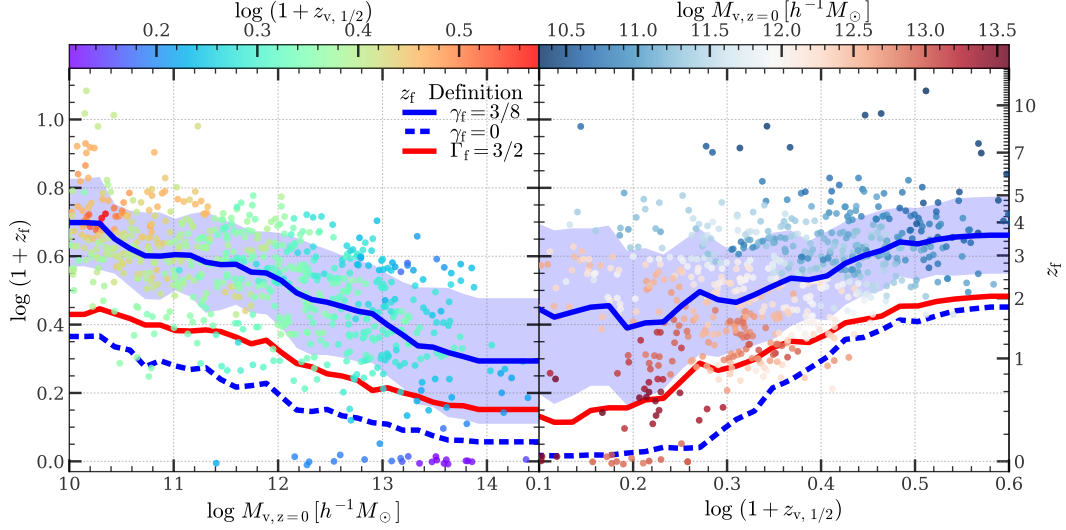


Figure B1. The mean transition redshift (z_f) as a function of halo mass ($M_v \equiv M_{200c}$) at $z = 0$ (left panel) and half-mass formation redshift ($z_{v,1/2}$, right panel). In each panel, three definitions of z_f are shown by three curves, respectively, as indicated by the legends. For the $\gamma_f = 3/8$ (High- z_f) case, scatter points represent individual halos, while the blue shading indicates the standard deviations. Colors of points are encoded according to the colorbar. Halo sample $S_{h,\text{large}}$ is used to produce this figure. See §2 for the details of halo transition time.

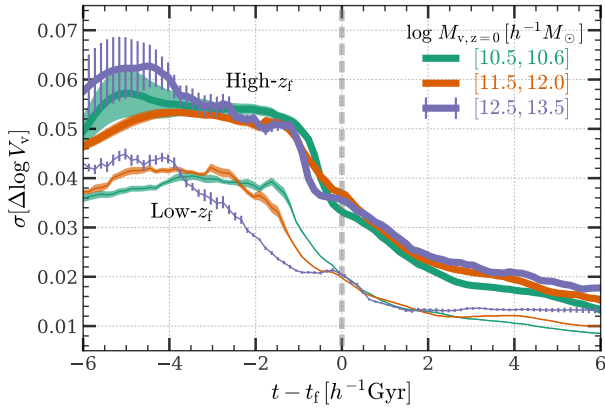


Figure C1. Fluctuation of halo assembly history, defined as the standard deviation of $\Delta \log V_v = \log V_v - \log V_v^{(\text{fit})}$ at given $t - t_f$, where $V_v^{(\text{fit})}$ is obtained by a parametric fitting described in §2, and $t_f \equiv t(z_f)$ is the cosmic time at the transition redshift z_f . Results for halos with different mass are shown by different colors. Thick and thin curves are for the $\gamma_f = 3/8$ (High- z_f) and $\gamma_f = 0$ (Low- z_f) variants, respectively. Error bars or shadings represent the standard deviations obtained by 20 bootstrap resamplings. This figure shows that the gravitational potential of halo drops significantly near the transition, and appears stabilized after that.

particles are all tightly bound and their binding energy stabilizes at a roughly constant value. A similar pattern is seen even when considering only particles within $0.2R_v$, approximately the upper limit of the size of the SGC (§3.3). The similarity in the trajectories of E_b and γ suggests that particles closely respond to changes in the halo potential, supporting our model assumption on the relation between the two-phase assembly of halos and the dynamical hotness of galaxies that form in them.

The lower panel of Fig. C2 presents three versions of γ obtained using: the simulated assembly history; a parametric function fitting of $M_v(z)$ (denoted as ‘fit’); and a smoothed version of $M_v(z)$ in a Gaussian kernel with a width of $\tau_{\text{dyn}}(z)$ (denoted as ‘sm’). A notable

feature is the presence of fluctuations in γ even in the smoothed version. During the fast phase, as defined by the Low- z_f variant where $\gamma^{(\text{fit})} \geq \gamma_f = 0$, $\gamma^{(\text{sm})}$ makes an excursion below γ_f at $z \approx 1.7$ and returns at $z \approx 1$ (see also the examples in Fig. 1). This suggests transformations of galaxies from bulge-like to disk-like and back to bulge-like, corresponding to dynamic oscillations between Q1 and Q2 described in §3.3.

To quantify such dynamic oscillations, we identify all events of excursion to the slow assembly regime during the fast phase of each halo. Here, we define an excursion event as a continuous time interval during which $\gamma^{(\text{sm})}$ falls below γ_f . Fig. C3 shows various statistics of these excursions for the halo sample $S_{h,\text{large}}$ using both High- z_f and Low- z_f . For both variants, the number of excursions ($N_{\text{excursion}}$) is ≤ 2 for about 80% of the halos, and ≤ 3 for nearly all halos, indicating that excursions are not rare. The total duration of all excursions ($\tau_{\text{excursion}}$) accounts for $\leq 30\%$ of the fast phase for about 80% of halos, and $\leq 40\%$ for nearly all halos, suggesting that these periods of temporary excursions away from dynamically hotness are relatively short.

The starting time of these excursions, $t_{\text{excursion}}$, is within $3 h^{-1}$ Gyr prior to the transition time defined by the High- z_f variant for about 80% of halos, as one can see from the lower left panel of Fig. C3). In contrast, the distribution of $t_f - t_{\text{excursion}}$ is quite uniform between 0 and $8 h^{-1}$ Gyr when Low- z_f is adopted. This difference implies that excursions are frequent when $0 < \gamma^{(\text{fit})} < 3/8$, suggesting that morphological transformations of galaxies are frequent during such periods. As discussed in §3.3, the transition to Q2 is often associated with ‘wet compactification’ that may lead to the emergence of ‘blue nuggets’ and enhanced growth of SMBHs. If the AGN feedback is sufficiently strong, it may lead to the formation of ‘red nuggets’ even at high redshift. The distribution of $M_{v,\text{excursion}}$, the halo mass during the excursion, is shown in the lower middle panel. The result indicates that excursions are most frequent when M_v is about 10 to 20 percent of M_f , the halo mass at the end of the fast phase. As shown by the top right panel, the typical mass increase during all the excursions, $\Delta M_{v,\text{excursion,all}}$, is about 6 to 12 percent of M_f . The relatively low values of $M_{v,\text{excursion}}/M_f$ and $\Delta M_{v,\text{excursion,all}}/M_f$ indicate that, for most systems, the mass of the disk-like component expected to form during

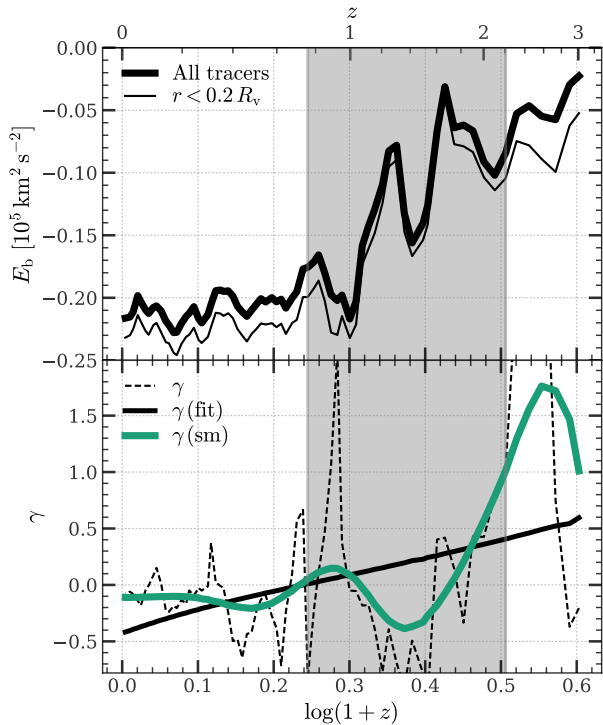


Figure C2. Upper panel shows the average specific binding energy of dark matter particles as a function of redshift in the main branch of an example halo with $M_{v,z=0} \approx 10^{12} h^{-1} M_{\odot}$. **Thick** curve is obtained by using all particles bound to the central subhalo in the range of redshift shown here, while **thin** curve is obtained by only using those within $0.2R_v$. Lower panel shows the specific growth rate γ (defined by Eq. 9) of the same halo. **Dashed, solid black and green** curves show the results obtained from the simulated assembly history, the fitting by a parametric function, and the smoothing by a kernel of size τ_{dyn} (see Fig. 1 and §2 for the details). **Grey** shaded area indicates the transition redshift bracketed by the two variants, Low- z_f and High- z_f . This figure suggests that the binding energies of particles respond well to γ , and provides support to our two-phase separation of galaxy formation by a transition of halo assembly.

the excursions is likely much lower than that of the mass component formed during the entire fast assembly phase. However, as shown in the lower right panel, for a significant fraction of halos, the mass acquisition during an excursion, $\Delta M_{v,\text{excursion}}$, can actually be comparable to the halo mass at the beginning of the excursion, $M_{v,\text{excursion}}$, particularly when the High- z_f variant is used. This indicates that the mass acquisition during some excursions at high z are significant. Such an excursion is expected to generate a system in Q2, producing a disk-like structure that is unstable and clumpy.

To summarize, the existence of excursions to the slow assembly regime during the fast assembly phase is not expected to have a significant impact on our results based on characterizing halo assembly histories with the two phases proposed in the main text. The discussion above also highlights the connections between the fluctuation in halo assembly and the transformation of galaxy morphology. This has significant implications for galaxy formation, particularly at high z where such fluctuations are expected to be important. Clearly, detailed investigations are needed to quantify such connections and to explore their implications.

APPENDIX D: ADJUSTMENT OF MODEL PARAMETERS

Most of our model parameters have theoretically plausible values. However, there remain parameters that are still uncertain. We thus seek observations for calibration. In this section, we elaborate our heuristic approach to adjust model parameters.

The overall strategy, as stated in §4.5, involves only using the local stellar mass (M_*) to halo mass ($M_v \equiv M_{200c}$) relation at $z \approx 0.1$ obtained by [Yang et al. \(2012\)](#) and the local black hole mass (M_{bh}) to bulge stellar mass ($M_{*,\text{bulge}}$) relation for elliptical galaxies at $z \approx 0$ obtained by [Graham & Sahu \(2023\)](#), to calibrate model parameters. We deliberately avoid using high-redshift observations for fine-tuning the parameters, since we aim to maximize the predictive power of our model. It is also noteworthy that all model parameters in our phase-phase model remain constant over the cosmic time, and thus, any redshift dependencies of the predicted galaxies and SMBHs come from halo assembly histories. This design strategy remains valid as long as our model effectively reflects the fundamental physics driving galaxy formation in the self-gravitating turbulent medium, which we confirm through all the model-observation comparisons presented in this paper.

As described in §5.2 and shown in Fig. 7, it is evident that a large value of the mass-capturing parameter (α_{cap}) is critical for the SMBH to evolve into the self-regulating regime that matches the observed $M_{\text{bh}} - M_{*,\text{bulge}}$ relation. However, an excessively large value of α_{cap} results in an upward shift of the $M_{\text{bh}} - M_{*,\text{bulge}}$ relation beyond the observed range. Consequently, we set $\alpha_{\text{cap}} = 2.5$ to ensure that the predicted relation eventually converges with that obtained by [Graham & Sahu \(2023\)](#). As the observed $M_{\text{bh}} - M_{*,\text{bulge}}$ relation for ellipticals is limited to massive SMBHs ($M_{\text{bh}} \gtrsim 10^7 h^{-1} M_{\odot}$), the value of the enhancement factor, α_{en} , which governs early-time SMBH growth, must be calibrated by additional observation. We thus use the observed $M_* - M_v$ relation for it.

Figure D1 shows the predicted relation between stellar mass (bulge or total) and halo mass according to our model, with α_{en} set to 1 to deactivate the enhancement (pink curve, labeled as ‘BHEnhanceOff’). All other parameters are at their default values (see Table 1). Without the fast growth resulting from SN-driven turbulence in SGC, SMBHs are unable to grow effectively, leading to an excessively fast early growth of stellar bulge and an abundance of over-massive galaxies in high-mass halos. Conversely, if α_{en} is too large, it would result in an expectation of excessively low predicted stellar masses in high-mass halos. Therefore, we set $\alpha_{\text{en}} = 3$ to match the observation. As a self-consistency check, we also show the stellar mass to halo mass relation when we completely disable SMBH growth ($\alpha_{\text{acc}} = 0$, shown by the purple curve labeled as ‘BHAccOff’). As expected, the high-mass end of the relation is significantly lifted, indicating the necessity of AGN feedback from accreted SMBHs to reproduce the observed stellar masses in high-mass halos.

Unlike the BH capturing parameters, the seed mass of SMBH does not impact the stellar masses of high-mass galaxies. This is evident in Fig. 7, where SMBHs with arbitrary seeded mass quickly converge to the observational line. Therefore, it is expected that the seed mass solely affects the stellar mass of low-mass systems, as demonstrated by the brown curve labeled as ‘BHOverseeded’ in Fig. D1 through the overseeding of the SMBHs. As the seed mass distribution has not been comprehensively understood, we opt to use small stellar-level seeds with $M_{\text{bh},\text{min}} = 10 h^{-1} M_{\odot}$, relying on early-time fast growth to boost it to a SMBH. This choice is thought to be both physically plausible and numerically stable, hence it is adopted as our default model.

For the parameter β_{sn} governing the strength of SN feedback in

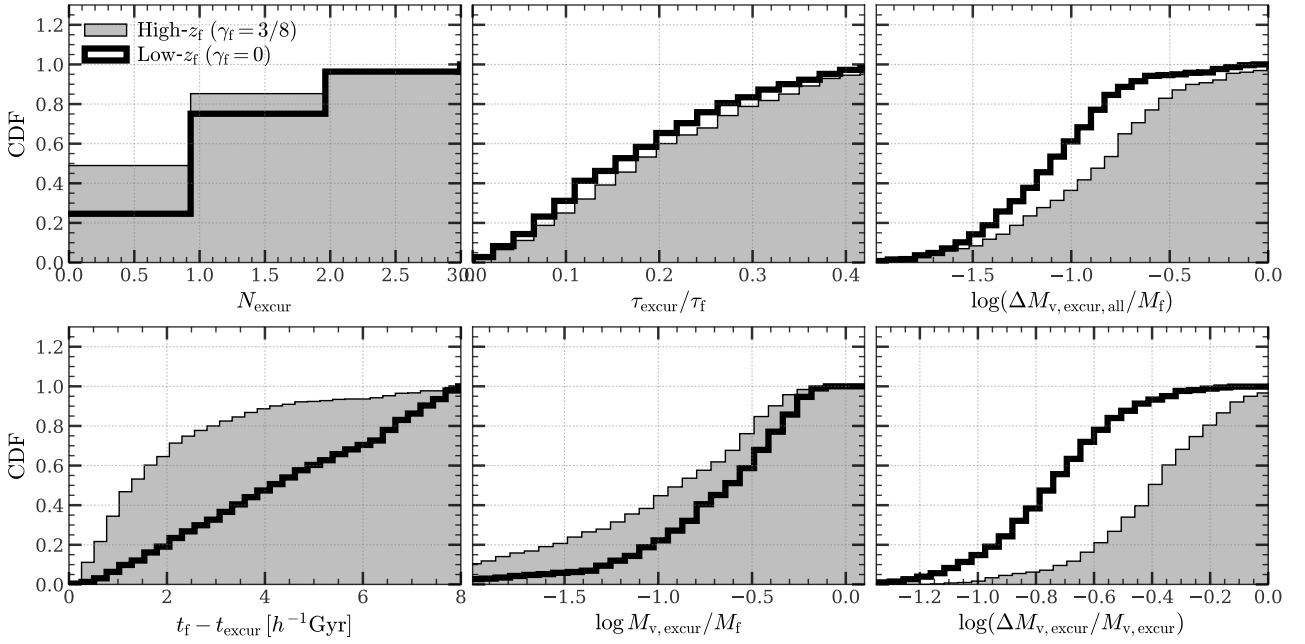


Figure C3. The cumulative distribution of quantities describing the excursion of halo assembly to the slow regime ($\gamma^{(\text{sm})} < \gamma_f$) during the fast phase ($z \geq z_f$). The **first row** shows the statistics for main branches, while the **second row** shows the statistics for excursions. N_{excur} is the number of excursion events of a halo during its fast phase. $\tau_{\text{excur}}/\tau_f$ is the total time spent by a halo in all the excursions divided by the duration of the entire fast phase. $\Delta M_{v,\text{excur,all}}/M_f$ is the total mass accreted during all excursions during the fast phase divided by the mass at the end of the fast phase. $t_f - t_{\text{excur}}$ is the difference of cosmic time between the end of the fast phase and an excursion. $M_{v,\text{excur}}/M_f$ is the halo mass at an excursion divided by that at the end of the fast phase. $\Delta M_{v,\text{excur}}/M_{v,\text{excur}}$ is the mass accreted during one excursion divided by the mass prior to the excursion. Two variants are shown by **thin** and **thick** curves, respectively. This figure gives a summary of excursions in halo assembly, which potentially drives the galaxy temporarily to a disk-like morphology.

low-mass halos, we expect a value of approximately 2, ensuring that the V_{g}^2 and V_{w}^2 terms in equation (68) have the dimensionality of specific energy. Indeed, this value yields a faint-end behavior of the $M_* - M_v$ relation that well matches Model-III of Lu et al. (2014), which concludes that an upturn of the faint end is necessary to match the observed galaxy stellar mass function in clusters. For comparison, we present in Fig. D1 a model with $\beta_{\text{sn}} = 4$ (green curve, labeled as ‘SNStrong’), which obviously eliminates the faint-end upturn and even results in an underestimation of M_* for halos $M \leq 10^{11} h^{-1} M_{\odot}$.

It is important to note that full Bayesian inference based on complete sampling of model ensembles and model parameters gives a more reliable parameter calibration and model comparison. However, it needs a careful combination of observational data to mitigate their systematics and a precise design of the likelihood function to account for the error distribution and covariance of data points. This is beyond the scope of this paper and will be addressed in future work.

This paper has been typeset from a $\text{\TeX}/\text{\LaTeX}$ file prepared by the author.

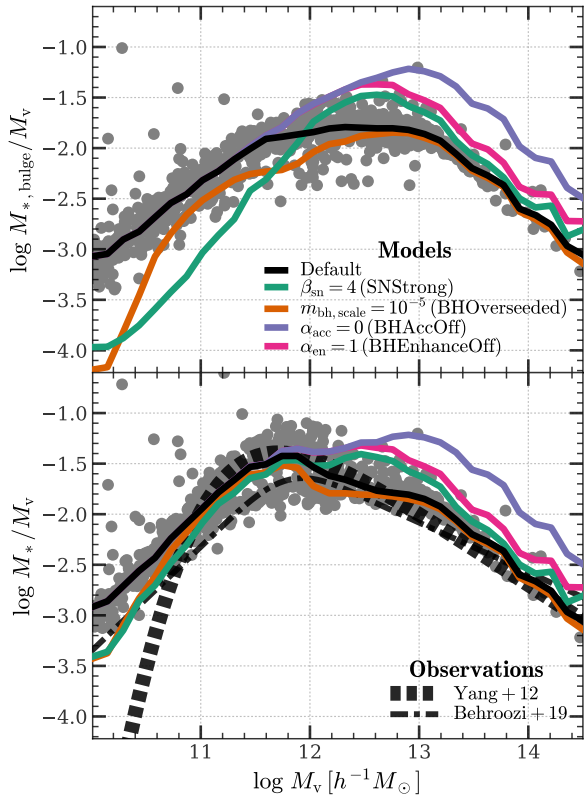


Figure D1. Stellar mass to halo mass ($M_v \equiv M_{200c}$) ratio as a function of halo mass at $z = 0$ predicted by our models, where z_f is defined by the Low- z_f variant. **Upper panel** shows bulge stellar mass and **bottom panel** shows total stellar mass (bulge + disk). Gray scatter points represent individual galaxies obtained from default model parameters (see Table 1), while the **black solid curve** shows the median relation. **Colored curves** are obtained by varying one parameter, as indicated in the legend, from the default model. In the bottom panel, **thin black dashed curve** shows the relation obtained by [Yang et al. \(2012\)](#) using conditional stellar mass function modeling, while **thick black dashed curve** shows the relation obtained by [Behroozi et al. \(2019\)](#) using an empirical model calibrated to various observations, with halo mass defined to be the peak mass.